SPUTTER-ION PUMPS: PERFORMANCE ASSESSMENT AND NOBLE-GAS PUMPING OPTIMISATION IN VIEW OF THE COMBINATION WITH NON-EVAPORABLE GETTERS

Settore Scientifico disciplinare FIS/01

Tesi di Dottorato di:
Tommaso Porcelli

Coordinatore: Prof. Marco Bersanelli

Supervisore: Prof. Carlo Pagani

Co-supervisori: Dott. Paolo Michelato

Dott. Fabrizio Siviero

"Πρὸ δὲ τῶν λέγεσθαι μελλόντων πρῶτον περὶ κενοῦ διαληπτέον. …καὶ ὅτι κενὸν μὲν ἄθρουν οὐκ ἔστι κατὰ φύσιν βίας τινὸς μὴ παρεισελθούσης, καὶ πάλιν ὅτι οὐκ ἔστι ποτὲ τὸ παράπαν κενόν, παρὰ φύσιν δὲ γενόμενον."

(Ἥρωνος Ἀλεξανδρέως Πνευματικῶν Πρῶτον)[1]

---

[1] "But, before proceeding to our proper subject, we must treat of the vacuum. …and that there is no continuous vacuum except by the application of some force: and again, that the absolute vacuum is never found, but it is produced artificially." (Hero of Alexandria, "The pneumatics", 1st century AD; translation by B. Woodcroft, London, 1851).

Table of contents

3

Preface

The present study deals with the pumping properties of sputter-ion pumps, focusing in particular on their combination with non-evaporable getters and on the sorption of noble gases and hydrocarbons, which cannot be pumped by these latter. The project was set up in the framework of the *Physics, Astrophysics and Applied Physics Ph.D. School* at *Università degli Studi di Milano* and the work has been entirely carried out in the *Vacuum Systems Development Laboratory* at *SAES Getters S.p.A.* in Lainate, Italy, during the past three years.

This thesis resumes the main results collected about the development and characterisation of new sputter-ion pumps implementing innovative cathodes and enhancing the pumping performance for gases which are not pumped by getters.

After a brief introduction in Chapter 1 about the goals of this project, Chapter 2 describes the state of the art in the field of sputter-ion pumps, explaining their functioning and illustrating the improvements implemented during the past decades. Chapter 3 introduces the idea of combining a non-evaporable getter cartridge with a sputter-ion pump and presents the main advantages and synergies given by this type of combination pump in several ultra-high-vacuum applications, showing some examples and real case studies. The cathodes characterised during this Ph.D. are listed in Chapter 4, together with the materials and the techniques employed for their production. The experimental test-bench is described in Chapter 5, which shows also the steps made towards the fine tuning and optimisation of an original and specific testing sequence for sputter-ion pumps in view of the combination with getters. Chapter 6 and Chapter 7 present and discuss, respectively, the results of these sorption tests and the FESEM/EDX and XRD analyses made on each cathode after its use. Finally, Chapter 8 draws conclusions and outlines the current status and the future prospects of this project.

1. Introduction

Since their introduction in the 1950s, sputter-ion pumps (SIPs) have been employed as an efficient and reliable way to maintain high vacuum (HV) or ultra-high vacuum (UHV) conditions (*i.e.*, pressures lower than 10^{-5} mbar and 10^{-9} mbar, respectively) in a wide range of technological applications. In its simplest configuration, which is commonly referred to as diode pump, a SIP consists of a vacuum envelope enclosing an array of stainless-steel cylindrical anodes placed between two Ti cathode plates. Its working principle relies on the simultaneous application of an electric and a magnetic field, whose combined action results in the ionisation of the residual gas inside the pump. Gas ions with a high kinetic energy can be subsequently pumped in both cathodes and anodes by means of several different chemisorption or physisorption mechanisms. A much more detailed description of a SIP's functioning is given in Chapter 2, together with an exhaustive list of cited works, which refer to both scientific papers and vacuum technology handbooks.

SIPs are able to efficiently pump most of the gas species and they are particularly effective in the sorption of chemically-reactive gases (*e.g.*, N_2, CO, CO_2). However, their use may imply also a number of drawbacks determined by their working mechanisms. First of all, pumping speed of a SIP is not constant but varies over its range of working pressures. It usually increases from lower pressure until about 10^{-6} mbar and then it starts to decrease as pressure keeps growing. At the same time, a consistent pumping speed reduction is typical also at low pressure and in particular with H_2, which is the main residual gas in UHV systems. Another critical aspect of a conventional diode SIP is represented by the sorption of noble gases with a special focus on Ar—which is the most common among them in air—whose pumping speed is generally only 2–5% of the nominal N_2 pumping

speed. Moreover, the sorption of relatively small quantities of Ar by a diode SIP may lead to the onset of the so-called *argon instability,* an undesired phenomenon consisting in periodical pressure bursts caused by the sudden release of previously-pumped Ar from the cathodes [1]. As better explained in Chapter 2, this was bypassed thanks to the development of noble-diode SIPs, in which the use of one Ti and one Ta cathode removes the argon-instability problem and ensures a higher Ar pumping speed; nevertheless, this improvement is possible only to the detriment of the sorption rates of chemically-reactive gases, which are reduced by 15–20%. Apart from argon instability, during its functioning a SIP is in general prone to the undesired regurgitation of previously-sorbed gases from its inner surfaces [2].

The need to ensure high pumping speeds even in the UHV range leads therefore to the use of very large SIPs with a huge number of electrodes and very heavy magnets. Nowadays, however, several applications pose strict constraints in terms of design, size, and weight of the pumping elements, thus limiting the feasibility of vacuum systems based on SIPs alone, especially if high pumping speeds are necessary. As a matter of fact, the current trends in the particle accelerators and light sources community seeks the design of increasingly compact machines, driven by both technical and logistic reasons (*e.g.*, the need for very high energies and magnetic fields and the cost of the magnets necessary to produce them, which increases with their size). The *Compact Linear Collider* (CLIC), which is currently under study at CERN in Geneva, Switzerland, and the MAX IV project at MAX IV Laboratory in Lund, Sweden, prove that this is the road taken for the coming years [3] [4]. At the same time, also the manufacturers of portable analysers and analysis instrumentation aspire to a continuous miniaturisation of these devices and of their vacuum systems.

New pumps made by SIPs combined with non-evaporable getter (NEG) pumps were thus investigated in order to overcome these constraints. NEGs are a class of materials employed in a number of technological applications requiring the maintaining of stable HV or UHV conditions. They usually consist in alloys or powder mixtures of elements belonging to the 4th (Ti, Zr, Hf) and to the 5th (V, Nb, Ta) group of the periodic table, plus in some cases Al, Fe or other elements. Once activated at high temperature, they do not require power to operate and they provide an effective pumping for chemically-reactive gases—both in terms of pumping speed and sorption capacity—through the formation of stable chemical bonds between their active surface and the gas molecules, even at room

temperature. Noble gases, which do not form chemical bonds with other elements, cannot be pumped by NEG; pumping speeds provided for hydrocarbons are also negligible. Since their discovery in the 1950s, several NEG formulations have been developed through the years (*e.g.*, St707, St101, and St172) and getter pumps made of cartridges of NEG disks, pills, or strips are nowadays widely used. More detailed information about NEG materials and their functioning can be found elsewhere [5] [6] [7] [8]. Moreover, NEG coatings made by magnetron sputtering were introduced in the late 1990s and since then they have been extensively employed in several facilities, such as the *Large Hadron Collider* (LHC) at CERN [9] [10] [11] [12].

Studies made at CERN in the past on vacuum chambers of the *Large Electron-Positron Collider* (LEP) evidenced the possibility to attain pressures as low as 10^{-13} mbar by using NEG strips together with small SIPs [13]. Other tests made at the *Pohang Accelerator Laboratory* confirmed the advantages given by the use of combined NEG+SIP pumps, showing that thanks to them it is possible to obtain lower pressures and to speed up the system pump down and bake-out [14].

Following these results, novel combination pumps based on the synergic coupling of a small SIP and a non-evaporable getter (NEG) cartridge have been recently developed by *SAES Getters* and merchandised under the tradename *NEXTorr*® [15]. This innovative configuration allows the NEG to be the primary pumping system, while the SIP is tasked only with removing the so-called non-getterable gases (*i.e.*, noble gases and hydrocarbons). NEG+SIP combination pumps provide an efficient pumping—particularly for H_2—and are very favourable in terms of weight, dimensions and performance. NEXTorr® pumps are very light and compact: a NEXTorr® D2000-10, for instance, which provides 2000 l/s for H_2, weighs 6.8 kg and has a total volume of 1.8 l. As a comparison, a VacIon® Plus 500 diode SIPs providing 500 l/s for N_2 (about 700 l/s only for H_2), weighs 120 kg and has a total volume of about 72 l. Moreover, the synergic integration of these two technologies ensures better performances compared to the simple coupling of a NEG cartridge and a SIP.

Nevertheless, further improvements in the SIP+NEG technology are still possible. The pumping of noble gases—which is one of the main SIP tasks in a combination pump— is particularly critical, due to the above-mentioned limitations of diode and noble-diode SIPs. In systems operating under typical UHV conditions, the gas load due to the non-getterable gases comprises a small percentage of the total pressure and therefore it does not affect the pumping

performance of a SIP throughout its working lifetime. However, some applications might require to deal with larger loads of non-getterable gases (*e.g.*, portable mass spectrometers, helium ion microscopes, inductively coupled plasma mass spectroscopes). The regurgitation of previously-pumped gases (both getterable and non-getterable) during the functioning of a SIP is also challenging, especially in view of the synergic combination with NEG; this is mostly true in the case of CH_4, which is not pumped by NEG but whose ionisation by a SIP produces H_2, which is instead a getterable gas. From this point of view, the gas quantities released by the SIP that the NEG pump can shoulder prior to reach its maximum capacity become an important aspect that should not be neglected during the characterisation of a combination pump, although in most cases these quantities are well below the saturation limits of NEG cartridges.

It is worth mentioning that most part of the literature referring to SIPs is quite outdated: Penning cell, which is at the basis of SIP technology, was described in the 1930s [16] and SIPs themselves date back to the 1950s [17] [18]. Most of the improvements in this technology were made during the following two decades, including the introduction of noble-diode pumps [19]. Since then, except for the major breakthrough given by the development of triode pumps in the 1980s [20], few papers have been published about SIPs and their possible enhancement. Nowadays, the possibility of combining NEG and SIP devices, together with the present, increased knowledge in the field of powders metallurgy, gives the chance to make further steps towards the optimisation of noble gas and CH_4 sorption. For instance, an enhanced sorption of Ar—even to the detriment of the pumping speed of chemically-reactive gases—might be now acceptable, thanks to the presence of the NEG cartridge, which is able to efficiently deal with large quantities of these latter. For the same reason, a SIP able to develop a high H_2 partial pressure through ionisation and regurgitation might be even preferable to others when pumping CH_4 in the presence of NEG: as a matter of fact, the NEG would provide a very high pumping speed for H_2, so that the overall pumping speed of the SIP+NEG combination—measured while pumping CH_4—would be greatly enhanced compared to the case of the SIP only.

This project aimed therefore at a better awareness and understanding of both beneficial and critical aspects of SIPs, in order to enhance their performance and hence to strengthen the SIP+NEG coupling. The organisation of this three-year long Ph.D. research followed two main directions:

−   an in-depth analysis of the pumping properties of conventional diode and noble-diode SIPs, with a special focus on noble gases, CH$_4$ and on the fine tuning of a dedicated SIP testing procedure in view of the coupling with NEG;

−   the study of innovative SIPs from the point of view of the cathode materials, focused on the sorption of noble gases and CH$_4$ and to be characterised according to the same optimised procedure of the previous point.

The performed sorption tests were flanked by a series of physicochemical analyses (FESEM/EDX, XRD) of the cathodes under study, in order to highlight any possible correlation between their pumping performances and the surface modifications induced by SIP functioning.

Finally, part of the work made in the framework of this project during these three years has been already presented in the form of a conference poster and four scientific papers; their contents are resumed and more in-depth discussed in the next chapters.

References

[1]   J. A. Vaumoron and M. P. De Biasio, "Argon and rare gas instability with heavy metal cathode Penning Pumps," *Vacuum,* vol. 20, no. 3, pp. 109-111, 1970.

[2]   M. Audi, "Pumping speed of sputter ion pumps," *Vacuum,* vol. 38, no. 8-10, pp. 669-671, 1988.

[3]   C. Garion, "Simulations and vacuum tests of a CLIC accelerating structure," in *Proc. of IPAC2011*, San Sebastian, Spain, 2011.

[4]   E. Al-Dmour, D. Einfeld, J. Pasquaud, M. Quispe, J. Ahlbäck, P. Fernandes Tavares and M. Grabski, "Vacuum system design for the MAX IV 3 GeV ring," in *Proc. of IPAC2011*, San Sebastian, Spain, 2011.

[5]   J. Lafferty, Foundations of Vacuum Science and Technology, Wiley, 1998.

[6]   P. della Porta, T. Giorgi, S. Origlio and F. Ricca, in *Proc. 8th Nat. Symp. AVS*, london, 1962.

[7]   C. Boffito, B. Ferrario, P. della Porta and L. Rosai, "A nonevaporable low

temperature activable getter material," *J. Vac. Sci. Technol.,* vol. 18, p. 1117, 1981.

[8] C. Benvenuti and P. Chiggiato, "Pumping characteristics of the St707 nonevaporable getter (Zr 70-V 24.6-Fe 5.4 wt%)," *J. Vac. Sci. Technol. A,* vol. 14, p. 3278, 1996.

[9] C. Benvenuti, J. Cazeneuve, P. Chiggiato, F. Cicoira, A. Escudeiro Santana, V. Johanek, V. Ruzinov and J. Fraxedas, "A novel route to extreme vacua: the non-evaporable getter thin film coatings," *Vacuum,* vol. 53, no. 1-2, pp. 219-225, 1999.

[10] C. Benvenuti, P. Chiggiato, F. Cicoira and Y. L'Aminot, "Nonevaporable getter films for ultrahigh vacuum applications," *J. Vac. Sci. Technol. A,* vol. 16, no. 1, pp. 148-154, 1998.

[11] A. Prodromides, Non-Evaporable Getter Thin Film Coatings for Vacuum Applications, Ecole Polytechnique Fédéral de Lausanne, 2002.

[12] P. Chiggiato and P. Costa Pinto, "Ti-Zr-V non-evaporable getter films: From development to large scale production for the Large Hadron Collider," *Thin Solid Films,* vol. 515, pp. 382-388, 2006.

[13] C. Benvenuti, J. Bojon, P. Chiggiato and G. Losch, "Ultimate pressures of the large electron positron collider (LEP) vacuum system," *Vacuum,* vol. 44, no. 5-7, pp. 507-509, 1993.

[14] C. Park, S. Chung and P. Manini, "Combination of compact nonevaporable getter and small ion pumps for ultrahigh vacuum systems," *J. Vac. Sci. Technol. A,* vol. 29, no. 1, 2011.

[15] P. Manini, A. Conte, L. Viale, A. Bonucci and L. Caruso, "A novel route to compact, high performance pumping in UHV-XHV vacuum systems," *Vacuum,* vol. 94, pp. 26-29, 2013.

[16] F. Penning, "Ein neues Manometer für niedrige Gasdrucke, insbesondere zwischen 10−3 und 10−5 mm," *Physica,* vol. 4, no. 2, pp. 71-75, 1937.

[17] A. Gurewitsch and W. Westendrop, "Ionic pump," *Rev. Sci. Instrum.,* vol. 25, no. 3, p. 389, 1954.

[18] L. Hall, "Electronic Ultra-High Vacuum Pump," *Rev. Sci. Instrum. ,* vol. 29, no. 5, pp. 367-370, 1958.

[19] R. Jepsen, "The physics of sputter-ion pumps," in *Proc. 4th Int. Vacuum Congr.*, London, 1968.

[20] M. Pierini and L. Dolcino, "A new sputter ion-pump element," *J. Vac. Sci. Technol. A,* vol. 1, p. 1983, 140.

2. Principles of sputter-ion pumping

Sputter-ion pumps (SIPs) were first described during the 1950s [1] [2] and marketed under the trade-name VacIon® [3]. Since then, several other studies have been published about SIP technology and its further developments; most of them, however, date back to the 1960s and 1970s, including the major step forward represented by the introduction of noble-diode SIPs [4].

This chapter gives some essential information about the functioning principle of SIPs and their sorption mechanisms for typical residual gases in HV and UHV system. These basic concepts are needed to fully understand the tests made during this research and the achieved experimental results. A complete review of SIP technology was made by Welch and can be found elsewhere [5]; for an exhaustive study of the physics of SIPs and or their main technical issues, please refer to the bibliographical sources listed in the following.

2.1. Functioning principle of SIPs: the Penning cell

In its simplest configuration—described by Hall and known as diode pump—a SIP consists in a vacuum envelope enclosing an array of stainless-steel anodes placed between two titanium cathode plates [2]. The simultaneous application of a high voltage between the electrodes and of an external magnetic field coaxial to the anodes (usually in the range of 3–7 kV and 0.1–0.2 T, respectively) allows the ignition of plasma inside the pump. As a matter of fact, the applied voltage causes the emission of electrons from the cathodes and accelerates them towards the anodes; along their way, these electrons may collide with residual

gas molecules, thus producing high-energy positive ions, which are in turn accelerated towards the cathodes. Thanks to the applied magnetic field, the electrons travel along very long helicoidal trajectories and tend to be trapped between the electrodes, thus enhancing their chance to strike a gas molecule and ionise it. Upon collision with the cathodes, ions can be subsequently pumped in several ways according to their nature, as explained in Section 2.2.

This scheme is analogous to that of cold-cathode gauges and relies on the pumping action of a low-pressure electrical discharge, also known as a Penning discharge. The gettering effect of vacuum devices in which an electrical discharge is applied between a couple of electrodes has been known for a long time: since the 19th century, a net decrease of pressure associated with the formation of a sputtered metallic deposit coming from the cathode and deposited on the glass envelope has been repeatedly described and documented, among the others, by Plücker and Vegard [6] [7]. In 1934, Gaede observed the above-mentioned electronic confinement caused by the simultaneous application of a magnetic field [8]. Few years later, Penning first recognised the possibility to reduce pressure inside a closed chamber through a magnetically-confined electrical discharge [9].

At pressure lower than 10^{-3} Torr and over a wide range of pressures, the ion current I^+ of a Penning cell was found to be linear with pressure; as a matter of fact, this represents the functioning principle of cold-cathode gauges. The I^+/P characteristics of a SIP's Penning cell—*i.e.*, its sensitivity—is thus a fundamental parameter, which is also proportional to its pumping speed [10] [11]. Sensitivity is influenced by a number of factors, including the geometry of the cell (*viz.*, diameter, length and anode-cathode gap), pressure, the applied voltage and the magnetic field. The discharge modes of a Penning cell—which determine the properties of the plasma—also vary as a function of these parameters. The pumping speed of a SIP is thus not constant but changes over its working pressure range and it is influenced by the applied voltage and magnetic field. An in-depth explanation about sensitivity and discharge modes was made by Welch [5]. Several studies have been devoted to the optimisation of these parameters and to the investigation of their influence on pumping speed and sputtering inside the Penning cell [12] [13] [14] [15] [16] [17] [18] [19]. A number of attempts have also been made in order to model the pumping performance of SIPs as a function of certain parameters [20] [21].

2.2. Pumping mechanisms of SIPs

Once created by the Penning discharge, gas ions can be pumped by means of different mechanisms, all ascribable to two main families: *chemisorption*, which involves the formation of chemical bonds between the gas and a chemically active layer, and *physisorption*, gathering all the other processes.

Chemisorption involves pumping by dissociation and diffusion into the cathodes or, alternatively, by dissociation on a sputtered getter film and formation of stable chemical bonds with it. On the other hand, physisorption comprises burying of gas atoms beneath a sputtered film, implantation of high-energy neutrals in the cathodes or elsewhere, atomic diffusion through defects and interstitials and, finally, surface adhesion due to van der Waals forces. All the above-listed mechanisms are direct consequences of sputtering, which acts thus as the main driving force for gas pumping in a SIP. Different gas species are pumped according to distinct mechanisms, depending on their nature.

2.2.1. Getterable gases

The pumping of chemically-reactive gases (*viz.*, N_2, CO, O_2 and CO_2) involves two distinct chemisorption processes.

Gas ions created by electron impact in the Penning discharge are accelerated towards the cathodes and can be captured by impingement and burial inside the cathode material, below its first atomic layers.

The impinging ions, in addition, sputter material from the cathode, which subsequently deposits elsewhere inside the pump. The second and main sorption mechanism is based on the gettering capability of these sputtered films and involves the formation of stable chemical bonds between them and gas molecules. It is well-known, as a matter of fact, that pressure in a vessel can be reduced by evaporating chemically-reactive metals, which combine with the residual gas molecules [13].

A metal should of course have enough chemical affinity with the gas in order to dissociate its molecules and to form stable compounds (*viz.*, oxides, carbides, nitrides) with its constituent atoms. Chemical adsorption is an exothermic process: among several metals, Ti and Ta are favourite in terms of heat

of chemisorption [22] and therefore have been chosen as cathode materials for SIPs.

These sputtered films are mainly located on the inner surface of the anodes, whose change in composition, thickness and morphology can be analysed by means of several surface analysis techniques [23] [24]. Also a change in colour due to the deposited film is clearly recognisable even after few hours of pumping.

Sputtered films, in addition, can be deposited also on the opposite cathode; however, they are able to stably grow and act as getters only in areas where sputtering is in turn low. Finally, a getter film can form also elsewhere inside the pump body, wherever the process is allowed by sputtering conditions.

The continuous refreshment of this getter film is ensured by sputtering of the cathode material provoked by high-energy gas ions created into the Penning discharge. The working life of a SIP is generally determined by the erosion of the cathodes caused by sputtering. The pumping performances of the deposited film are determined by the equilibrium between its regeneration through sputtering and its consumption through gettering; in this framework, pumping Ar (which has a high sputter yield) for a certain time results in an improved SIP pumping speed for getterable gases, which lasts until equilibrium is restored [25].

Desorption of gas pumped by this mechanism is very unlikely, due to the strength of the chemical bonds and to the progressive deposition of new, sputtered metal layers one over the other. On the other side, ions buried inside the cathodes might be subsequently reemitted, as cathode erosion induced by sputtering progresses [26]. A stable and permanent pumping by burial into the cathodes is therefore possible only in areas where sputtering does not prevail and where deposition of cathode material exceeds the erosion rate, namely at the fringe areas along the anode projections [27]. Cathodes are indeed not uniformly sputtered while pumping but display a pattern of eroded and deposited area, whose shape and distribution depend on several parameters, *viz.* gas pressure, cell geometry, electric field and magnetic field [12] [28].

2.2.2. *Hydrogen*

In spite of being a getterable gas as the previous ones, H_2 deserves a separate discussion because it is mainly pumped according to a different mechanism. Due to its small mass, the pumping of H_2 by sputtered getter films is limited by its very

low sputter yield [29] [30] [31], which cannot ensure a sufficient production and refreshment of the sputtered getter film.

H_2 pumping is instead mostly given by dissociation at the cathode surface of the ionised molecules ($H_2^+ + e^- \rightarrow H + H$), followed by diffusion into the bulk material, driven by the concentration gradient with the cathode surface [30]. Dissociation has a great importance because only few percent of the ions created by the Penning discharge are H^+, the majority being instead H_2^+ [5].

This model for the pumping of H_2 is of course strictly dependent on diffusivity and solubility of the gas into the cathode material. The crystal structure becomes thus essential when considering the best cathode materials for H_2 pumping. It has been noted that greater H_2 capacity can be achieved when Ti alloys stabilised in their body-centred cubic (BCC) form are employed, instead of the hexagonal close-packed (HCP) structure of pure Ti. Cathodes made of Ti6Al4V alloy, for instance, were found to perform much better than others made of pure Ti, both in terms of pumping speed and capacity [5].

The sorption of significant quantities of H_2 leads to the formation of macroscopic fissures [31]; when pure Ti transforms into TiH_2, density decreases and the HCP crystal lattice becomes face-centred cubic (FCC), causing distortions and cracks in the material.

If the cathode surface is contaminated by other compounds, such as oxides or nitrides, dissociation and diffusion into the bulk are inhibited and pumping speed drops. Sputtering is therefore necessary in order to obtain a clean cathode surface and to promote this pumping mechanism. As the sputtering yield of H_2^+ ions is very low, however, it takes a long time to sufficiently scrub the cathodes, and thus to increase pumping speed until its maximum saturation value, when pumping pure H_2.

If a small fraction of a contaminant such as N_2 is present in the residual gas, a single adsorbed monolayer of impurities is sufficient to stop surface dissociation and diffusion into the bulk, resulting in a consistent decrease of H_2 pumping speed. If N_2 increases above 10%, however, H_2 pumping speed increases too: in this case, the high sputtering yield of N_2 prevents the formation of an impurity layer at the surface and, in addition, it enhances the formation of a getter film, which gives an additional contribution to the pumping of H_2 [32]. In general, if H_2 is pumped in a mixture with other gases, the much higher sputtering provoked by these latter is responsible for both release of H_2 molecules previously-pumped at the cathodes and enhanced sorption by sputtered films at the anodes; the resulting

overall pumping speed might be considerably higher or lower, compared to pure H_2, and strongly depends on pressure, gas composition and temperature [32] [33].

It has been demonstrated that, when pumping H_2, pressure plays a leading role in influencing pumping speed. Using different cathode materials, at low H_2 pressure (*i.e.*, below 10^{-8} Torr), the pumping performances are always the same and, since each material has its characteristic diffusivity and solubility of H_2, it follows that these physical properties are not relevant for H_2 pumping at low pressure [32]. On the other hand, at high pressure (*i.e.*, over 10^{-5} Torr) H_2 pumping is diffusion limited and pumping speed decreases with increasing pressure [5]. Since H_2 causes relatively little sputtering, and also because diffusion is involved as a pumping mechanism, it is not meaningful to specify an equilibrium pumping speed for pure H_2 [34].

2.2.3. Heavy noble gases

Noble gases are chemically inert and thus they cannot be chemisorbed; the first studies on SIPs identified ion implantation and burial into the cathodes as the main pumping mechanism for these gases [35]. This has been repeatedly proven by the use of radioactive tracers, like ^{131m}Xe [36] or ^{85}Kr [37] [28] [38]; pumping noble gases containing fractions of these isotopes allows detecting their distribution in the eroded patterns by means of autoradiography and Geiger-Müller counters.

Nevertheless, this mechanism might not be permanent due to the continuous cathode erosion produced by the incoming ions, which provokes the desorption of previously-buried atoms. It has been observed, in particular, that the radioactive tracer concentrates in correspondence of the anode edges, while the central part of each cell is continuously sputtered and thus cannot result in a permanent burial of inert gas atoms. For this reason, the balance between gas sorption and release from the cathodes results in a very limited pumping speed for these gases, corresponding to only 1–2% of that for N_2.

So-called *instability* phenomena are a direct consequence of this and have been early recognised as one of the main drawbacks of standard-diode SIPs [4]. Instability consists in periodic pressure bursts caused by sudden releases from the cathodes of previously-pumped Ar [39].

To a certain degree, noble gases can implant also in the anodes or in other parts of a SIP's inner surface [37]. Analyses with radioactive tracers demonstrated

that pumping at the anodes accounts for about 10–20% of the total in standard-diode SIPs [36] [28]. As it easy to understand, sorption of noble gases at the anode surface provides a much more stable pumping, due to the fact that anodes are not subject to erosion: once buried into them, desorption caused by sputtering cannot occur.

Several speculations have been made in the past about the possible reasons for the sorption of inert gases at the anodes [37], in order to possibly foster this pumping mechanism and to decrease the percentage of noble gas pumped at the cathodes. Among the others, the high-energy neutrals model was recognised as the most plausible mechanism and led to the development of noble-diode SIPs, as discussed in Section 2.3.1.

2.2.4.   Helium

The sorption of He by SIPs do not follow the same mechanisms explained in Section 2.2.3 for heavy noble gases. It has been found that only few % of He pumped by a diode SIP is normally buried inside the anodes and the pump body, whilst the most part of the sorbed gas is implanted in the cathodes [40].

The pumping of He seems to be mostly determined—as for H_2—by diffusion of gas molecules and ions into the cathodes. The main difference is however given by the fact that He molecules, unlike H_2 ones, cannot dissociate and form any kind of stable chemical compound (*e.g.*, hydrides) with the cathode materials. This predominant sorption of He at the cathodes explains why He pumping speed tends to decrease as the partial pressures of heavier gases increase: the higher sputter yield of these latter enhances the desorption from the cathodes of previously-pumped He [41].

As He atoms have very small dimensions and cannot be bounded by the cathode material, desorption of previously-pumped He from both cathodes and other surfaces of a SIP—unlike heavier noble gases—can take spontaneously place even at room temperature [42]. It has been repeatedly observed that, once a significant quantity of He has been pumped by a diode SIP, He re-emission might be detected for the rest of its working life [34]. At any given time, the overall He pumping speed is thus determined by the balance between the amount of gas pumped by the SIP and the quantity of previously-pumped gas desorbed from the components of the SIP itself.

2.2.5.   Hydrocarbons

Pumping of hydrocarbons basically involves cracking of the organic molecules by the Penning discharge, followed by pumping of the dissociated gas according to the usual mechanisms. This leads to the regurgitation of gaseous H_2 from the electrodes during sputtering [43]. For this reason, when CH_4 is pumped by a SIP, the residual gas composition can drastically change during time [44].

If pressure is sufficiently high, a prolonged pumping of hydrocarbons may result in the formation of a carbonaceous deposit on the cathodes; this layer is difficult to sputter and, once formed, it inhibits the continuous refreshment of the sputtered Ti film, thus resulting in a sharp decrease of pumping speed [45]. At lower pressure, instead, a SIP is able to efficiently pump hydrocarbons for longer times. In order to recover the initial pumping capacity, the carbonaceous layer must be dissolved by admitting O_2, which tends to form volatile compounds with the deposit. Reactivation relying on sputtering by N_2 or Ar, on the other side, was not proven to be effective.

2.3. Other types of SIPs

The pump developed by Hall is generally known as diode SIP and is made of an array of stainless-steel anodes comprised between two Ti cathode plates [2].

During the past decades, however, several other SIP configurations have been proposed and developed. Among them, noble-diode and triode SIPs are the only ones that obtained a broad diffusion in the vacuum technology community; other concepts did not have the same fortune and remained confined to the level of academic discussions and publications.

2.3.1.   Noble-diode pumps

As explained in Section 2.2.3, the main drawback of diode SIPs is the very limited pumping speed for noble gases provided by these devices, together with the short-term outbreak of instability phenomena.

Tom and James proposed in 1969 a *differential* SIP with one cathode made of Ti and one made of Ta or, in general, of a metal with high sputter yield [46]. This so-called noble-diode SIP was not affected by Ar instability (even after several weeks of pumping against an Ar leak in the 10^{-6} mbar range) and significantly increased the pumping speed for noble gases to about 25% of the nominal speed for N_2. Their explanation for this particular behaviour was that reemission of noble gases from a cathode can be greatly reduced by deposition of material sputtered from the opposite cathode with higher sputter yield. However, these observations were not consistent with the fact that, for a broad range of ion energies, sputter yields of Ti and Ta are very similar [47].

As already mentioned, several theories had previously been outlined in order to account for the fact that part of noble gas pumping by standard-diode SIPs occurs at the anode surface [37]; most of them involved the burial of high-energy neutrals, whose origin was however still debated.

The differential ion pumping model proposed by Tom and James was later refuted by Jepsen, who first described the actual origin of high-energy neutral and their improved sorption mechanism in noble-diode pumps [4] [48].

According to his theory, noble gas ions created in the Penning discharge are accelerated towards the cathode and, upon impingement, they can be neutralised and reemitted via elastic scattering (Figure 2-1). These neutral particles keep part of the initial energy of incident ions and may afterwards implant in the anodes or somewhere else inside the pump body, where they are permanently buried because no sputtering occurs there.

The fraction of energy retained by neutrals depends on the masses of the bombarding gas species and of the cathode material (m_1 and m_2, respectively) according to the following equation, which derives from the conservation of kinetic energy and momentum in elastic collisions [49]:

$$\frac{E_1}{E_0} = \frac{\left[cos\,\vartheta \pm \sqrt{\left(\frac{m_2}{m_1}\right)^2 - sin^2\,\vartheta} \right]^2}{\left(1 + \frac{m_2}{m_1}\right)^2}$$

Where θ is the scattering angle of the incident particle, E_0 is its initial kinetic energy and E_1 its kinetic energy after scattering. If $m_2 < m_1$, backscattering cannot occur and only the forward direction is allowed ($\theta < \pi/2$).
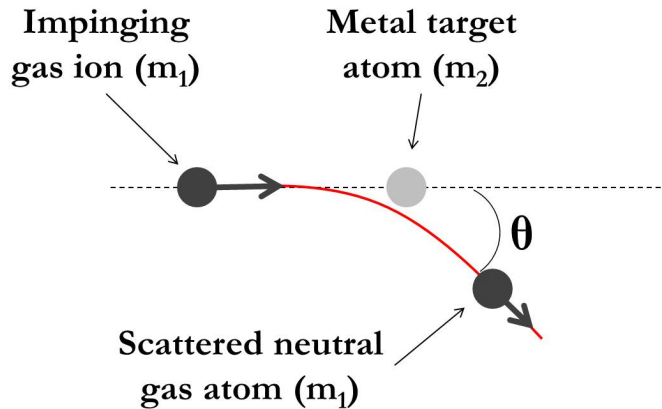
Figure 2-1 – Elastic scattering of high energy neutrals.

In the case of diode SIPs with flat Ti cathodes, Ar ions strike nearly at normal incidence and most of them are scattered in the forward direction, due to the fact that Ti atomic mass is only slightly higher than that of Ar (48 u *vs.* 40 u, respectively); the fraction of backscattered Ar atoms retains less than 10% of the initial energy [5]. Conversely, Ta has an atomic mass much higher than that of Ti (181 u *vs.* 48 u, respectively). For this reason, the use of a Ta cathode promotes backscattering and also allows to increase the average fraction of energy retained by reflected neutral, which in this case can be up to 64% of the initial one [5]. Once re-emitted from the cathodes, Ar neutrals are thus able to implant more deeply (that is, more stably) into the anodes or other surfaces of the pump. As a result, noble-diode SIPs with a Ti and a Ta cathode are immune from instability and provide higher pumping speeds for Ar compared to diode ones.

These results are confirmed by further studies focused on sputtering and sputter deposition using noble gases: it has been observed that a high flux of high-energy neutrals is established when the atomic mass of gas atoms is lower than the target material, leading to the growth of sputtered films with a high concentration of substitutionally-included noble gas atoms [50].

In the case of He, due to its light atomic mass, there is little if any difference between the energies retained by neutrals off of Ti and Ta cathodes; this in turn results in the fact that the use of noble-diode SIPs instead of diode ones do not give any significant advantage in terms of He pumping speed [40].

2.3.2.   Triode pumps

Shortly after the first appearance of diode SIPs, a triode concept—in which cathode and anode were flanked by a collector plate with a different voltage—was proposed [27]. Compared to diode SIPs, triode pumps were found to provide higher pumping speeds for Ar (up to 25% of that of air) and to be immune to Ar instability. The triode layout was later refined: a cathode grid was placed between the anode and the vacuum envelope acting as a collector, where ions are pumped. Triode SIPs exploit the dependence of backscattering energy on incident angle between projectile and target.

For most metals the sputtering rate increases as the energy of the incident ions increases. Furthermore, ions incident at a grazing angle do more sputtering than those which strike the surface at normal incidence [27]. Most of the ions impinging on the cathode grids do so at grazing incidence. Therefore—regardless of the adopted cathode material [51]—a deflected, neutralised ion retains much of its original kinetic energy and becomes buried in the walls of the pump. Post-cathode SIPs [34] and multi-holed cathode ones [52] also rely on this principle.

Gas	Diode	Triode
N_2	100	100
H_2	200	180
O_2	100	100
CO	100	100
CO_2	100	100
Air	100	100
He	1	30
Ar	3	22

Table 2-1 – Pumping speeds of diode and triode SIPs for different gases, expressed as percentage of the value for N_2.

The major breakthrough in the field of triode SIP was made in the 1980s by Pierini and Dolcino, who proposed an innovative cathode element which is cheaper and easier to manufacture [53]. This solution is currently sold under the trade-name StarCell®.

2.4. Memory effects of SIPs

Unlike mechanical pumps, which are able to provide a constant pumping speed for every gas at a given pressure, the performances of a SIP are severely influenced by a number of factors and thus they can greatly vary over time. At any given moment, the overall pumping speed of a SIP results from the equilibrium between gas species adsorbed on the inner surfaces of the pump and desorbed from them. Cathodes and anodes represent the preferential sorption sites for most of the gas species in a SIP; while the implantation in the anodes is permanent, cathodes are instead prone to sputtering by the incoming ions and hence their erosion might cause a continuous re-emission of previously-buried gas atoms. The extent of this phenomenon is strictly dictated by several interdependent factors, including the sputter yield of the gas ions, the fraction of gas molecules already pumped inside the cathodes and their implantation depth. An eventual chemical cleaning or vacuum firing of the electrodes prior to the first ignition of the pump has also an influence on the outgassing [54].

The pumping speed provided by a SIP is thus influenced by its previous sorption history [33]; gases that are mainly sorbed inside the cathodes (like H_2 and He) might be easily released if these latter are subsequently bombarded by a heavy gas with a high sputtering effect. Noble gases, in particular, are prone to be released due to their inability to form strong chemical bonds with the cathode material [55] [56] [34] [57].

This kind of regurgitation phenomena might be exploited in order to obtain a positive effect on the efficiency of a SIP: pumping speed of a SIP for a certain gas, as well as its overall capacity, can be restored with the adsorption of a large quantity of another gas with a high atomic mass number. This mechanism—commonly known as *purging*—stimulates the release from the cathodes of previously-sorbed species, which afterwards can be more permanently pumped elsewhere, *e.g.* by implantation of high-energy neutrals. From this point of view, Ar is the most effective among the gases commonly pumped by SIPs: thanks to its high sputtering effect on the cathode materials, Ar is able to provoke a relevant regurgitation, thus efficiently purging a SIP. In addition, the intense sputtering caused by Ar purging creates a fresh layer of getter material on the inner surfaces of a SIP, which results in a significant increase of its pumping speed for getterable gases; since Ar is not getterable, it produces this sputtered layer but it does not give any contribution to its subsequent saturation. Other gases (*e.g.*, N_2 and O_2) or

combinations of two can also be used to purge a SIP; however, the best results are usually obtained with Ar.

In general, when a SIP starts to pump a gas, there is an initial transient during which a high pumping speed is observed. As the pumping goes on, this effect tends to vanish and pumping speed approaches its saturation value [4]. This is due to the fact that, at the beginning, most part of the gas is pumped through ion burial into the cathodes and there is little if any gas release from the cathodes themselves. Afterwards, the concentration of gas in the atom layers beneath the surface increases and the outgassing from the cathodes through sputtering tends to balance the ion burial. If another gas species is then introduced, a new transient occurs until equilibrium is reached again.

References

[1] A. Gurewitsch and W. Westendorp, "Ionic Pump," *Rev. Sci. Instrum.,* vol. 25, p. 389, 1954.

[2] L. Hall, "Electronic Ultra-High Vacuum Pump," *Rev. Sci. Instrum.,* vol. 29, no. 5, pp. 367-370, 1958.

[3] L. Hall, J. Helmer and R. Jepsen, "Electrical Vacuum Pump Apparatus and Method". Patent U.S. Patent No. 2,993,638, 1957.

[4] R. L. Jepsen, "The physics of sputter-ion pumps," in *Proc. 4th Int. Vacuum Congr.*, London, 1968.

[5] K. Welch, Capture pumping technology - An introduction, Oxford: Pergamon Press, 1991.

[6] J. Plücker, *Poggendorffs Ann.,* vol. 103, p. 88, 1858.

[7] L. Vegard, *Ann. Phys. (Leipzig),* vol. 4, p. 769, 1916.

[8] W. Gaede, "Tiefdruckmessungen," *Zeitschr. f. Techn. Physik,* vol. 12, p. 664, 1934.

[9] F. M. Penning, "Ein neues manometer für niedrige gasdrucke, insbesondere zwischen $10-3$ und $10-5$ mm," *Physica,* vol. 4, no. 2, pp. 71-75, 1937.

[10] R. Jepsen, "Important characteristics of a new type getter-ion pump," *Le Vide,*

vol. 14, p. 80, 1959.

[11] S. Rutherford, "Pumping speed measurement on sputter-ion pumps," *Vacuum,* vol. 16, no. 12, pp. 643-646, 1966.

[12] J. Helmer and R. Jepsen, "Electrical Characteristics of a Penning Discharge," *Proc. of the IRE,* vol. 49, no. 12, pp. 1920-1925, 1961.

[13] L. Holland, "Theory and design of getter-ion pumps," *J. of Sci. Instr.,* vol. 36, pp. 105-116, 1959.

[14] L. Lamont, "Physical processes in the Penning discharge from E-8 Torr to E-3 Torr," *J. Vac. Sci. Technol.,* vol. 4, no. 5, p. 339, 1967.

[15] W. Knauer, "Mechanism of the Penning discharge at low pressures," *J. Appl. Phys.,* vol. 33, no. 6, pp. 2093-2099, 1962.

[16] T. Chou and D. McCafferty, "Pumping behavior of sputter ion pumps," *J. Vac. Sci. Technol.,* vol. 18, no. 3, pp. 1148-1151, 1981.

[17] K. Wear, "Electrical characteristics of sputter-ion pumps," *J. Appl. Phys.,* vol. 38, no. 4, pp. 1936-1940, 1967.

[18] R. Jepsen, "Magnetically confined cold cathode gas discharges at low pressures," *J. Appl. Phys.,* vol. 32, p. 2619, 1961.

[19] L. Lamont, "A model for the Penning discharge in the neighbourhood of the transition point," *Proc. of the 4th Internl. Vacuum Congress,* pp. 345-348, 1968.

[20] H. Hartwig and J. Kouptsidis, "A new approach for computing diode sputter-ion pump characteristics," *J. Vac. Sci. Technol.,* vol. 11, no. 6, pp. 1154-1159, 1974.

[21] T. Ha, S. Chung and C. Park, "Optimization of cell geometry for a conventional sputter ion pump by a particle-in-cell simulation," *J. Vac. Sci. Technol. A,* vol. 27, p. 485, 2009.

[22] E. Miyazaki, "Chemisorption of diatomic molecules (H2, N2, CO) on transition d-metals," *J. Catal.,* vol. 65, no. 1, pp. 84-94, 1980.

[23] A. Vesel, M. Mozetic, J. Kovac and A. Zalar, "XPS study of the deposited Ti layer in a magnetron-type sputter ion pump," *Applied Surface Science,* vol. 253, pp. 2941-2946, 2006.

[24] A. Vesel, M. Mozetic, J. Kovac and A. Zalar, "AES investigation of anode deposits in magnetron-type sputter ion pump," *Applied Surface Science ,* vol. 246, pp. 126-131, 2005.

[25] D. Andrew, "The performance assessment of sputter ion pumps," *Vacuum,* vol. 16, no. 12, pp. 653-657, 1966.

[26] E. Brown and J. H. Leck, *Brit. J. Appl. Phys.,* vol. 6, no. 5, p. 161, 1955.

[27] W. Brubaker, "A method for greatly enhancing the pumping action of a Penning discharge," in *Proc. 6th Nat. AVS Symp.*, 1959.

[28] D. Andrew, D. R. Sethna and G. F. Weston, "Inert-gas pumping in a magnetron pump," *Vacuum,* vol. 18, no. 3, p. 136, 1968.

[29] J. H. Singleton, "Hydrogen pumping by sputter-ion pumps and getter pumps," *J. Vac. Sci. Technol.,* vol. 8, no. 1, pp. 275-282, 1971.

[30] K. M. Welch, D. J. Pate and R. J. Todd, "Pumping of helium and hydrogen by sputter-ion pumps. II. Hydrogen pumping," *J. Vac. Sci. Technol. A,* vol. 12, no. 3, pp. 861-866, 1994.

[31] S. L. Rutherford and R. L. Jepsen, "Enhanced hydrogen pumping with sputter-ion pumps," *Rev. Sci. Instrum.,* vol. 32, no. 10, p. 1144, 1961.

[32] J. H. Singleton, "Hydrogen pumping speed of sputter-ion pumps," *J. of Vac. Sci. Technol.,* vol. 6, no. 2, pp. 316-321, 1969.

[33] M. Audi and M. De Simon, "The influence of heavier gases in pumping helium and hydrogen in an ion pump," *J. Vac. Sci. Technol. A,* vol. 6, no. 3, pp. 1205-1208, 1988.

[34] L. Lamont, "A novel diode sputter-ion pump," *J. Vac. Sci. Technol.,* vol. 6, no. 1, pp. 47-51, 1969.

[35] L. Hall, "Electronic Ultra-High Vacuum Pump," *Rev. Sci. Instr.,* vol. 29, no. 5, pp. 367-370, 1958.

[36] K. Kawasaki, T. Sugita, I. Kohno, J. Watanabe and N. Hayashi, "Clean up of inert gases in a Penning discharge studied by a tracer technique," *J. Appl. Phys.,* vol. 35, no. 3, pp. 479-482, 1964.

[37] J. M. Lafferty and T. A. Vanderslice, "The interplay of electronics and vacuum technology," *Proc. IRE,* vol. 49, pp. 1136-1154, 1961.

[38] D. Andrew, "The role of energetic neutrals in a magnetron sputter ion pump," *J. Phys. D,* vol. 2, no. 11, pp. 1609-1615, 1969.

[39] J. A. Vaumoron and M. P. De Biasio, "Argon and rare gas instability with heavy metal cathode Penning Pumps," *Vacuum,* vol. 20, no. 3, pp. 109-111, 1970.

[40] K. M. Welch, D. J. Pate and R. J. Todd, "Pumping of helium and hydrogen by sputter-ion pumps. II. Helium pumping," *J. Vac. Sci. Technol. A,* vol. 11, no. 4, pp. 1607-1613, 1993.

[41] M. Audi and M. De Simon, "The influence of heavier gases in pumping helium and hydrogen in an ion pump," *J. Vac. Sci. Technol. A,* vol. 6, no. 3, pp. 1205-1208, 1988.

[42] E. Brown and J. H. Leck, "Desorption of gas in the cold cathode ionization gauge," *Brit. J. of Appl. Phys.,* vol. 6, no. 5, pp. 161-164, 1955.

[43] A. Frennet and G. Liénard, "Analyse de mélanges hydrocarbure-deutérium à l'aide d'un spectromètre de masse évacué par une pompe ionique," *Le vide,* vol. 142, pp. 239-243, 1969.

[44] F. Williams, M. Boudart and A. Frennet, "Backstreaming of hydrogen when pumping hydrocarbons with an ion pump," *J. Vac. Sci. Technol.,* vol. 9, no. 1, pp. 362-365, 1972.

[45] J. E. Kelly and T. A. Vanderslice, "Pumping of hydrocarbons by ion pumps," *Vacuum,* vol. 11, no. 4, p. 205, 1961.

[46] T. Tom and B. D. James, "Inert gas ion pumping using differential sputter yield cathodes," *J. Vac. Sci. Technol.,* vol. 6, no. 2, pp. 304-307, 1969.

[47] N. Laegreid and G. K. Wehner, "Sputtering yields of metals for Ar+ and Ne+ ions with energies from 50 to 600 eV," *J. Appl. Phys.,* vol. 32, no. 3, pp. 365-369, 1961.

[48] I. Brodie, L. T. Lamont and R. L. Jepsen, "Production of high-energy neutral atoms by scattering of ions at solid surfaces and its relation to sputtering," *Phys. Rev. Lett.,* vol. 21, no. 17, pp. 1224-1226, 1968.

[49] C. Snoek and J. Kistemaker, "Fast ion scattering against metal surfaces," *Advances in electronics and electron physics,* vol. 21, pp. 67-99, 1966.

[50] B. Window, "Removing the energetic neutral problem in sputtering," *J. Vac. Sci. Technol. A,* vol. 11, no. 4, pp. 1522-1527, 1993.

[51] Liu.

[52] S. Komiya and N. Yagi, "Enhancement of noble gas pumping for a sputter-ion pump," *J. Vac. Sci. Technol.,* vol. 6, no. 1, pp. 54-57, 1969.

[53] M. Pierini and L. Dolcino, "A new sputter ion-pump element," *J. Vac. Sci. Technol. A,* vol. 1, no. 2, pp. 140-142, 1983.

[54] A. Calcatelli, M. Bergoglio, P. Mohan, M. Spagnol and M. De Simon, "Study of outgassing of sputter-ion pump materials threated with three different cleaning procedures," *Vacuum,* vol. 47, no. 6-8, pp. 723-726, 1996.

[55] J. H. Carmichael and P. M. Waters, "Re-emission of ionically pumped helium by helium ion bombardment," *J. Appl. Phys.,* vol. 33, no. 4, pp. 1470-1474, 1962.

[56] B. Cobic, G. Carter and J. H. Leck, "Comprehensive study of the ion pumping of the noble gases," *Brit. J. Appl. Phys.,* vol. 12, pp. 288-292, 1961.

[57] G. H. Li and S. Xu, "New research on re-outgassing of SIP," *Vacuum,* vol. 41, no. 7-9, pp. 2073-2075, 1990.

[58] J. M. Lafferty, Foundations of vacuum science and technology, John Wiley & Sons, Inc., 1998.

3. SIP+NEG coupling

3.1. Basics of the SIP+NEG coupling

New pumps, based on the coupling of a NEG and a SIP element, have been introduced in order to obtain a higher overall pumping speed without increasing the pump dimensions. This kind of SIP+NEG combination pumps has been adopted in a number of accelerator facilities all over the world [1] [2] [3].

The idea of a SIP+NEG combination pump takes advantage of the complementarity of these two technologies. NEG pumps provide high pumping speed for all the getterable gases (*viz.*, H_2, H_2O, CO, N_2, O_2, and CO_2); they do not need electrical power during their functioning (except for the initial activation of the getter) and they are very compact, vibration-free and lubricant-free devices. However, they cannot sorb noble gases and their pumping speed for hydrocarbons is negligible. On the other side, SIPs are able to pump both getterable and non-getterable gases—that is, hydrocarbons and noble gases—even if the sorption of these latter is liable to a number of drawbacks (limited pumping speed, instability, …). As already mentioned in Chapter 2, noble-diode SIPs partially remedy these aspects: their noble-gas sorption rates are higher and they are immune from instability, but pumping speeds provided for N_2 and other chemically-active gases become usually lower compared to diode pumps. One main advantage of SIPs is that they can be switched on already at relatively high pressures, starting from the HV range (10^{-5} Torr), so that they are suitable also for unbaked systems. However, also NEG pumps can be effectively used when pressure is higher than the UHV range, provided that they work at a sufficiently high temperature (200–300 °C) in order to ensure a greater sorption capacity. In baked systems working in the UHV pressure range, if large pumping speeds and capacities are required, NEG pumps

are in any case preferable, due to the very large size, great weight and voluminous magnets that a SIP ensuring the same sorption rates would imply. Furthermore, pumping speed of a SIP for a certain gas depends on the working pressure and it decreases as pressure drops, so that the effective sorption rate provided by a SIP in the UHV range is usually far less than its nominal value [4], which is conventionally the highest one measured in the range between the lowest achievable pressure and 10^{-3} Pa [5]. This problem is particularly evident in the case of H_2, which is normally the main residual gas in typical UHV-XHV baked systems and whose SIP pumping speed is susceptible to a rapid decrease as pressure goes below $1 \cdot 10^{-6}$ Pa [6].

Conversely, it has been proven that H_2 pumping speed of a NEG pump does not vary with pressure. Figure 3-1 shows for instance the performance for H_2 of a CapaciTorr$^\circledR$ D100 pump in a Fischer-Mommsen dome as a function of the residual pressure: by progressively increasing the H_2 flux entering the system, the sorption rate was constant from $1 \cdot 10^{-10}$ mbar to $4.5 \cdot 10^{-5}$ mbar and equal to 110 l/s. The only exception was represented by the first point below $1 \cdot 10^{-10}$ mbar, which was too close to the base pressure of the system and where the influence of CH_4 and other residual gases was still sizeable.
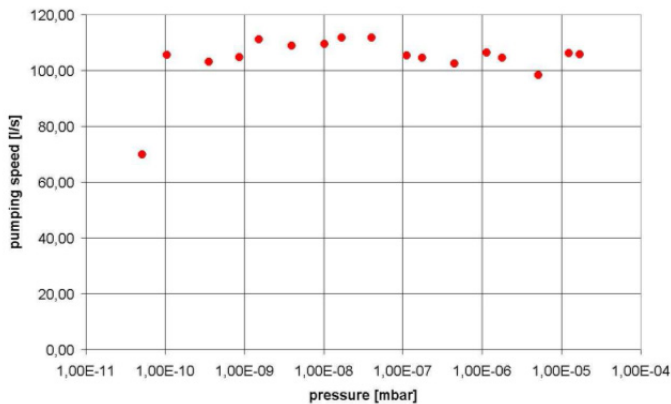
Figure 3-1 – H$_2$ pumping speed of CapaciTorr® D100 NEG pump, measured as a function of pressure in a baked Fischer-Mommsen dome (courtesy of Lukas Urban, GSI, Darmstadt, Germany).

3.2. **Performance issues of NEG elements inside SIPs**

The first approach to the combination pump consisted in the installation of a NEG element (*viz.*, a strip, a module, or a cartridge) inside the body of a SIP through an appropriate flange (Figure 3-2a and Figure 3-2b) [7] [8].

Although being still sometimes adopted, this solution is actually not the best possible and it implies some major drawbacks, either placing the NEG pump inside a large SIP or using a small one. More details about these limitations are given in the following.
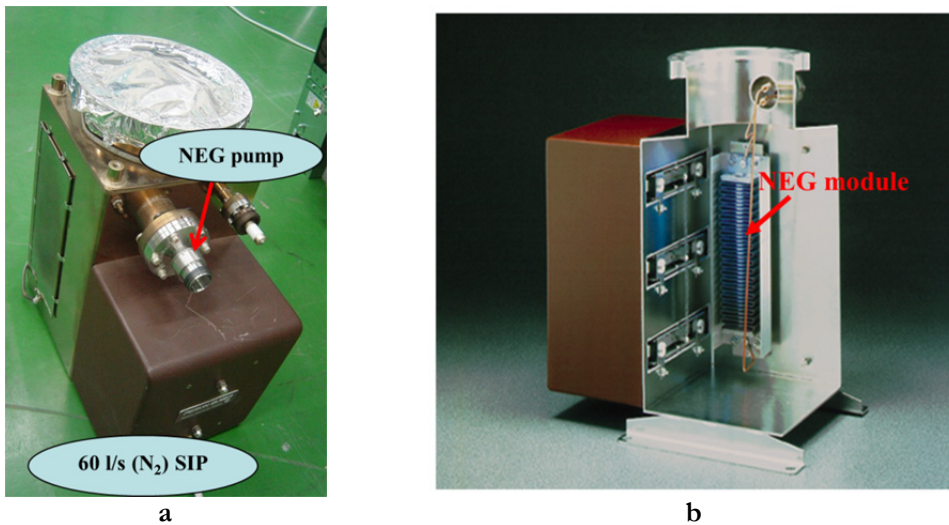
Figure 3-2 – a) Combination of a SIP and a NEG cartridge inside it [2]; b) combination of a SIP and a NEG module inside it (courtesy of SSRF).

3.2.1. NEG elements inside conductance-limited SIPs

The following practical example demonstrates how the performance of a SIP+NEG combination pump—when considering the sorption of certain gases—might be dramatically influenced by the geometry and the mutual positioning of the two pumping elements, regardless of their characteristic sorption rates.

In this case, a NEG cartridge was installed inside the body of a small SIP ensuring a nominal pumping speed of 20 l/s for N_2, between the pump inlet and

the electrode array; the nominal initial pumping speeds of the NEG were 70 l/s and 340 l/s for N_2 and H_2, respectively. The SIP was connected to the experimental vacuum system through a 4.5 cm long CF35 inlet flange, which resulted in an inlet conductance for N_2 of 52 l/s according to Clausing's formula for short circular ducts. Moreover, a further conductance determined by the test-bench had to be taken into account (*i.e.*, a zero-length junction from CF35 to the main volume of the vacuum system), so that the overall inlet conductance was equal to only 42 l/s.

The pumping performances of both configurations (SIP only and SIP+NEG) have been evaluated for different gases, in compliance with the standard testing procedures described in Chapter 5. Pumping speed S (in l/s) of each configuration for each gas has been plotted against the quantity Q of sorbed gas (in Torr·l), keeping a constant pressure value inside the vacuum chamber.
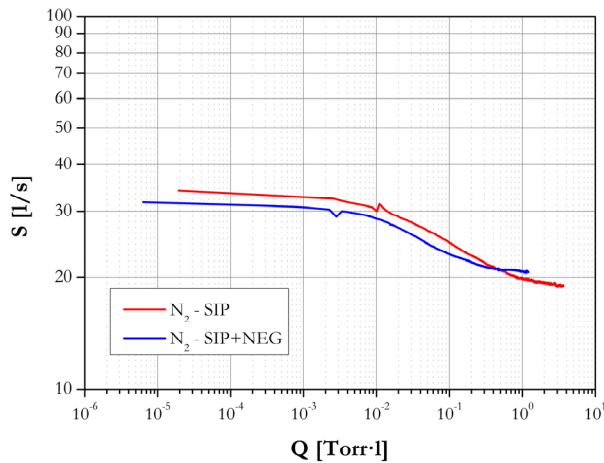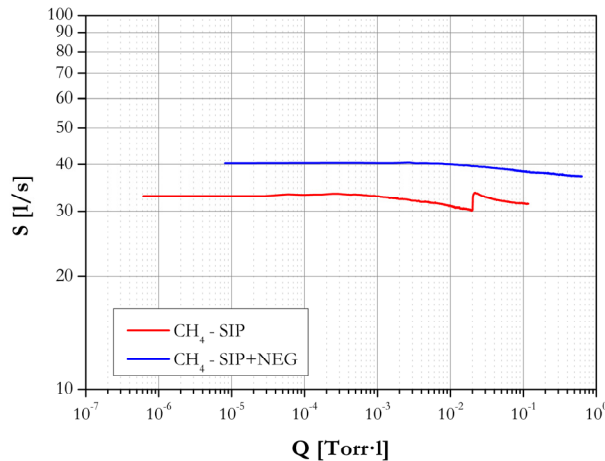

Figure 3-3 – N_2 pumping speeds of the SIP only and of the SIP with a NEG cartridge inside.

Figure 3-3 shows the N_2 pumping speed measured using the SIP only, together with the one obtained with both the SIP and the NEG cartridge inside it. Little if any difference was found between these two curves, despite the theoretically-large N_2 pumping speed contribution of the NEG pump. As the NEG cartridge was placed upstream of the conductance, the pumping speed of

the NEG+SIP combination was limited by the conductance itself. This explains why even the initial value observed in this configuration (about 31 l/s) was much lower than the nominal pumping speed of the NEG (70 l/s) and even slightly lower than the initial sorption rates given by the SIP only (about 34 l/s): the 42 l/s conductance was able to completely suppress any beneficial influence of the NEG cartridge, albeit this latter was still fully activated.

At the end of the test ($Q>1$ Torr·l), pumping speed of the SIP reached a constant value close to its nominal pumping speed of 20 l/s. At the same position, pumping speed of the SIP+NEG combination was only slightly higher and, in any case, much lower than the 42 l/s inlet conductance. As a matter of fact, N_2 pumping speed of this type of NEG cartridge starts from 70 l/s but it is normally reduced to 10 l/s after the sorption of 0.1 Torr·l of gas; at the end of the test, even if used in combination with the SIP, the NEG pump was thus probably partially or totally saturated, so that most part of the overall pumping speed was ensured by the SIP.

Figure 3-4 – CH$_4$ pumping speeds of the SIP only and of the SIP with a NEG cartridge inside (the bump on the red curve was given by a sudden release of previously-pumped gas).

On the other side, when considering H_2, the corresponding inlet conductance was much larger (158 l/s). This is the reason why a significant

increase in the sorption performance was instead noticeable when pumping H_2 with the SIP+NEG in place of the SIP only: about 110 l/s were measured using the combination pump, while it is known that H_2 pumping speed of a SIP can be up to 1.5 times higher than its nominal N_2 pumping speed, which in this case was 20 l/s.

In accordance with this, Figure 3-4 shows that CH_4 pumping speed of the SIP+NEG combination was remarkably higher compared to the SIP only, due to the NEG contribution in the sorption of H_2 resulting from CH_4 cracking in the Penning cells of the SIP.

The example of this specific SIP+NEG coupling gives a clear indication of the important role played by the geometry when considering a combination pump, where the NEG cartridge is simply installed inside the SIP through an appropriate flange. Depending on the dimensions of the inlet conductance and on the mutual position of the NEG cartridge and the SIP's electrodes, the beneficial effects of the SIP+NEG coupling might be strongly reduced or even completely lost, especially when N_2, CO, or CO_2—which are more demanding from the conductance point of view—are pumped. This is particularly true when small SIPs like this 20 l/s one are taken into account, due to the strong limitations on the maximum possible dimensions of the NEG element and to the severe impact of their inlet conductances (CF63 or lower) on the NEG performance.

3.2.2.   NEG elements inside large SIPs

On the other hand, NEG pumps placed inside large SIPs have also been studied and adopted [1] [2], in particular when large gas loads are expected and strict pressure requirements are necessary.

Among the others, a combination pump made of a NEG cartridge (CapaciTorr® D400, providing 400 l/s for H_2 and 100 l/s for N_2) mounted inside a 400 l/s diode SIP has been the object of a recent investigation for a new accelerator facility—the *Heavy Ion Medical Machine* (HIMM)—which is currently under construction in Lanzhou, China[1].

---

[1] J. Meng, C. Luo, Z. Chai, Z. Hu, X. Ma, W. Xie, W. Yang, X. Zhang, F. Siviero, L. Caruso, T. Porcelli, P. Manini, E. Maccallini, "Use of combined sputter ion and NEG pumps in the heavy ion medical machine", *Vacuum* **114** (2015) 108-113.
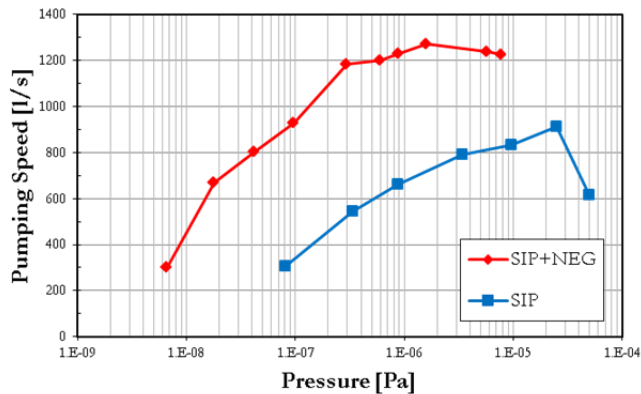
a
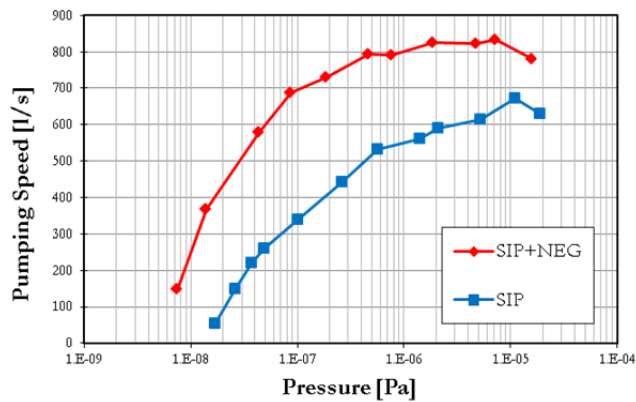
b

Figure 3-5 – Pumping speeds of SIP+NEG and of the SIP only, measured by injecting gas at different pressure levels in a baked test dome: a) H_2; b) N_2.

Heavy-ion beams will be accelerated in a synchrotron ring, in which the average pressure should be kept below $5 \cdot 10^{-7}$ Pa in order to guarantee the required beam storage lifetime. The entire vacuum system is about 170 m long. The choice of SIP+NEG combination pumps is dictated by the fact that, in order to ensure the attainment of the required UHV base pressure after bake-out in a reasonable time by using only SIPs, very large pumps would be necessary; this is due to already-mentioned substantial decrease of a SIP's sorption rate as pressure goes below $1 \cdot 10^{-6}$ Pa. However, this solution would not be feasible, since the space left for vacuum pumps in the HIMM is greatly limited by the size of the synchrotron magnets.

Test on the proposed SIP+NEG combination pump demonstrated that it allows to attain a better ultimate pressure level in a shorter pump-down time compared to the sole SIP ($1.7 \cdot 10^{-9}$ Pa after 24 h *vs.* $3.4 \cdot 10^{-9}$ Pa after 48 h, respectively). This means that, using the SIP+NEG layout, the pump-down time might be reduced or, alternatively, a shorter bake-out at lower baking temperature might be introduced (currently it consists in heating up to 250 °C for 40 h). The NEG pump was activated immediately after the bake-out, when temperature had dropped to 80 °C.

N_2 and H_2 sorption tests made by injecting gas at different pressure levels in a test dome between 10^{-8} Pa and 10^{-4} Pa—according to the ISO/DIS standard for SIP pumping speed measurements [5]—confirmed the higher pumping speeds expected for the combination pump in comparison to the SIP only (Figure 3-5a and Figure 3-5b); for both gases, the increment was in line with the sorption rates ensured by the NEG cartridge. At high pressure, the lifetime of the NEG pump is of course shorter than in the UHV range, if the getter is kept at room temperature; the values of Figure 3-5 measured at $P > 1 \cdot 10^{-6}$ Pa might thus be affected by a partial saturation of the NEG.

If a NEG pump is installed in a large SIP, unlike the previous case, its sorption performances are thus not severely affected by the inlet conductance, since the use of wide inlet flanges becomes feasible (CF150 in the case of this 400 l/s SIP). However, even if a SIP ensuring the same pumping speed would be even heavier and bigger, the weight and size of the pumping group in this configuration are still sizeable: the 400 l/s SIP weights about 100 kg.

3.3. A new combination layout: the NEXTorr® pump

An improved version of the combination pump has been therefore studied and developed in recent years, driven by the need for extremely-compact and high-performing UHV pumps [9]; this new pump, patented and marketed by SAES Getters under the trade-name NEXTorr®, combines a NEG cartridge with a small SIP—N_2 nominal pumping speed is 5 l/s or 10 l/s, depending on the model—tasked with the pumping of non-getterable species only.

As noble gases and CH_4 are normally only a small fraction of the residual atmosphere in UHV and XHV conditions, a small and compact SIP is sufficient to

deal with them [2]. Indeed, in a system affected by ion-induced desorption and pumped by NEG pumps (like for instance the LHC), CH_4 degassing might be the limiting factor to the ultimate achievable base pressure. It has been demonstrated that the low 10^{-13} Torr range may be reached by using a SIP providing 10 l/s per m^2 of vacuum chamber surface for Ar and CH_4 [10] [11].

On the other side, the NEG pump is able to ensure very large pumping speeds (up to 2000 l/s for H_2 with the largest model) and capacities for getterable gases, despite its limited dimensions. Unlike the previous case, the NEG cartridge of a NEXTorr® is located outside the SIP body, more precisely in front of the SIP aperture and coaxial with it (Figure 3-6) [12]. This configuration optimises the synergy between the two devices: the NEG can intercept the gases released by the SIP, thus reducing any back-streaming effect from the SIP and improving the overall pumping performance of the combination [9] [13]. Further details about this synergic mechanism are given in Chapter 5—where the experimental setup is described—because it had repercussions on the choice of the way to characterise SIPs.

Figure 3-6 – From left to right: NEXTorr® D100-5, D200-5, D300-5, and D500-5.

As already mentioned, a large NEG cartridge ensuring high pumping speed and capacity would require the adoption of a bulky SIP able to host it inside its vacuum envelope; however, this would severely hinder the chance to increase the pumping performance while limiting the size of the SIP. From this point of view, the NEXTorr® layout represents a great step forward. Moreover, its integrated design allows an efficient exploitation of the possible synergies between the two

pumping elements: the inlet-conductance limitation is in this case avoided and the NEG cartridge is thus able to shoulder effectively the incoming loads of active gases.

In light of these considerations, a further improvement of the SIPs used in NEXTorr® pumps should focus on the sorption of noble gases—whose loads might be relevant in some specific applications—and on the occurrence of regurgitation phenomena, especially when pumping CH_4. These are indeed the scopes of this dissertation, which deals therefore with small SIPs analogous to those employed in NEXTorr® pumps.

References

[1] D. Jiang, "The vacuum system for Shanghai Synchrotron Radiation Facility (SSRF)," *J. Vac. Soc. Jpn.,* vol. 49, no. 12, pp. 754-756, 2006.

[2] C. Park, S. Chung and P. Manini, "Combination of compact nonevaporable getter and small ion pumps for ultrahigh vacuum systems," *J. Vac. Sci. Technol.,* vol. A, no. 29(1), 2011.

[3] G. Hsiung, H. Hsueh, L. Wu, C. Chang, C. Cheng, C. Chan and Y. Yang, "Vacuum systems for the TPS accelerator," *Vacuum,* vol. 121, pp. 245-249, 2015.

[4] M. Audi, "Pumping speed of sputter ion pumps," *Vacuum,* vol. 38, no. 8-10, pp. 669-671, 1988.

[5] I. 1. 3, "ISO/DIS 3556-1.2: Sputter-ion pumps - Measurement of performance characterstics," 1992.

[6] J. H. Singleton, "Hydrogen pumping speed of sputter-ion pumps," *J. of Vac. Sci. Technol.,* vol. 6, no. 2, pp. 316-321, 1969.

[7] M. Audi, L. Dolcino, F. Doni and B. Ferrario, "A new ultrahigh vacuum combination pump," *J. Vac. Sci. Technol. A,* vol. 5, no. 4, pp. 2587-2590, 1987.

[8] J. Römer, "Combined sputter-ion and NEG pump," *Vacuum,* vol. 43, no. 5-7, pp. 551-553, 1992.

[9] P. Manini, A. Conte, L. Viale, A. Bonucci and L. Caruso, "A novel route to compact, high performance pumping in UHV-XHV vacuum systems,"

Vacuum, vol. 94, pp. 26-29, 2013.

[10] C. Benvenuti, J. Bojon, P. Chiggiato and G. Losch, "Ultimate pressures of the Large Electron Positron Collider (LEP) vacuum system," *Vacuum,* vol. 44, no. 5-7, pp. 507-509, 1993.

[11] C. Benvenuti and P. Chiggiato, "Obtention of pressures in the 10-14 torr range by means of a Zr-V-Fe non evaporable getter," *Vacuum,* vol. 44, no. 5-7, pp. 511-513, 1993.

[12] A. Bonucci, A. Conte and P. Manini, "Combined pumping system comprising a getter pump and an ion pump". Patent EP 2409034.

[13] E. Maccallini, P. Manini, A. Conte, F. Siviero and A. Bonucci, "New approach to meet vacuum requirements in UHV/XHV systems by non-evaporable getter technology," *J. Phys.: Conf. Ser.,* vol. 390, no. 012006, 2012.

4. Choice of cathode materials for SIPs

The study and development of innovative cathodes followed the scheme in Figure 4-1: the first step included a full characterisation of a series of traditional diode and noble-diode SIPs, whose functioning principles are explained in Chapter 2. The second part was devoted to the characterisation of pumps with two cathodes made of the same material (other than Ti) or, alternatively, couples of two different cathodes (other than Ta and Ti).
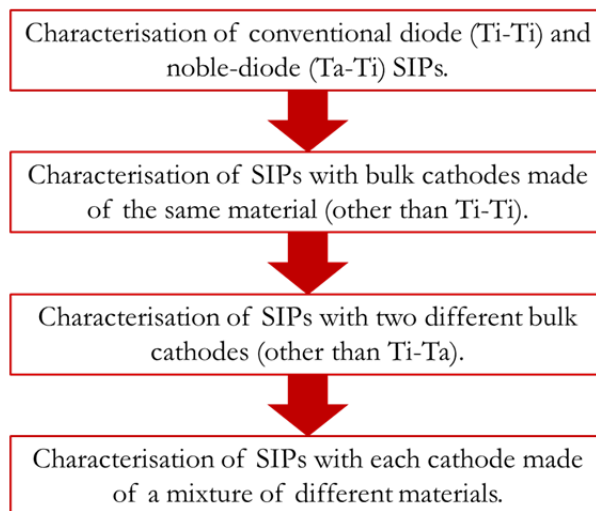
Figure 4-1 – Sequence of the SIP characterisation made in the framework of the thesis project.

Finally, the last stage was the production and study of cathodes made by sintering powders of different materials. More details about the choice of materials and the manufacturing of the cathodes are given in the following sections.

4.1. Examples from the literature

A number of papers has been published in the past decades about the possibility to vary the cathode materials of diode SIPs, in order to improve their pumping efficiency for some gases of interest. The most significant are listed in the following. Since the earliest investigations on SIP technology made by Hall, Ti has been identified as the most suitable cathode material, both due to its chemical reactivity as well as to its availability and price [1]. Other materials were also examined by Hall, including Mg, Fe, Al, Mo, and Cu, but Ti was found to be clearly superior in terms of pumping speed provided for air. Cu was proven to be the scarcest option, while other reactive metals (*viz.*, Zr, Hf, V, and rare earths) gave promising results but were discarded, presumably due to practical or economic reasons.

The most important step forward was made by Jepsen, who described the mechanism of high-energy neutrals and led to the development of noble-diode SIPs [2] [3]. Since then, the most thorough investigation was carried out by Vaumoron and De Biasio, who meticulously tested several couplings of different cathode materials and found that the ratio R between their mean atomic mass and that of the impinging gas ions determines whether a SIP will be prone to instability or not [4]. They found, in particular, that a minimum ratio R~2.5 is necessary for a SIP with flat cathodes in order to completely avoid the onset of instability; if two different cathode materials are paired, the atomic mass of the heaviest one is used to calculate the ratio. The larger is R, moreover, the higher is pressure at which instability occurs: with Ti cathodes and Xe, for instance, instability was observed already in the 10^{-8} Torr range, while with Ne it arose at 10^{-5} Torr.

Baker and Laurenson [5] studied instead the pumping behaviour of some combinations of Al, Ti, and Ta cathodes with He, Ne, Ar, and Kr; their conclusion was that pumping speed S is generically dependent on the same ratio R according to the following relationship, which results in the fact that pumping speed is higher when heavier cathodes pump lighter gases:

$$S \propto log\, R$$

Lamont [6], on the basis of the energetic-neutrals theory, also found that Ar pumping speed of different cathode materials (*viz.*, Ti, Nb, Mo, Ta) is determined by their atomic masses.

The performance of a SIP with a pair of cathodes made of Zr and Al has also been investigated [7]. N_2 and Ar pumping speeds of this new pump at $1 \cdot 10^{-5}$ Pa were found to be, respectively, 1.8 and 3.3 times larger compared to a standard diode SIP; H_2 pumping speed was instead slightly lower. Cathodes made of aluminium mixed rare-earth alloy have also been proposed, which resulted in a 40% higher air pumping speed compared to diode SIPs, due to the ability of this material to form stable compounds like oxides and nitrides with chemically-active gases [8].

Finally, other investigations have been made on a possible SIP coupling a Ti flat cathode with a Mg one [9]; the idea was to use a high vapour-pressure metal and to increase the ionisation rate of the Penning cell—and thus its characteristic pumping speed—simply by heating the new electrode.

Except for Ta-Ti noble-diode SIPs, however, none of these proposed solutions relying on new cathode materials has never been implemented in any commercial product. Improvements in the SIP technology came instead from geometry modifications of the pump and, in particular, of the electrodes: triode SIPs [10] are a significant examples of this, whilst multi-holed cathodes [11] and post-cathode SIPs [6] have been also considered.

4.2. Single metal and couplings of two metals

As already mentioned, after the completion of the initial series of characterisations made on conventional diode and noble-diode SIPs, further sorption tests have been performed with different couplings of bulk cathode plates. A number of chemical and physical parameters was taken into account when selecting the innovative materials to be tested:

– the atomic mass number A, which is involved in the high-energy neutrals theory [12] and, consequently, in the pumping efficiency for noble gases [2] and in the possible outbreak of instability [4];

–   the sputter yield (SY), which determines the erosion of the cathodes and increases along each period of the periodic table as the *d* shell is progressively filled [13];

–   the gettering ability of the material, which is typically a characteristic of metals belonging to the 4th and the 5th group of the periodic table;

–   the crystal structure of the material lattice;

–   the melting point, which might play a role during sputtering and in the resulting surface modifications of the cathodes.

Based on these considerations, the following materials were selected, among the others, for studying their possible exploitation in a new type of SIP:

–   <u>Al</u>: low mass, low cost, highly reactive, intermediate SY;

–   <u>Cu</u>: heavier than Ti, no gettering properties, being a noble metal has one of the highest SY;

–   <u>Zr</u>: SY and gettering similar to Ti but almost double atomic mass;

–   <u>Nb</u>: high atomic mass, same group as V and Ta, low SY, cheaper than Ta;

–   <u>Ta</u>: very high atomic mass but also high cost, low SY, limited getter properties.

Other candidate materials (*viz.*, Mg, V, Y, Ag, Hf, W, Au) were instead left out, mainly due to the cost of the raw materials and their workability, which excluded *a priori* their eventual use as bulk cathode plates on an industrial scale.

Cathodes	Mean atomic mass [u]
Al-Al	26.982
Cu-Cu	63.546
Zr-Zr	91.224
Nb-Nb	92.906
Ta-Ta	180.950
Cu-Ti	55.713
Nb-Cu	78.226
Ta-Zr	136.087

Table 4-1 – Tested combinations of cathode plates. Their mean atomic masses are also indicated.

The adopted configurations, whose sorption properties have been studied and compared to those of conventional diode and noble-diode SIPs, are resumed in Table 4-1. For the sake of simplicity, each SIP configuration was denominated by the symbols of its pair of cathodes: Ta-Ta represents for instance a SIP with both cathodes made of tantalum, whilst Cu-Nb indicates a SIP with a cathode made of copper and the other one of niobium. Diode and noble-diode pumps might be thus indicated in the following also as Ti-Ti and Ta-Ti, respectively.

Prior to the use in UHV conditions, each pair of cathode plates was cleaned in an ultrasonic bath with an appropriate alkaline detergent (M-Aero-NS, Arm & Hammer). Afterwards, they underwent an *in-vacuo* annealing thermal treatment, with the main aim of reducing the degassing rate of H_2. The standard procedure was 600 °C for 3 h, which reduces the initial outgassing of more than two orders of magnitude; this is a reasonable compromise based on previous SAES experience about the vacuum firing of Ti and Zr alloys. Al cathodes were heated to 300 °C and Ta and Nb ones to 800 °C, always for 3 h, taking into account their respective melting points.

4.3. Sintered cathodes

Cathodes made of a mixture of different materials were produced by hot uniaxial pressure (HUP) sintering of powders. This technique consists in the simultaneous application of uniaxial pressure and heat to a mould containing the metal powders to be sintered. Hot pressing allows to greatly reduce porosity and to obtain bulk density; furthermore, it results in better mechanical properties and in a more uniform microstructure compared to conventional press or sintering processes.

The choice of the HUP technique was driven by the need to explore new ways of producing cathodes for SIPs, differently to other solutions proposed in the past (like, for instance, the already-mentioned triode SIPs, post pumps or multi-holed Ta plates combined with flat Ti ones). As a matter of fact, the HUP process allows to make couples of cathodes in which two different metals—such as Ti and Ta—are homogeneously distributed, in contrast with the conventional noble-diode SIP layout, where a pure Ti cathode is opposed to a pure Ta one. If necessary, it also permits to increase the number of elements constituting each

cathode, instead of using only two of them each time. Furthermore, the HUP technique is a good way to produce a mixture of different materials with bulk density without using alloys, which instead would result in new compounds with different physical and chemical properties. Finally, the atomic percentage of each element in the mixture to be sintered can be easily tuned in order to find the highest-performing one, taking into account the constraints determined by the necessary retention of appropriate mechanical properties in the sintered cathodes. The use of bulk cathode plates, each one made of a single pure material—as those described in the previous section—clearly does not allow this kind of tuning of the elemental composition.

Several couples of HUP cathodes have been characterised: Table 4-2 introduces the explored compositions and resumes the atomic percentages of each element for each pair of cathodes. Both cathodes of each couple were identical and had the same elemental composition. Except for a couple of cathodes made of pure Ti, all the others were obtained by sintering powders of two different elements. Each composition is identified by the symbols of its constituents; the subscript numbers indicate the atomic percentage of each element.

Cathode	Mean atomic mass [u]	Element 1 (at%)	Element 2 (at%)
Ti	47.880	Ti (100)	---
$Zr_{50}Ti_{50}$	69.552	Zr (50)	Ti (50)
$Ta_{35}Ti_{65}$	94.455	Ta (35)	Ti (65)
$Ta_{50}Ti_{50}$	114.415	Ta (50)	Ti (50)
$Ta_{35}Zr_{65}$	122.628	Ta (35)	Zr (65)
$Ta_{50}Zr_{50}$	136.087	Ta (50)	Zr (50)

Table 4-2 – Atomic percentage of each element constituting the HUP cathodes under examination.

The choice of the HUP cathodes so far produced and tested was dictated by several factors and involved different combinations of Ti, Zr and Ta. First of all, Ti and TaTi cathodes were specifically conceived in order to have a direct comparison with standard diode and noble-diode SIPs and to easily highlight any possible advantage in the pumping performance of these cathodes given by the HUP processing itself. Secondly, the choice was driven by the best-performing couplings of bulk cathode materials described in the previous section, thus excluding Al and Cu (cf. characterisation results in Chapter 6). Furthermore, the

chosen HUP combinations spread over a wide range of mean atomic masses (from 48 u to 136 u) and thus they could give useful suggestions about the influence of this parameter on the pumping properties of SIPs. At the same time, a significant role was played also by the affordability and availability of the raw materials, as well as by the physicochemical properties of the elements and of their binary mixtures. From this point of view, the study of the phase diagrams drove the exclusion of mixtures that may result in the formation of eutectics or intermetallic compounds (see for instance the Cu-Ti phase diagram in Figure 4-2a).
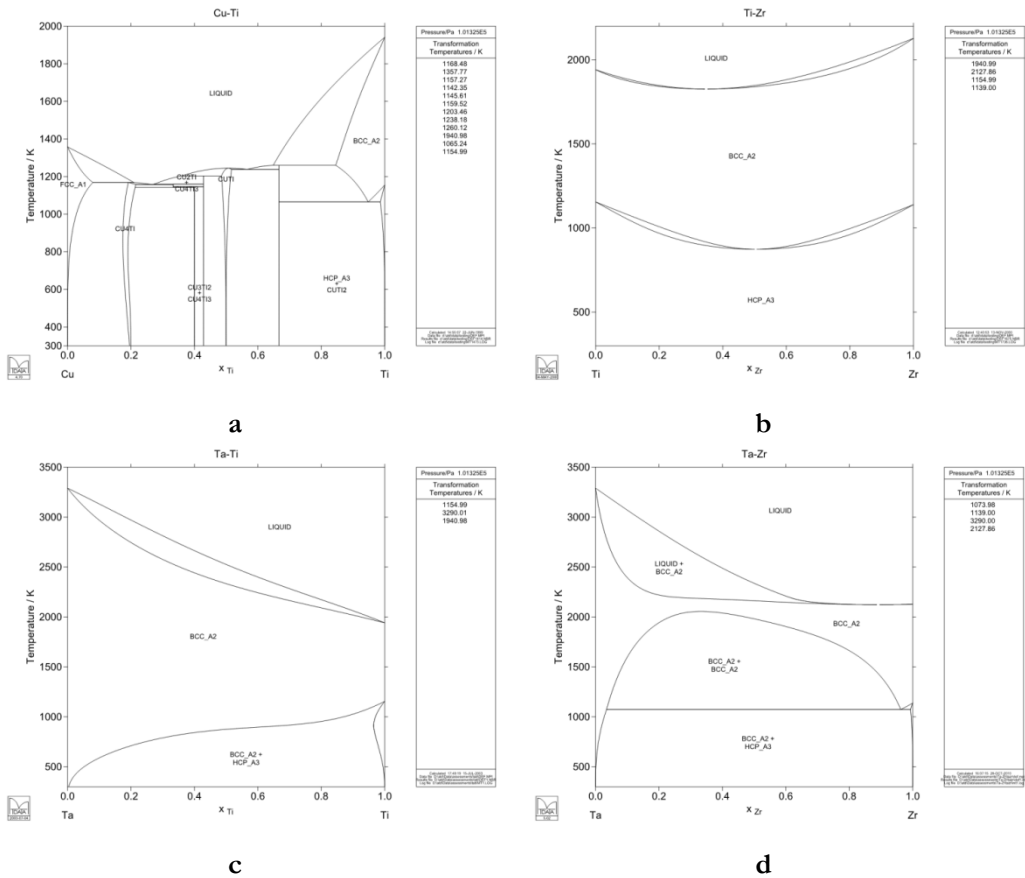
Figure 4-2 – a) Cu-Ti phase diagram. Phase diagrams of the investigated HUP binary combinations: b) ZrTi, c) TaTi, d) TaZr (courtesy of NPL online database).

These latter were excluded from this study for the sake of simplicity, due to the fact that their physicochemical properties (*e.g.*, crystal structure, melting point)

might be different from those of their original constituents, thus adding additional variables in the determination of the performance of each couple of cathodes. For the same reason, mixtures of three or more elements and alloys have been so far excluded but they will possibly be the object of further, future investigations. All these aspects steered the choice of HUP cathodes constituents towards these three elements (Ti, Zr and Ta) to the detriment of other possible combinations; the related phase diagrams are shown in Figure 4-2b-d. Nb has been for now excluded due to the high cost of its powders and to logistic reasons concerning its availability and delivery time by the supplier.

4.3.1. Production and thermal treatment of sintered cathodes

The process parameters of the HUP sintering were determined case by case by the nature of the mixture components. More in detail, the processing temperature generally ranged between several hundreds of Celsius degrees, while the applied uniaxial pressure was of the order of several tens of bar.

Cathodes	Temperature	Time length
Ti	600 °C	3 h
$Zr_{50}Ti_{50}$	1100 °C	40 min
$Ta_{35}Ti_{65}\_1$	1100 °C	40 min
$Ta_{35}Ti_{65}\_2$	800 °C	3 h
$Ta_{50}Ti_{50}\_1$	1100 °C	40 min
$Ta_{50}Ti_{50}\_2$	800 °C	3 h
$Ta_{50}Ti_{50}\_3$	1100 °C	72 h
$Ta_{35}Zr_{65}$	1100 °C	72 h
$Ta_{50}Zr_{50}$	1100 °C	72 h

Table 4-3 – Temperature and time length of the thermal treatment performed on each pair of HUP cathodes.

At the end of the HUP process, each cathode was grinded, if necessary, and carefully cleaned in an ultrasonic bath with the same above-mentioned detergent. Afterwards, each pair of cathodes underwent an *in-vacuo* annealing thermal

treatment, with the main aim of reducing the degassing rate of H_2. Different combinations of temperature and time length of annealing have been tested, in order to assess the modifications induced in the cathode morphology and microstructure by the thermal treatment, as well as their possible repercussions on the pumping performance (more details are given in Chapters 6 and 7). For this reason, more than one couple of both $Ta_{35}Ti_{65}$ and $Ta_{50}Ti_{50}$ cathodes has been produced and characterised.

Table 4-3 resumes all the tested configurations and the corresponding thermal treatments. The 72 h treatment, in particular, was introduced in order to verify the effects of a high-temperature long annealing on the homogeneity of the cathode microstructure.

References

[1] L. D. Hall, "Electronic Ultra-High Vacuum Pump," *Rev. Sci. Instr.,* vol. 29, no. 5, pp. 367-370, 1958.

[2] R. L. Jepsen, "The physics of sputter-ion pumps," in *Proc. 4th Int. Vacuum Congr.*, London, 1968.

[3] I. Brodie, L. T. Lamont and R. L. Jepsen, "Production of high-energy neutral atoms by scattering of ions at solid surfaces and its relation to sputtering," *Phys. Rev. Lett.,* vol. 21, no. 17, pp. 1224-1226, 1968.

[4] J. A. Vaumoron and M. P. De Biasio, "Argon and rare gas instability with heavy metal cathode Penning Pumps," *Vacuum,* vol. 20, no. 3, pp. 109-111, 1970.

[5] P. Baker and L. Laurenson, "Pumping mechanisms for the inert gases in diode Penning pumps," *J. Vac. Sci. Technol.,* vol. 9, no. 1, pp. 375-379, 1972.

[6] L. Lamont, "A novel diode sputter-ion pump," *J. Vac. Sci. Technol.,* vol. 6, no. 1, pp. 47-51, 1969.

[7] T. Okano, A. Ohsaki and Y. Tuzi, "A Zr-Al composite-cathode sputter-ion pump," *J. Vac. Sci. Technol. A ,* vol. 2, no. 2, pp. 191-194, 1984.

[8] M. Lu and P. Fang, "New cathode material for sputter ion pumps: aluminum mixed rare-earth alloy," *J. Vac. Sci. Technol. A,* vol. 5, no. 4, pp. 2591-2593, 1987.

[9] T. Tom, "Use of a Metallic Ion Source in Cold Cathode Sputter Ion Pumps," *J. Vac. Sci. Technol.,* vol. 9, no. 1, pp. 383-386, 1972.

[10] M. Pierini and L. Dolcino, "A new sputter ion-pump element," *J. Vac. Sci. Technol. A,* vol. 1, no. 2, pp. 140-142, 1983.

[11] S. Komiya and N. Yagi, "Enhancement of noble gas pumping for a sputter-ion pump," *J. Vac. Sci. Technol.,* vol. 6, no. 1, pp. 54-57, 1969.

[12] C. Snoek and J. Kistemaker, "Fast ion scattering against metal surfaces," *Advances in electronics and electron physics,* vol. 21, pp. 67-99, 1966.

[13] N. Laegreid and G. K. Wehner, "Sputtering yields of metals for Ar+ and Ne+ ions with energies from 50 to 600 eV," *J. Appl. Phys.,* vol. 32, no. 3, pp. 365-369, 1961.

5. Experimental setup and procedure

5.1. Choice of the testing procedure

The choice of a suitable testing procedure for SIPs in view of the combination with NEGs was not trivial but rather represented the main initial step of this experimental campaign. This topic is also the scope of a paper recently appeared on *Vacuum*[1].

As already mentioned, pumping mechanisms of SIPs involve several competing chemical and physical effects and are different for different gases. At any given time, the overall pumping speed of a SIP is thus dictated by the balance between ions adsorbed at the electrodes and desorbed from them. Pumping speed of a SIP, in particular, is not constant but varies over its working-pressure range: it usually increases from base pressure until about 10^{-6} Torr and then it starts to decrease again, mainly due to power dissipation and pump overheating, which stimulate desorption from the pump's elements [1].

The measurement of SIP performance, in terms of ultimate pressure and pumping speed, is regulated by an international standard issued by ISO/DIS [2]. According to it, N_2 should be used as test gas and pumping speed should be determined with the known-conductance method [3] for pressures ranging between the lowest possible value (at least 10^{-8} Torr) and 10^{-5} Torr; pressure should be progressively increased in steps and it is necessary to wait each time until equilibrium conditions are established. The evolution of pumping speed after saturation shall be plotted as a function of pressure; the maximum value shall be

_____

[1] T. Porcelli, F. Siviero, G. Bongiorno, P. Michelato, C. Pagani, "Characterisation of sputter-ion pumps to be used in combination with non-evaporable getters", *Vacuum* **123** (2016) 23-28.

quoted as the nominal pumping speed of the SIP, specifying its corresponding pressure.

On the other side, NEG pumps are commonly tested according to the former ASTM F798-97 standard practice [4], which was specifically conceived for them. When combining SIP and NEG pumps, an in-depth characterisation of both components is necessary in order to optimise the coupling and its synergies. All phenomena which might cause desorption from a SIP—like Ar instability, CH_4 cracking and gas regurgitation—need to be carefully evaluated in view of the coupling with NEG. Thus it follows that the testing procedures of SIPs and NEGs should somehow line up.

In this perspective, a new approach based on the ASTM F798-97 practice was adopted for the characterisation of SIPs, beyond the conventional ISO/DIS standard. In compliance with this guideline, pumping speed of a SIP for a specific gas should be measured at constant pressure (again using the known-conductance method) and plotted as a function of the sorbed quantity of gas (expressed in Torr·l or Pa·l). Each test should last until the complete saturation of the SIP and the attainment of a constant equilibrium pumping speed. Although NEG pumps are normally tested at pressure equal to $3 \cdot 10^{-6}$ Torr or $3 \cdot 10^{-7}$ Torr, different conditions have been progressively introduced in the characterisation of SIPs; further details are given in the following sections. Furthermore, the use of a quadrupole mass spectrometer (QMS) to follow the evolution of partial pressures during each test is of basic importance, in order to quantify the desorption from the SIP of each gas species and to distinguish the reactive gases from the non-getterable ones.

5.2. Test-bench layout

A schematic layout of the experimental test-bench (Figure 5-1) used for the characterisation of SIPs is depicted in Figure 5-2. The system is made of a main vacuum vessel, with a volume of 26.7 l, where a Pfeiffer Prisma Plus quadrupole mass spectrometer (QMS) for residual gas analyses and the SIP under test are installed.

Gas leaks into the main volume through a known conductance C, whose choice and optimisation will be discussed in the following (Section 5.5.1); the

conductance value can be estimated through geometry calculations for a short duct and confirmed by experimental pump-down measurements. The entire system is pumped by an Edwards XDS 10 scroll pump (PS) connected in series to a Pfeiffer Vacuum HiPace 300 turbomolecular pump (TMP), which provides a nominal pumping speed of 260 l/s for N_2. Gas leakage into the system is controlled by automatic valves built in-house.
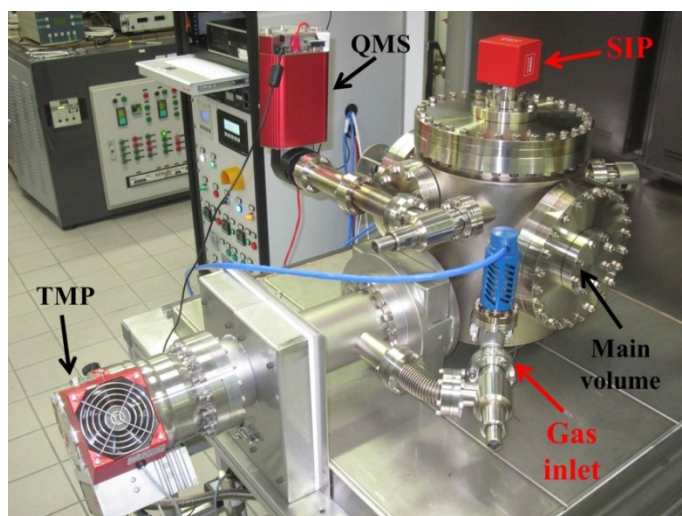
Figure 5-1 – Test-bench at SAES Vacuum Systems Development Laboratory in Lainate, Italy.
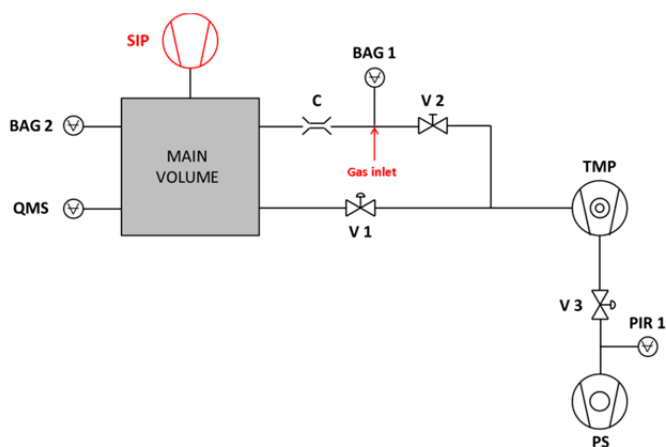
Figure 5-2 – Layout of the adopted experimental test-bench.

As already mentioned, the adopted testing procedure is based on the known-conductance method [3] [5]. Two hot-cathode Bayard-Alpert gauges (Granville-Phillips 360/370 Stabil-Ion®), BAG1 and BAG2, are placed in proximity of the gas inlet and in the main volume near SIP and QMS, respectively. Their working pressure range is 10^{-2} Torr to 10^{-10} Torr. According to a codification traditionally adopted at SAES laboratories, P_{BAG1} and P_{BAG2} in the following will always be indicated as P_m and P_g, respectively.

5.3. Experimental procedure

The layout described in Section 5.2 allows performing sorption tests of pumps keeping constant either P_g (as prescribed by ASTM F798-97 [4]) or P_m (*i.e.*, setting a constant gas flow entering the main vessel).

According to this configuration, the main volume is isolated from the TMP by closing valve V1 and the quantity of gas Q pumped by the SIP (in Torr·l) is thus defined by:

$$Q = C \int \left(P_m - P_g \right) dt$$

The corresponding pumping speed S (in l/s) is consequently given by:

$$S = C \left(\frac{P_m}{P_g} - 1 \right)$$

Furthermore, by substituting in this last equation P_g with the partial pressure of the test gas measured by QMS, it is possible to calculate the effective pumping speed S_{QMS} of the SIP for this specific gas, leaving aside the influence of the others.

The results of each test are usually plotted in terms of pumping speed S or, alternatively, S_{QMS} (in l/s) on the y-axis as a function of the pumped quantity of gas Q (in Torr·l) on the x-axis.

BA gauges and QMS are periodically calibrated against a certified gauge (BAG N_2 sensitivity: 0.37 A/Pa, QMS sensitivity: $1.35 \cdot 10^{-4}$ A/Pa for N_2). After every venting necessary for the installation of a new SIP to be characterised and prior to make whichever sorption test, the entire vacuum system is baked by means of an *ad hoc* oven. The injection line and the SIP to be tested, without

magnets, are also baked. The adopted procedure includes a 10 h long bake-out at 180 °C, which is sufficient to reach base pressures typically in the 10^{-10}–10^{-9} Torr range; heating at higher temperatures is not feasible due to technical constraints dictated by the QMS filament.

5.4. Layout of the pumps under test

Most part of the sorption tests described in the following chapters concerned SIPs providing a nominal N_2 pumping speed of 5 l/s, which are currently employed in the smaller models of NEXTorr® pumps. For simplicity, these SIPs are referred to hereinafter as IP-5; this category comprises both diode and noble-diode pumps, whose N_2 nominal pumping speed are more or less equivalent. A number of these IP-5 has been characterised in order to clearly assess their pumping performance and to optimise the new testing procedure adopted in view of the coupling with NEG pumps.

| a | b |
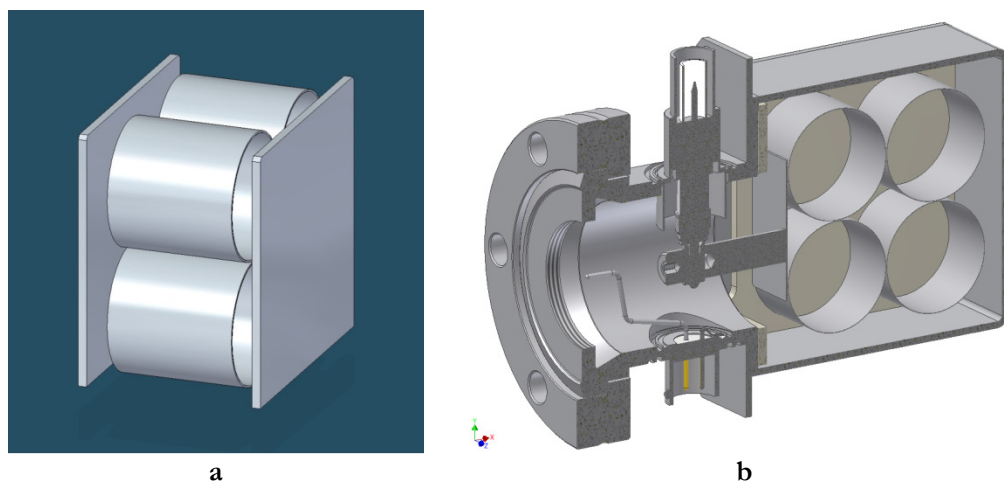
Figure 5-3 – a) electrodes configuration of IP-5 pumps; b) IP-5 layout.

A schematic layout of the electrodes of an IP-5 pump is shown in Figure 5-3a. It comprises an array of four identical cylindrical anodes made of stainless steel located between two cathode plates (Ti-Ti in the case of diode SIPs and Ta-Ti for noble-diode ones). These SIPs are quite small: the dimensions of the

stainless-steel vacuum envelope enclosing the electrodes are 60x62x42 mm; a section of an IP-5 cut along its symmetry plane is shown in Figure 5-3b. Pumps are connected to the vacuum system through a CF35 flange and magnets are placed outside the vacuum envelope, in correspondence of the cathodes.

In the present configuration, the vacuum envelope of an IP-5 is sealed, so that it is not possible to remove the electrodes without breaking the pump itself. A laboratory pump (IP-LAB) has been therefore conceived for testing the various pairs of innovative cathodes other than Ti-Ti and Ta-Ti; it is geometrically identical to conventional IP-5 pumps, except for a CF63 flange welded on the back, which allows an easy replacement of the electrodes and a repeated use of the same pump (Figure 5-4). The front part is not modified, so that direct comparisons with IP-5 pumps are still feasible.
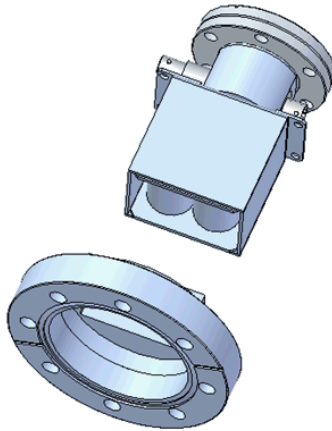
Figure 5-4 – IP-LAB layout.

5.5. **Optimisation of the testing procedure**

Once the experimental setup and procedure were established and the sorption tests started, some further adjustments became necessary in order to fine-tune the experiments and to optimise the results achievable with this kind of measurements. These improvements primarily concerned the choice of an

appropriate conductance for testing SIPs of this size and the adoption of tests at constant P_m instead of P_g for certain gases; more details are given in the following.

5.5.1. Conductance choice

The conductance of the test-bench is determined by a hole in a blind 1 cm long OFC copper CF35 flange. The nominal dimensions of the initially-chosen conductance C_1 are reported in Table 5-1, together with its corresponding nominal value C_{TH} for N_2 at 20 °C, calculated according to the following formula for the conductance of short pipes (*i.e.*, with $L<20 \cdot D$) derived by Clausing [6] [7], where L is the hole length and D is its diameter:

$$C = 12.1 \cdot \alpha \cdot \frac{D^3}{L} \cdot \sqrt{\frac{29}{28}} = 12.1 \cdot \frac{15\frac{L}{D} + 12\left(\frac{L}{D}\right)^2}{20 + 38\frac{L}{D} + 12\left(\frac{L}{D}\right)^2} \cdot \frac{D^3}{L} \cdot \sqrt{\frac{29}{28}}$$

In addition, the conductance was also experimentally measured through the evacuation method; the resulting value C_{EXP} is also reported in Table 5-1. The difference between the theoretical and experimental values of C_1 (1.33 l/s *vs.* 0.95 l/s) was probably ascribable to the intrinsic inaccuracy of the evacuation method for a conductance of such dimensions installed on a system with a relatively small volume (26.7 l).

	L [cm]	D [cm]	C_{TH} [l/s]	C_{EXP} [l/s]
C_1	1	0.6	1.33	0.95
C_2	1	0.15	0.032	0.030

Table 5-1 – Length L and diameter D of the first and the second installed conductances C_1 and C_2, together with their respective calculated values C_{TH} and experimental values C_{EXP} for N_2 at 20 °C.

The corresponding values of C_1 for several other gases of interest are reported in Table 5-2. This conductance had been previously conceived in order to make sorption tests with pumps pumping up to 5000 l/s, considering the working range of Bayard-Alpert gauges. However, the first tests performed on the test-bench showed that a conductance of this size was not suitable for the

characterisation of small SIPs providing very limited pumping speeds. The worst scenario, in particular, was represented by diode 5 l/s SIPs pumping Ar and Ne, whose pumping speeds after saturation are of the order of 0.3 l/s, *i.e.* much smaller than the conductance itself.

	H_2	He	CH_4	Ne	N_2	CO	O_2	Ar	CO_2	Kr
C_1	3.55	2.51	1.26	1.12	0.95	0.95	0.89	0.79	0.76	0.55
C_2	0.112	0.079	0.040	0.035	0.030	0.030	0.028	0.025	0.024	0.017

Table 5-2 – Values of the first conductance for different gases.
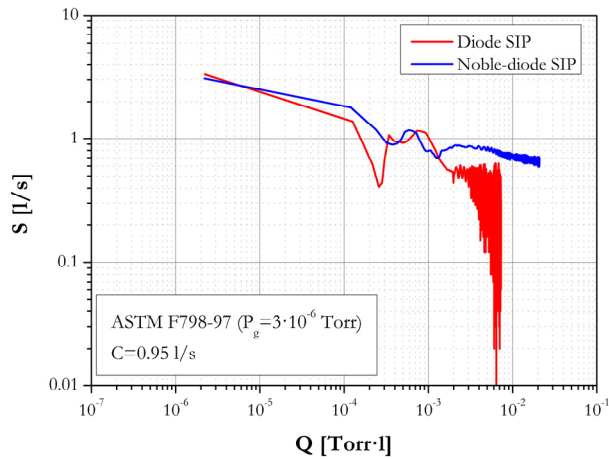
Figure 5-5 – ASTM F798-97 Ar sorption curves at $P_g=3\cdot10^{-6}$ Torr of a diode and a noble-diode 5 l/s SIP, with C=0.95 l/s (nominal N_2 value).

Figure 5-5 shows two ASTM F798-97 sorption curves for Ar at $P_g=3\cdot10^{-6}$ Torr, obtained respectively with a diode and a noble-diode 5 l/s SIP. The strong fluctuations observed with the diode pump were caused by the inability of the automatic gas leakage valve to properly regulate its aperture in order to maintain the correct P_g value in the presence of a so small pumping speed. These oscillations usually started to arise after the very initial transient and the sorption of few 10^{-2} Torr·l of gas. Fluctuations in the curve of the noble-diode SIP were less intense, thanks to its higher Ar pumping speed, but still easily noticeable. At $P_g=3\cdot10^{-7}$ Torr this phenomenon was even more pronounced and appeared at

even lower values of Q (before $1 \cdot 10^{-3}$ Torr·l), few minutes after the beginning of each test, with both diode and noble-diode SIPs.

The occurrence of this phenomenon made it impossible to perform this kind of tests with the described experimental setup. A new smaller conductance was therefore adopted, in order to face the onset of such fluctuations and to possibly mitigate them. The dimensions of this new conductance C_2 are reported in Table 5-1, together with its calculated and measured values, C_{TH} and C_{EXP} (0.03 l/s for N_2). Its corresponding values for other gases can be found in Table 5-2.
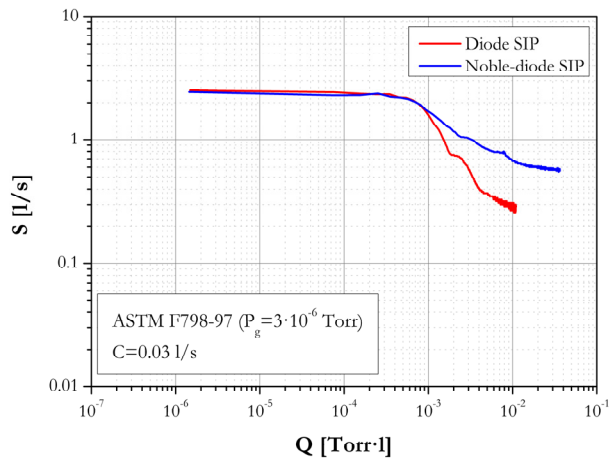
Figure 5-6 – ASTM F798-97 Ar sorption curves at $P_g=3 \cdot 10^{-6}$ Torr of a diode and a noble-diode 5 l/s SIP, with C=0.03 l/s (nominal N_2 value).

The introduction of a more proper conductance, this time considerably smaller than Ar pumping speed of 5 l/s diode SIPs, greatly reduced the amplitude of the fluctuations while testing these pumps at $P_g=3 \cdot 10^{-6}$ Torr (cf. Figure 5-6). However, as fluctuations completely disappeared with noble-diode pumps, the conductance change did not affect instead the performance of diode SIPs at $P_g=3 \cdot 10^{-7}$ Torr, where strong oscillations still occurred. It is worth mentioning that the change of conductance had no influence on the measured pumping speed values, net of fluctuations. The better results obtained for both conductances, in terms of amplitude of the fluctuations, with noble-diode SIP are presumably influenced by the higher performances of this kind of pumps in the sorption of

Ar. The higher provided pumping speed, as well as the reduced gas desorption caused by the onset of instabilities, are the most probable reasons for the minor extent of their oscillations compared to diode pumps.

Further improvements in the experimental setup and procedure, which together with the conductance change paved the way to a correct evaluation of the pumping performance for noble gases and CH_4, are discussed in the next section.

5.5.2.   Experimental procedure optimisation

The initial testing sequence adopted for the characterisation of SIPs on the test-bench consisted of a series of ASTM F798-97 sorptions, made alternatively at $P_g=3 \cdot 10^{-7}$ Torr or $P_g=3 \cdot 10^{-6}$ Torr. However, it soon became clear that this procedure could not ensure the best results in terms of accuracy and reproducibility of the curves, especially for certain gases.
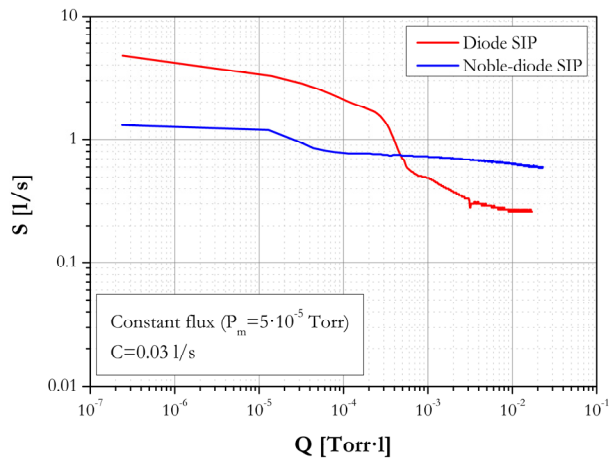
Figure 5-7 – Ar sorption curves at $P_m=5 \cdot 10^{-5}$ Torr of a diode and a noble-diode 5 l/s SIP, with C=0.03 l/s (nominal N_2 value).

ASTM F798-97 sorption tests, in particular, do not fit for CH_4. As a matter of fact, cracking of hydrocarbons leads to the regurgitation of gaseous H_2 from the electrodes during sputtering and, if CH_4 pumping speed is measured simply

keeping a constant value of P_g inside the vacuum chamber pumped by the SIP, the regurgitation of H_2 from this latter will progressively alter the residual gas composition in the vacuum system, thus resulting in distorted information about the real CH_4 pumping speed. For this reason, CH_4 tests should be carried out keeping a constant incoming flux of gas (*i.e.*, at constant P_m).

Along with this change, the way to test noble gases (and, in particular, Ar) was also modified. As already mentioned, measuring rather small pumping speeds may result in strong fluctuations of the sorption curves if the conductance is not adequate, due to the inability of the automatic valves to properly adjust their aperture at the set pressure. This initial problem was partially solved by adopting a new conductance sufficiently smaller than the pumping speed to be measured.

However, a further enhancement was obtained by choosing tests at constant P_m also for Ar, Ne and Kr, in place of standard ASTM F798-97 at constant P_g. In both cases (CH_4 and noble gases) $P_m = 5 \cdot 10^{-5}$ Torr was chosen as set pressure for the tests; after saturation of a diode SIP, this value results in P_g of the order of $5 \cdot 10^{-6}$ Torr when pumping Ar or Ne. Figure 5-7 shows that, by doing so, fluctuations completely disappeared also with diode SIPs; again, as for the conductance change, this further modification of the experimental setup did not affect the shape of the sorption curves after saturation and the measured equilibrium pumping speeds. The onset of fluctuations did not pertain to ASTM F798-97 sorptions of He at $P_g = 3 \cdot 10^{-6}$ Torr, which therefore remained unvaried.

5.6. Study of Ar and CH_4 pumping by SIPs

Some practical examples about the information achievable with the adopted experimental setup and procedure are given in the following. The focus of the chosen examples is on Ar and CH_4, as their sorption is particularly relevant in view of the SIP+NEG combination pump. When pumping these two gas species, the release of previously-pumped gas should be carefully investigated; the use of a QMS becomes therefore essential and cannot be avoided. A characterisation based uniquely on the standard ISO/DIS SIP testing procedure, when dealing with such regurgitation phenomena, would not discern the effects of the desorbed species and thus it would not give a correct evaluation of the gas loads on the NEG pump and of the actual SIP pumping speed for the gas of interest.

5.6.1. **Regurgitation during Ar pumping**

As cathodes play an important role in the sorption of several gas species, sputtering and erosion produced by the incoming ions may result in the re-emission of previously-pumped gas [8], giving rise to regurgitation phenomena which might heavily influence the sorption efficiency of a SIP. Pumping Ar for a certain time—the so-called *Ar cleaning*—for instance, is a technique commonly adopted to enhance regurgitation and to dramatically increase the pumping speed of reactive gases immediately after the treatment, thanks to the large dose of freshly-sputtered getter material produced by Ar sputtering [1]. Generally speaking, every perturbation in the system's conditions generates a transient variation of pumping performances, which are afterwards gradually restored. In the case of Ar cleaning, for instance, the beneficial effect tends to vanish as the newly-sputtered material progressively saturates.
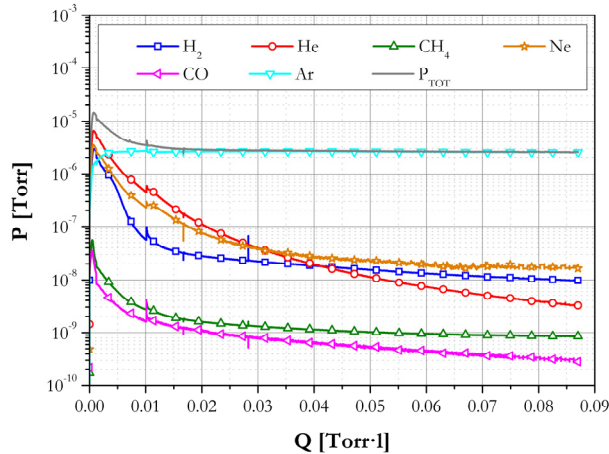
Figure 5-8 – Total pressure and partial pressures of H$_2$, He, Ne and Ar measured by QMS during Ar cleaning due to regurgitation.

Saturation of a SIP occurs when every transient ends and equilibrium between degassing and sorption is reached, *i.e.* when pumping speed does not vary anymore with time, in the absence of further perturbations. The time needed to reach saturation depends of course on several parameters and, in particular, on

working pressure: the lower it is, the longer will be the transient. Gas release from the SIP during such transients is worth being considered in view of the coupling with NEGs. In particular, distinguishing each gas from the other (especially when dealing with mixtures of getterable and non-getterable gases) is important to correctly evaluate the performances of the SIP and thus of the coupling.

Figure 5-8 shows the evolution of partial pressures measured during an Ar sorption test on a 5 l/s diode SIP. The pump was not new but it had been purposely polluted with other gases (*viz.*, He, and Ne), in order to observe how the subsequent pumping of Ar could induce the release of other previously-sorbed species. The subsequent pumping of Ar caused therefore a strong release of previously-sorbed gases, especially in the first hour of test. Afterwards, partial pressures of these gases progressively decreased due to a more stable implantation in the cathodes or in other parts of the SIP, which are not subject to sputtering.

As the test was performed at constant flux, by setting a constant pressure $P_m = 5 \cdot 10^{-5}$ Torr at the gas inlet, the overall pressure P_g inside the vacuum chamber was able to vary all along, until partial pressures of other residual gases became negligible compared to Ar.
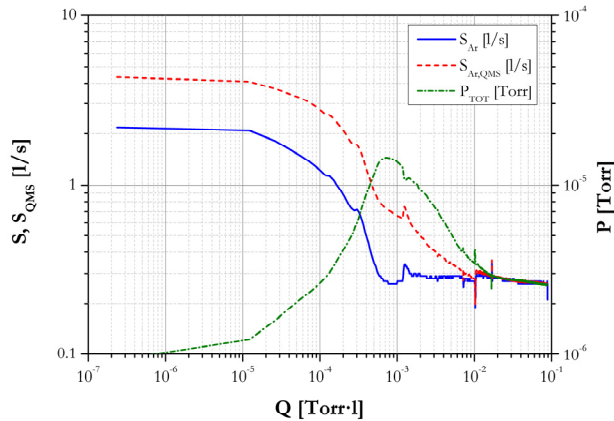
Figure 5-9 – S and S_{QMS} measured during the sorption of Ar (in Figure 5-8) as a function of the gas sorbed quantity; the corresponding total pressure P_{TOT} inside the vacuum vessel is also reported.

Figure 5-9 shows the evolution of pumping speed S measured during the test of Figure 5-8, as well as of the corresponding real Ar pumping speed S_{QMS}, derived from the Ar partial pressures measured by the QMS. These two quantities diverged significantly during the initial part of the test, corresponding to the strong release of previously-sorbed gases. Indeed regurgitated species, on one hand caused an increase of pressure inside the vacuum chamber, while on the other they affected the reading of the gauge, which has a different sensitivity for these gases. Afterwards, as Ar became dominant and the other gas species negligible, pressure became constant and no more difference was noticeable between S and S_{QMS}. However, nearly three hours were necessary for the S value to reflect the real pumping speed for Ar, and a much longer time would have been necessary at lower pressure, like in typical UHV applications.

In order to correctly outline the pump performance throughout the test, it is clear that S_{QMS} should be considered. The use of the QMS for pumping speed calculation gives an insight into the behaviour of a combination pump during similar transient phenomena. For instance, as H_2 was among the gases released by the SIP, in presence of a getter the test result would have been different; in cases where the desorbed species are mainly active gases, in particular, the measured value of S is expected to be much closer to the real Ar pumping speed from the very beginning of test.

As a further example, curves depicted in Figure 5-10 are well-representative of how the same pump can display very different behaviours depending on its pumping history. Figure 5-10a illustrates Ar pumping speeds S of the same 5 l/s noble-diode SIP during two different Ar sorption tests: Ar_1 was performed when the pump was new, right after the bake-out and the first ignition of the pump, while Ar_2 was taken at the end of a series of pumping tests with different gases and, in particular, after a long sorption of He (about 0.1 Torr·l of sorbed He). The first test lasted about 24 hours and the second one about 22 hours. The first test was characterized by a significant release (confirmed by QMS data) of gases adsorbed on cathode surface at atmospheric pressure prior to the installation of the pump in the vacuum system.

During the second test, instead, a very large release of He was recorded, while a minor role was played by other gases, since the pump had already been cleaned by sputtering during the previous test. The pressure increase due to He regurgitation resulted in a substantial lowering of the initial overall pumping speed compared to the previous Ar sorption test. Nevertheless, as He partial pressure

and desorption rate became negligible, a saturation pumping speed equal to that of Ar_1 was measured.
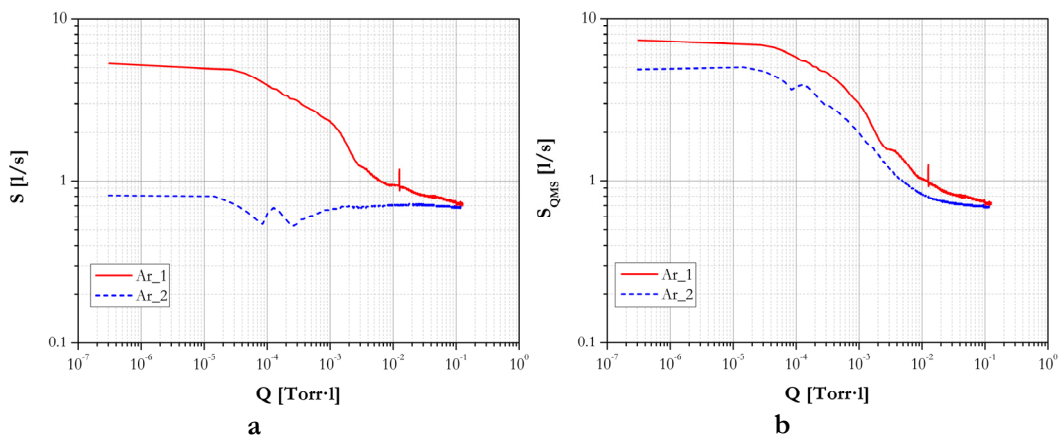
Figure 5-10 – a) Pumping speeds S measured during two different Ar tests as a function of the sorbed quantity of gas; b) corresponding Ar effective pumping speeds S_{QMS} during the same tests.

Figure 5-10b shows the corresponding real Ar pumping speeds S_{QMS}, calculated from QMS data. In this case, the initial values of Ar_1 and Ar_2 were much more similar and of the same order of magnitude, as it is logical to expect since the pump is the same. The slight gap observed was probably due to the unavoidable differences between a brand-new SIP and the same already used. The following trends of both curves are very similar and describe the progressive evolution of Ar pumping speed until the attainment of saturation, regardless of the influence of other desorbing species. S_{QMS} of both tests reached again the same saturation value, thus confirming the soundness of this kind of characterisation.

5.6.2. CH$_4$ pumping

Pumping of hydrocarbons by SIPs occurs through cracking of molecules, which leads to the production of carbonaceous deposits on the cathodes and to the regurgitation of gaseous H_2 from the electrodes during sputtering [9] [10]; for this reason, when CH_4 is pumped by a SIP, the residual gas composition can drastically change during time [11]. If CH_4 pumping speed is measured simply

keeping a constant pressure P_g in the vacuum chamber pumped by the SIP, the regurgitation of H_2 from this latter will progressively alter the residual gas composition in the vacuum system and saturation will never be reached: H_2 pressure will steadily increase and CH_4 flow will be consequently decreased in order to maintain a constant pressure inside the main vessel, thus resulting in distorted information about the real CH_4 pumping speed and capacity of the pump under test. For this reason, tests should be carried out at constant flux and a QMS is in any case necessary to fully understand the occurring phenomena.

CH$_4$ pumping was therefore tested for three small SIPs (*viz.*, α, β, γ), each one having the same geometry but enclosing cathodes made of a different material. A constant pressure $P_m=5\cdot10^{-5}$ Torr was set at the gas inlet. The pumps were new and only an Ar cleaning had been previously made on each of them.

Figure 5-11 shows the evolution of pumping speed S during each test, evidencing the peculiar behaviour of each SIP: pumping speeds S_β and S_γ, in particular, markedly decreased with respect to their initial values, whereas S_α remained more or less constant.
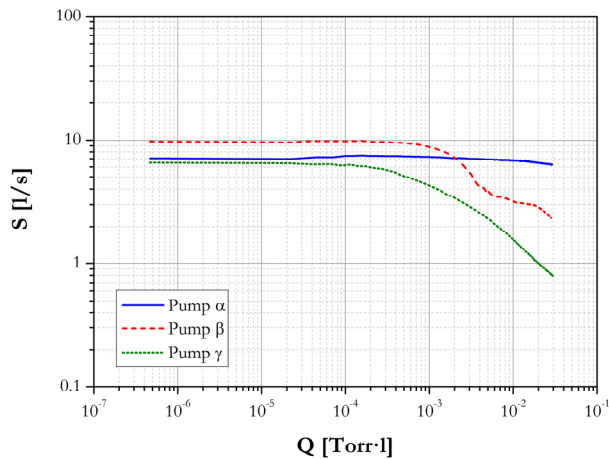
Figure 5-11 – Pumping speeds S of three different pumps measured during CH$_4$ sorption tests as a function of the gas sorbed quantity.

The evolution of H_2 and CH_4 partial pressures measured by QMS during each test is depicted in Figure 5-12 as a function of the sorbed quantity of gas:

CH_4 pressures of pumps α and β were always equivalent and remained constant, according to the fact that these tests were performed under a steady incoming flux of gas. The discrepancy between the overall pumping speeds of α and β is instead explained by the evolution of H_2 pressure, which is a direct consequence of cracking and of H_2 pumping capability of each SIP. With both pumps, H_2 soon became the main residual gas in the system. With pump α, however, the increase in H_2 pressure during time was relatively gradual and, at the end of the test, H_2 pressure was 2.8 times larger than CH_4 one.
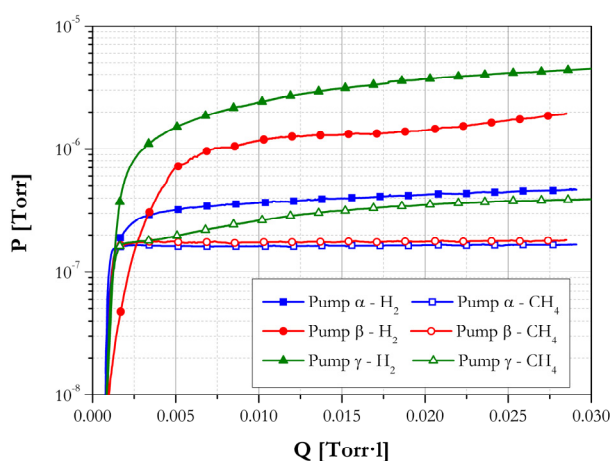
Figure 5-12 – CH_4 and H_2 partial pressure measured by QMS during CH_4 sorption tests of three different SIPs, plotted against the sorbed quantities of gas.

The increase in H_2 pressure of pump β, instead, was much more evident and, at the end, H_2 pressure was more than 10 times larger than CH_4 one. With pump γ, finally, the increase in H_2 pressure was even more pronounced and, in addition, also CH_4 pressure grew.

A more or less pronounced regurgitation of H_2, which is a direct consequence of the capability of a SIP to crack H_2 molecules and to permanently absorb this gas, has thus severe repercussions on the measured overall pumping speed S.

Further confirmation of this can be obtained if, starting from the partial pressures measured by QMS, the real CH_4 pumping speeds S_{QMS} are calculated (cf. Figure 5-13). Unlike the previous case, S_{QMS} of both α and β remained constant,

reflecting the corresponding behaviour of CH_4 partial pressures, whereas only γ showed a sharp drop. This method allows distinguishing between the effects of H_2 and CH_4 on the overall pumping speed. The worse behaviour of β compared to α, observed in Figure 5-11, was therefore exclusively ascribable to a scarcer H_2 pumping capability of the first device; α and β are equivalent if CH_4 only is taken into account. Pump γ, instead, was characterised by scarcer pumping performance for both H_2 and CH_4.
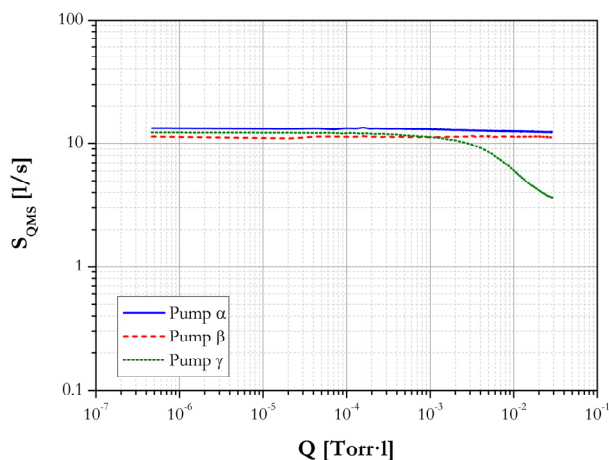
Figure 5-13 – CH₄ effective pumping speeds S_QMS, of three different pumps measured during CH₄ sorption tests as a function of the gas sorbed quantity.

In order to verify that these observations are still valid when combining SIP and NEG pumps, further tests about CH_4 pumping have been conducted, this time coupling a SIP with an activated NEG cartridge able to provide a pumping speed of 100 l/s for H_2. H_2 pumping speed on the SIP only is instead about 6 l/s. Figure 5-14 shows the evolution of CH_4 and H_2 partial pressures during two different tests, with the sole SIP installed in the vacuum system or with the coupling SIP+NEG, respectively. CH_4 partial pressures were equivalent, due to the fact that pumping speed of NEG pumps for hydrocarbons is almost negligible and thus the only pumping was provided by the SIP, which was the same in both cases.
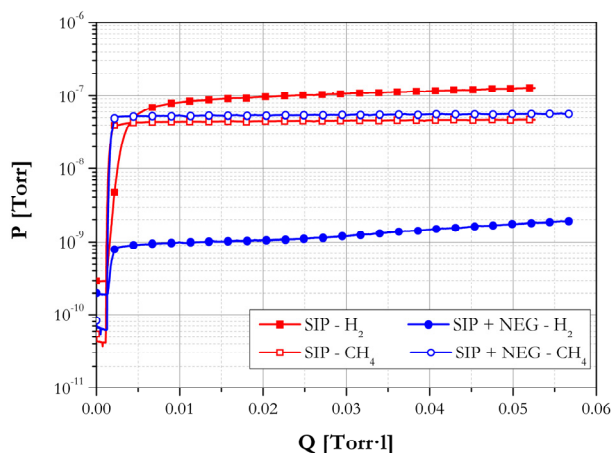
Figure 5-14 – CH$_4$ and H$_2$ partial pressures measured by QMS during two different CH$_4$ sorption tests: with the sole SIP pumping (red lines with squares) and with the same SIP plus a NEG cartridge (blue lines with circles).

As for pumps in Figure 5-12, H$_2$ partial pressures soon became higher than CH$_4$ one with the SIP alone; in the presence of NEG, instead, it remained well-below CH$_4$ partial pressure, thanks to the much higher H$_2$ pumping speed provided by the NEG cartridge in comparison to H$_2$.

This difference can be easily appreciated by comparing the corresponding sorption curves. The overall pumping speed S (which is not corrected with QMS data and which takes into account all the gases) of the sole SIP progressively decreased due to the increasing amount of reemitted H$_2$, whereas S of the coupling SIP+NEG was initially higher and remained constant during the test (cf. Figure 5-15a), due to the fact that the NEG cartridge was easily removing H$_2$. As pumping speed S$_{QMS}$ of CH$_4$ only (calculated via QMS partial pressure data) is taken into account, instead, the two curves become equivalent (cf. Figure 5-15b).

When dealing with Ar, as seen in the previous subsection, S and S$_{QMS}$ of a SIP only differ during the transients and become equivalent when the pump reaches saturation (cf. Figure 5-9). On the other hand, these examples about CH$_4$ demonstrate that, when pumping this gas, S is always different from S$_{QMS}$ (regardless of the pump being saturated or not) due to the completely diverse pumping mechanisms for CH$_4$ and H$_2$.
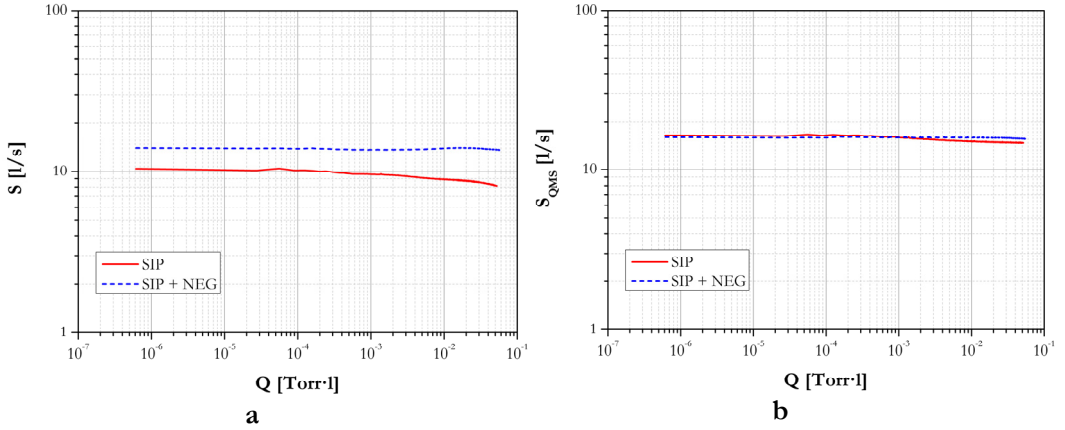
Figure 5-15 – a) Pumping speeds S measured during CH$_4$ sorption tests as a function of the gas sorbed quantity; b) corresponding CH$_4$ effective pumping speeds S$_{QMS}$ during the same tests.

For vacuum systems pumped only by a SIP, these considerations might not be particularly relevant: only the overall pumping speed should be considered in order to discern which pump would be the best for a certain application.

In the perspective of a SIP+NEG combination pump, instead, the opportunity to distinguish between H$_2$ and CH$_4$ is a fundamental requisite. As a matter of fact, a NEG cartridge provides very high pumping speed and capacity for H$_2$ and thus it is able to easily remove even large amounts of this gas produced by cracking of hydrocarbons.

From this point of view, a SIP able to develop a higher H$_2$ partial pressure (as in the case of pump β) would be even preferable compared to others characterised by a lower H$_2$ release but also by a lower pumping speed for CH$_4$. SIP characterisations performed with QMS under a constant incoming flux of CH$_4$ are hence useful for determining the best SIP configuration for the combination pump, which may not be necessarily the same as if the only SIP is adopted.

References

[1] M. Audi, "Pumping speed of sputter ion pumps," *Vacuum,* vol. 38, no. 8-10, pp. 669-671, 1988.

[2] ISO/TC 112/SC 3, "ISO/DIS 3556-1.2: Sputter-ion pumps - Measurement of performance characteristics," 1992.

[3] E. Fischer and H. Mommsen, "Monte Carlo computations on molecular flow in pumping speed test domes," *Vacuum,* vol. 17, no. 6, pp. 309-315, 1967.

[4] ASTM, "F798-97: Standard practice for determining gettering rate, sorption capacity and gas content of nonevaporable getters in the molecular flow region," 2002.

[5] R. Barre, G. Mongodin and F. Prevot, "Une méthode absolue de mesure des vitesses de pompage en régime moléculaire," *Le Vide,* vol. 11, p. 25, 1956.

[6] P. Clausing, *Ann. Physik,* vol. 12, p. 961, 1932.

[7] P. Clausing, "The flow of highly rarefied gases through tubes of arbitrary length," *J. Vac. Sci. Technol.,* vol. 8, p. 636, 1971.

[8] E. Brown and J. H. Leck, "Desorption of gas in the cold cathode ionization gauge," *Brit. J. Appl. Phys.,* vol. 6, no. 5, p. 161, 1955.

[9] J. E. Kelly and T. A. Vanderslice, "Pumping of hydrocarbons by ion pumps," *Vacuum,* vol. 11, no. 4, p. 205, 1961.

[10] A. Frennet and G. Liénard, "Analyse de mélanges hydrocarbure-deutérium à l'aide d'un spectromètre de masse évacué par une pompe ionique," *Le vide,* vol. 142, pp. 239-243, 1969.

[11] F. Williams, M. Boudart and A. Frennet, "Backstreaming of hydrogen when pumping hydrocarbons with an ion pump," *J. Vac. Sci. Technol.,* vol. 9, no. 1, pp. 362-365, 1972.

6. Results of sorption tests

Aim of this chapter is to resume the main results of the sorption tests performed in the laboratory on test-bench 6 with all the previously-described pumps.

In order to ease this resume, separate sections will be devoted to each of the following "families" of SIPs:

– conventional pumps, *i.e.* diode and noble-diode pumps;
– pumps with two bulk cathode plates, each one made of a different material;
– pumps with HUP cathodes.

In addition, a separate section is devoted to the resuming and description of the sorption tests of He, due to the peculiar behaviour of this gas and to the resulting data obtained. Finally, two dedicate sections also separately analyse the most important results obtained for heavier noble gases and CH_4, which represent the main focus of this study.

6.1. Diode and noble-diode pumps

Mechanical vacuum pumps (*e.g.*, turbomolecular pumps) provide a stable pumping speed for a given gas at a fixed pressure and thus their characteristic pumping speed curves are easily achievable and reproducible. In contrast, pumping speed of SIPs can greatly vary with time due to the influence of several factors and concurrent pumping mechanisms (pressure, chemically-active *vs.* noble gases, regurgitation of previously-sorbed gases, instabilities, attainment of saturation).

Prior to study new SIP configurations, it was therefore of paramount importance to determine whether the chosen testing method would allow obtaining reproducible results with SIPs of the same type or not.

A series of conventional diode and noble-diode SIPs has been therefore initially characterised and a standard testing sequence has been set, aiming at the obtainment of reproducible results for every SIP tested on the test-bench described in Chapter 5. Eight identical diode SIPs and three noble-diode ones (labelled *ND*) have been thoroughly characterised. All these pumps had a nominal N_2 pumping speed of 5 l/s and were indicated as IP-5; as already mentioned in Chapter 5, their design was largely the same of the IP-LAB pump later used to test the performance of innovative cathode materials, whose features and results will be described in the following sections.

6.1.1. Testing sequence and purging optimisation

Each pump underwent a series of sorption tests, which were intended to obtain an overview of its pumping properties for different gases (Ar, CH_4, He, N_2, O_2). The first diode pump, IP-5_01, was in-depth characterised with a long series of ASTM F798-97 tests alternatively at $P_g=3 \cdot 10^{-6}$ Torr and $P_g=3 \cdot 10^{-7}$ Torr, whose sequence is reported in Table 6-1. The applied voltage was always equal to 5 kV. The intent was to find any possible variation in pumping speed for a certain gas driven by gas sorbed during the previous steps of the sequence and particularly by the purging steps. As already mentioned, purging consists in the sorption at quite high pressure of large quantities of a gas able to cause an intense sputtering of the cathodes and thus the reemission of previously-pumped species, followed by their relocation in other positions providing a more stable pumping [1].

IP-5_01 underwent three purging phases: the first involved a unique sorption of O_2, while the others were made of two steps, namely Ar followed by O_2. Both two-steps purgings, in particular, followed a He tests, since the sorption of large quantities of He causes a substantial increase of its residual pressure stimulated by its tendency to easily re-diffuse from the cathodes (further details about He purging techniques are given in Section 6.6). Ar purging is very effective due to the large atomic mass of this gas (~40 u) and to its high sputter yield on cathode materials, resulting in a deeper cleaning of the pump. Moreover, being a noble gas it does not affect the subsequent pumping of chemically-active gases but

rather it creates a large amount of fresh sputtered Ti able to pump them. The purpose of using O_2 was in turn to remove as much Ar as possible from the cathodes, in order to prevent or, at least, delay the onset of instability. However, the main drawback of O_2 purging is given by the fact that a relatively high pressure of this gas may significantly alter the calibration and the functioning of the QMS, which should therefore remain preferably switched off during this kind of test.

Test	Set pressure [Torr]
Ar_1	$P_g = 3 \cdot 10^{-7}$
CH$_4$_1	$P_g = 3 \cdot 10^{-7}$
N$_2$_1	$P_g = 3 \cdot 10^{-6}$
O$_2$_1	**$P_g = 3 \cdot 10^{-6}$**
Ar_2	$P_g = 3 \cdot 10^{-7}$
CH$_4$_2	$P_g = 3 \cdot 10^{-7}$
N$_2$_2	$P_g = 3 \cdot 10^{-6}$
CH$_4$_3	$P_g = 3 \cdot 10^{-7}$
He_1	$P_g = 3 \cdot 10^{-6}$
Ar_3	**$P_g = 3 \cdot 10^{-6}$**
O$_2$_2	**$P_g = 3 \cdot 10^{-6}$**
He_2	$P_g = 3 \cdot 10^{-6}$
Ar_4	**$P_g = 3 \cdot 10^{-6}$**
O$_2$_3	**$P_g = 3 \cdot 10^{-6}$**

Table 6-1 – Testing sequence adopted exclusively for the pump IP-5_01; bold lines denote purging processes.

Test	Set pressure [Torr]
Ar_1	**$P_g = 3 \cdot 10^{-6}$**
O$_2$_1	**$P_g = 3 \cdot 10^{-6}$**
N$_2$_1	$P_g = 3 \cdot 10^{-6}$
CH$_4$_1	$P_m = 2 \cdot 10^{-6}$
CH$_4$_2	$P_m = 1 \cdot 10^{-6}$
Ar_2	$P_g = 3 \cdot 10^{-7}$
He_1	$P_g = 3 \cdot 10^{-6}$
O$_2$_2	**$P_g = 3 \cdot 10^{-6}$**

Table 6-2 – Standard sequence of tests on 5 l/s diode and noble-diode SIPs; bold lines denote purging processes.

This consequently results in a complete loss of data about the evolution of partial pressures during the purging. On the contrary, the length of every purging should be determined by the time needed to reduce all the partial pressure of previously-sorbed gases to a constant value, much lower than the partial pressure of the purging gas.

In order to deal with the large number of pumps to be tested, a shorter sequence (cf. Table 6-2) was later adopted for all the subsequent characterisations (all the measurements were performed applying a voltage equal to 5 kV). Unlike the first one, this new sequence included a two-step $Ar+O_2$ purging at the very beginning: when a SIP is installed in a vacuum system and starts pumping for the first time, the sputtering of residual gas ions stimulates a significant release of contaminants adsorbed in the first layers, which results in a pressure increase and in low pumping speeds. A purging at higher pressure fosters this stimulated desorption and speeds up the restoration of a cleaner atmosphere with a lower level of residual impurities.
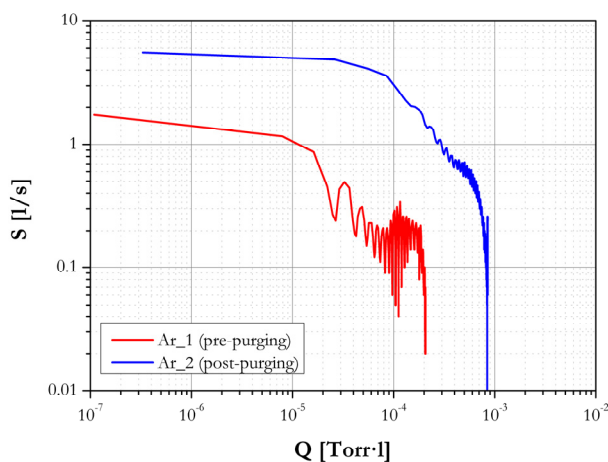
Figure 6-1 – ASTM F798-97 tests Ar_1 and Ar_2, performed at $P_g=3 \cdot 10^{-7}$ Torr on IP-5_01 before and after the first purging, respectively.

Tests on IP-5_01 demonstrated the importance of this initial purging on the performance of a new SIP. Figure 6-1 shows the two initial ASTM F798-97 sorption curves Ar_1 and Ar_2, obtained at $P_g=3 \cdot 10^{-7}$ Torr before and after the

first O_2 purging, respectively. Although being both heavily affected by strong fluctuations caused by the unsuitable conductance and procedure (cf. Chapter 5), the gain of Ar_2 in terms of pumping speed and sorbed quantity of gas is evident; this increase resulted from the purging effect of the previous O_2_1 and N_2_1 sorptions at $P_g=3\cdot10^{-6}$ Torr (cf. Table 6-1).

The chance to significantly reduce the number of tests in the adopted sequence was fostered by the awareness (gained during tests on the first pump) that, once reached saturation, pumping speed of a SIP for a certain gas is always the same, regardless of the previous pumping history; indeed, the attainment of saturation itself implies that the influence of other residual species on the main gas under test has become negligible. In addition, the second testing sequence (Table 6-2) implemented the already-mentioned adoption of CH_4 sorption tests at constant P_m instead of conventional ASTM F798-97 trials at constant P_g, as explained in Chapter 5. Further improvements concerning the installation of a new smaller conductance and the adoption of tests at constant P_m also for Ar, which are discussed in detail in Chapter 5, were instead implemented at the end of this series of tests on conventional diode and noble-diode SIPs, thanks to the experience gained during these initial characterisations.

6.1.2. Sorption tests: diode and noble-diode pumps

		Ar	N_2	CH_4
Set pressure [Torr]		$P_g=3\cdot10^{-6}$	$P_g=3\cdot10^{-6}$	$P_m=2\cdot10^{-6}$
IP-5	**S [l/s]**	0.27	3.5	~6.5
	S_{QMS} [l/s]	0.27	4.5	~15
IP-5 ND	**S [l/s]**	0.60	3.5	~6.5
	S_{QMS} [l/s]	0.80	4.5	~15

Table 6-3 – Summary of pumping speeds of Ar, N_2 and CH_4 measured with diode and noble-diode IP-5 pumps.

Ar, N_2 and CH_4 pumping speeds S and real pumping speeds S_{QMS} of the diode and noble-diode IP-5s tested are summarised in Table 6-3. This cycle of analyses demonstrated that measurements of this kind are well reproducible if pumps of the same type are tested according to the same procedure. Moreover,

the results of the first pump IP-5_01 were also in good agreement with those of the other SIPs, regardless of the differences in the adopted testing sequence.
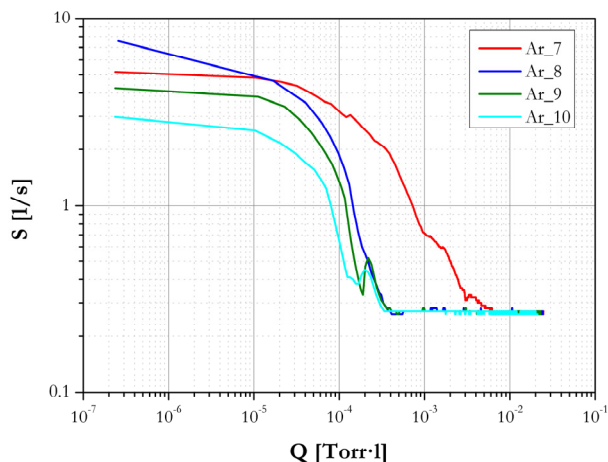
Figure 6-2 – Series of four consecutive Ar sorptions at $P_m=5\cdot10^{-5}$ Torr by a single diode SIP. Bumps of Ar_9 and Ar_10 around $Q=2\cdot10^{-4}$ Torr·l are most likely due to a sudden gas release from the SIP electrodes; QMS data are however not available.

Pumping speed for Ar was thoroughly investigated and the values in Table 6-3 were confirmed by more precise analyses made after the adoption of the optimised experimental setup and the consequent disappearance of unwanted fluctuations. A series of consecutive Ar sorptions made with a single diode pump at $P_m=5\cdot10^{-5}$ Torr confirmed the significance of pumping speed *after* saturation for the performance evaluation of SIPs. Large variations of S were observed at low values of Q, due to the specific residual-gas conditions of the vacuum system at the beginning of each test (cf. Figure 6-2); conversely, a univocal value S=0.27 l/s was measured in all cases after saturation. It is also interesting to note how saturation was reached much later (in terms of quantity Q of sorbed gas) during the first test Ar_7 compared to the following ones. This is a further proof of the beneficial effects of purging on SIP performances: as a pump becomes cleaner thanks to purging, the initial transient becomes increasingly shorter. As already mentioned in Chapter 2, this transient state occurs during the initial phase of a sorption test, when a prominent fraction of the pumping occurs through ion burial

into the cathodes. Afterwards, as the concentration of implanted ions in the first cathode layers grows, this pumping effect is progressively balanced by re-sputtering from the cathodes themselves and thus the net pumping speed decreases [2].

Tests for N_2, CH_4 and O_2 were also well reproducible and did not put in evidence any substantial difference between diode and noble-diode pumps. As already mentioned in Chapter 5, the large discrepancy between S and S_{QMS} while pumping CH_4 intrinsically results from the pumping mechanism of this gas, which relies on the cracking of molecules and the production of H_2. S takes therefore into account also the contribution of H_2, which is often the main residual gas during the sorption of CH_4. S_{QMS} gives instead an indication of pumping speed for the sole CH_4.
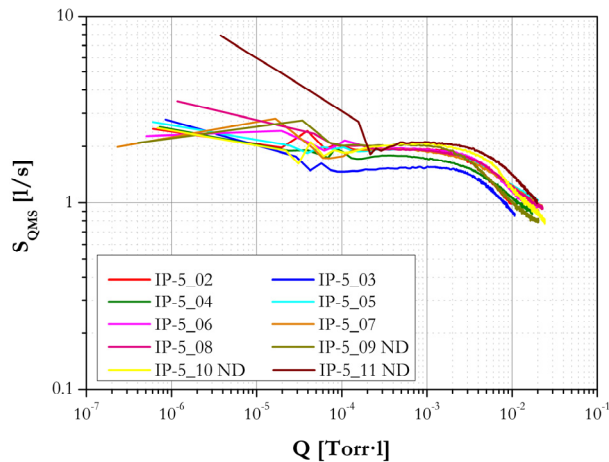
Figure 6-3 – ASTM F798-97 He sorption curves at P_g=3·10⁻⁶ Torr of diode and noble-diode IP-5 pumps.

On the other side, the pumping of He deserves a separate discussion. First, unlike the other gases, there was a much wider variance among the sorption curves of the pumps under test. Secondly, although being a noble gas, He was not pumped with higher pumping speed by noble-diode SIPs: indeed, their sorption curves were perfectly equivalent to those of diode ones (Figure 6-3). This condition is determined by the fact that the role of the energetic neutrals in the

pumping of He is limited: thus, using a noble-diode SIP instead of a diode one does not give any advantage when pumping this gas [3]. Lastly, the attainment of saturation conditions while pumping He was not as straightforward as in the case of other gases.

As a matter of fact, all these SIPs pumped about $2 \cdot 10^{-2}$ Torr·l of He and not all of them had the chance to reach saturation before the end of its test. This upper limit of Q was dictated by time constraints in the measurement schedule and by the choice not to sorb excessive quantities of this gas, whose residual pressure might be subsequently heavily affected by its continuous desorption from the inner surfaces of the vacuum system. Consequently, saturation values of He pumping speed were recorded only for few pumps: Figure 6-4 shows that saturation pumping speed was comparable to that typical of Ar (0.27 l/s).
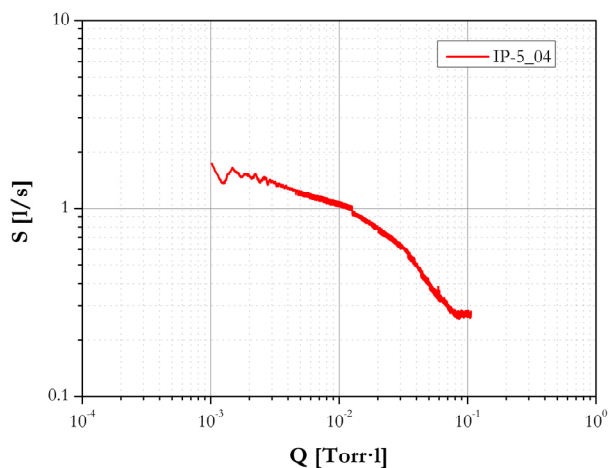
Figure 6-4 – ASTM F798-97 He sorption curve at P_g=3·10^{-6} Torr of a diode IP-5 pump.

6.2. Pumps with cathodes made of different materials

This section resumes the characterisation of bulk cathode plates made of metals other than Ti. In addition, some couples of cathodes made of two different materials were also tested. All the tested configurations are listed in Chapter 4.

These tests were performed using the pump IP-LAB described in Chapter 5, which allowed to easily substitute each time only the electrodes without the need to replace all the other components of the SIP. Conventional Ti-Ti cathodes have been also initially tested in IP-LAB; since the adherence of Ti-Ti IP-LAB results to those of diode IP-5 pumps was very good, it was possible to rule out any possible influence of the IP-LAB design on the pumping performance of cathodes identical to those installed in IP-5 pumps.

Following the optimisation made while characterising standard diode and noble-diode SIPs, the testing sequence adopted for tests on IP-LAB was largely different (Table 6-4). The series of tests was further reduced, in order to better deal with the large number of configurations to be tested. Sorptions of O_2, which had been initially conceived for purging purposes, were deleted as well as CH_4 and Ar tests at lower pressures. A sorption of Ne was instead added to the sequence; Kr sorption tests were instead performed on part of the pumps only. Moreover, CH_4 and heavy noble gas tests were all performed setting a constant pressure value $P_m=5\cdot10^{-5}$ Torr at the gas inlet (that is, with a constant flux of gas entering the main vessel pumped by the SIP under examination).

Test	Set pressure [Torr]	Type of test
Ar_1	$P_m=5\cdot10^{-5}$	Constant flux
N$_2$_1	$P_g=3\cdot10^{-6}$	ASTM F798-97
CH$_4$_1	$P_m=5\cdot10^{-5}$	Constant flux
Ne_1	$P_m=5\cdot10^{-5}$	Constant flux
He_1	$P_g=3\cdot10^{-6}$	ASTM F798-97
Ar_2	$P_m=5\cdot10^{-5}$	Constant flux
(Kr_1)	$(P_m=5\cdot10^{-5})$	(Constant flux)

Table 6-4 – Testing sequence adopted for the characterisation of cathodes in IP-LAB. The final Kr test was not initially included in the sequence and was later introduced.

6.2.1. Ar sorption tests

Figure 6-5 shows the Ar pumping speeds S_{QMS} measured at $P_m=5\cdot10^{-5}$ Torr with couples of identical bulk cathodes; pairs of two different cathode plates are instead shown in Figure 6-6. Table 6-5 and Table 6-6 resume for each curve the

corresponding saturation pumping speed values and their ratios $S_{QMS}/S_{QMS,Ti}$ with saturation pumping speed of Ti-Ti cathodes.
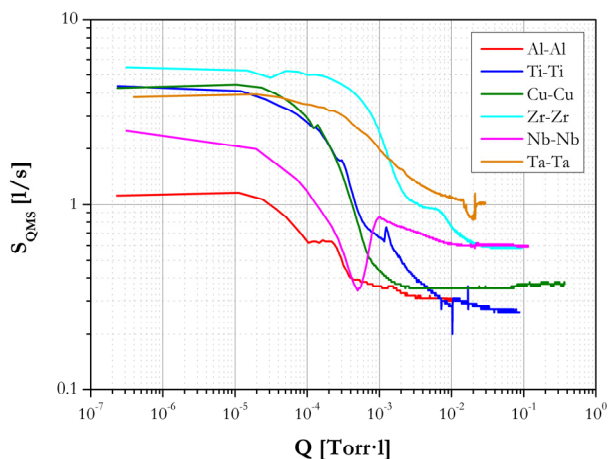
Figure 6-5 – S_{QMS} during Ar sorption tests at $P_m=5\cdot10^{-5}$ Torr with pairs of identical cathodes: Ti-Ti, Ta-Ta, Al-Al, Cu-Cu, Nb-Nb and Zr-Zr.

	Ar_1		**Ar_2**	
Cathodes	**S_{QMS} [l/s]**	***$S_{QMS}/S_{QMS,Ti}$***	**S_{QMS} [l/s]**	***$S_{QMS}/S_{QMS,Ti}$***
Al-Al	0.18	*0.62*	0.30	*1.15*
Ti-Ti	0.29	---	0.26	---
Cu-Cu	0.26	*0.90*	0.37	*1.42*
Zr-Zr	0.59	*2.03*	0.56	*2.15*
Nb-Nb	0.56	*1.93*	0.59	*2.27*
Ta-Ta	0.98	*3.38*	1.01	*3.88*

Table 6-5 – Saturation values of S_{QMS} during tests Ar_1 and Ar_2 at $P_m=5\cdot10^{-5}$ Torr with pairs of identical cathodes; the ratio $S_{QMS}/S_{QMS,Ti}$ is also showed for every material.

These results seem to indicate that saturation pumping speed tends to be higher for cathodes having a higher atomic mass. It is worth mentioning that the overall pumping speed S measured for Ta-Ta cathodes after saturation was only 0.65 l/s both during Ar_1 and Ar_2. The QMS data revealed however that, even at

saturation, a significant and constant fraction of H_2 was still present, probably due to a non-optimal annealing thermal treatment of Ta cathodes prior to the installation in IP-LAB. The corresponding calculated values of Ar pumping speed S_{QMS} at saturation were instead equal to 0.98 l/s and 1.01 l/s. This is a further proof of the need to use a QMS during the characterisation of SIPs, especially when their performance should be evaluated in view of the coupling with another pump.
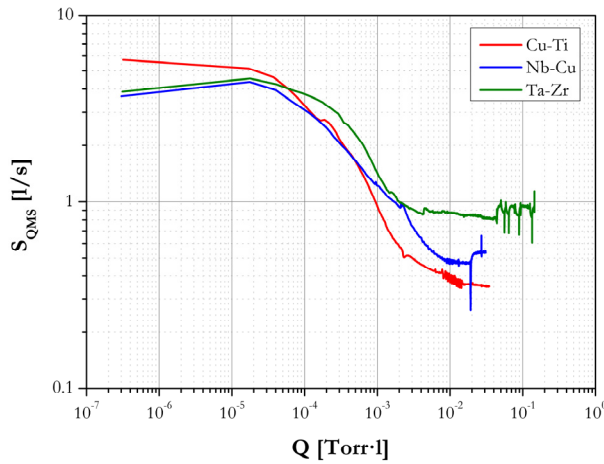
Figure 6-6 – S_{QMS} during Ar sorption tests at $P_m=5\cdot10^{-5}$ Torr with pairs of different cathodes: Cu-Ti, Cu-Nb and Ta-Zr.

Cathodes	Ar_1		Ar_2	
	S_{QMS} [l/s]	$S_{QMS}/S_{QMS,Ti}$	S_{QMS} [l/s]	$S_{QMS}/S_{QMS,Ti}$
Ti-Ti	0.29	---	0.26	---
Cu-Ti	0.38	*1.31*	0.35	*1.35*
Nb-Cu	0.54	*1.86*	0.54	*2.08*
Ta-Zr	0.94	*3.24*	0.96	*3.69*

Table 6-6 – Saturation values of S_{QMS} during tests Ar_1 and Ar_2 at $P_m=5\cdot10^{-5}$ Torr with pairs of two different cathodes; the ratio $S_{QMS}/S_{QMS,Ti}$ is also showed for every coupling of materials.

Unlike the other materials—for which saturation pumping speed was in every case well-reproducible—non-negligible discrepancies were observed in the final pumping speed values of Cu-Cu (Figure 6-7a) and Al-Al (Figure 6-7b) cathodes. In both cases, S_{QMS} during Ar_1 was significantly lower compared to Ar_2; a second pair of Cu-Cu cathodes was also tested but the same tendency arose. Though the reason for this behaviour is unclear, it might be related to the fact that, among the metals under exam, only Al and Cu do not have any gettering ability in HV and UHV conditions. Even though Ar is a non-getterable gas, its equilibrium pumping speed might be in some way influenced by the simultaneous sorption of other getterable residual gases or by the sorption of N_2 and CH_4 between Ar_1 and Ar_2. Moreover, only Al and Cu have a face-centred cubic (FCC) crystal structure, whilst all the other metals are body-centred cubic (BCC) or hexagonal close-packed (HCP). Any possible connection between crystal structure and sorption performance, however, still needs to be further investigated.
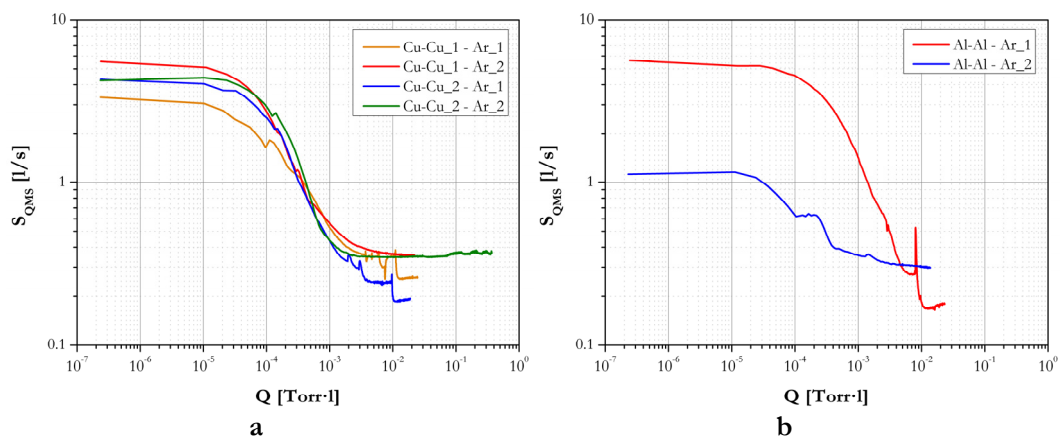
Figure 6-7 – S_{QMS} during Ar sorption tests at $P_m=5\cdot10^{-5}$ Torr with a) Cu cathodes and b) Al cathodes.

6.2.2. N_2 sorption tests

While Ar results were quite univocal, those for N_2 did not evidence a clear trend. Except for Cu-Cu cathodes, whose pumping speed was by far the lowest, all the others were found to be more or less equivalent, both at the beginning of the test and in proximity of saturation conditions (Figure 6-8a). Neither any possible

dependence on the cathode atomic mass was noticed, nor any particular difference between Ti-Ti and all the other configurations. This reflects the fact that the way of pumping N_2 in SIPs is completely different from the sorption mechanisms typical of Ar. Quite surprisingly, Al-Al cathodes were not among the worst ones, in spite of their very scarce gettering ability. On the other side, the results obtained with Ta-Ta cathodes denote the less-pronounced getter properties of this material compared to Zr and Ti, whose pumping speeds—together with Nb—were higher. No difference at all was instead noticeable among the three pairs of different cathodes, each one comprising Ti, Nb or Zr, respectively (Figure 6-8b).
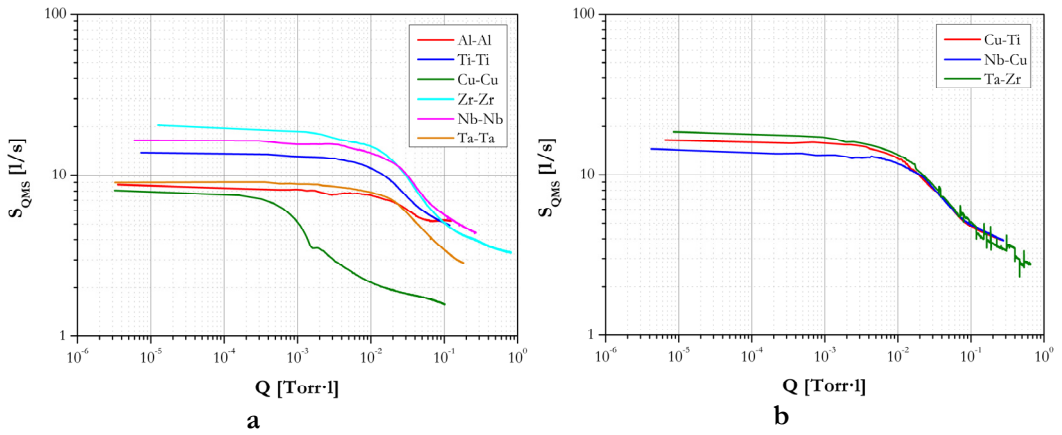
Figure 6-8 – S_{QMS} during N_2 sorption tests at $P_g=3\cdot10^{-6}$ Torr with pairs of a) identical cathodes and b) two different ones.

6.2.3. CH_4 sorption tests

CH_4 results were even less straightforward. As already explained in Chapter 5, the analysis of CH_4 sorption curves cannot omit neither the corrected pumping speed S_{QMS} (Figure 6-9a-b) nor the overall S (Figure 6-10a-b), since the pumping of CH_4 through cracking and ionisation intrinsically gives rise to the production of significant quantities of H_2. Furthermore, under these conditions, a real saturation value of pumping speed can never be achieved; S and S_{QMS} values in Table 6-7 refer therefore to an arbitrary quantity of sorbed gas (*i.e.*, $Q=2\cdot10^{-2}$ Torr·l).

Nb-Nb and Zr-Zr were the best configurations, with both S and S_{QMS} about 10–15% times higher than the corresponding values of Ti-Ti cathodes. On the

contrary, Cu-Cu were by far the worst ones, both in terms of S and S_{QMS} (only 14% and 33% compared to Ti-Ti, respectively), due to their lack of gettering ability for H_2. Al-Al cathodes were instead very poor in terms of S but almost comparable to Ti-Ti when considering S_{QMS} (41% and 89%, respectively). S and S_{QMS} of Ta-Ta cathodes were 69% and 78% of the corresponding Ti-Ti values, probably reflecting the lower getter properties of Ta and being influenced, again, by the non-optimal thermal treatment.
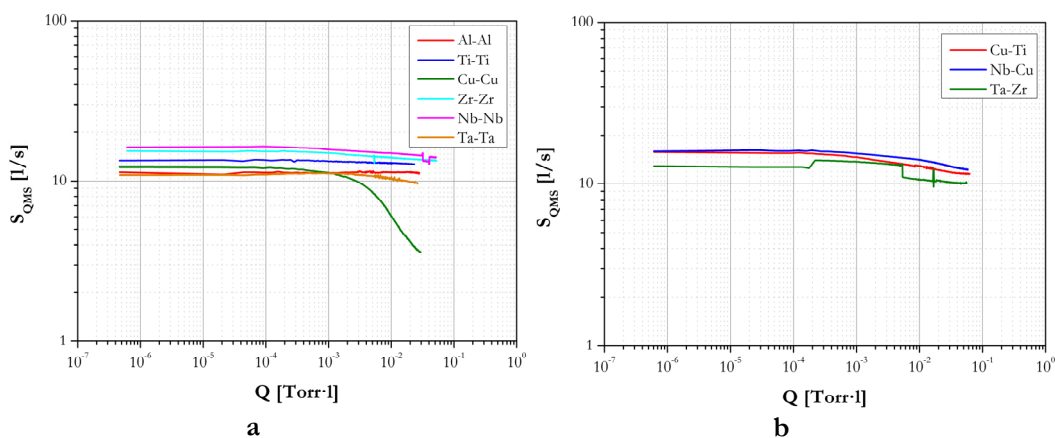
Figure 6-9 – S_{QMS} during CH_4 sorption tests at $P_m=5\cdot10^{-5}$ Torr, for $Q=2\cdot10^{-2}$ Torr·l, with pairs of a) identical cathodes and b) two different ones.

CH$_4$_1				
Cathodes	S [l/s]	S/S_{Ti}	S_{QMS} [l/s]	$S_{QMS}/S_{QMS,Ti}$
Al-Al	2.87	0.41	11.32	0.89
Ti-Ti	7.03	---	12.70	---
Cu-Cu	1.01	0.14	4.19	0.33
Zr-Zr	7.56	1.08	13.74	1.08
Nb-Nb	7.89	1.12	14.57	1.15
Ta-Ta	4.84	0.69	9.92	0.78
Cu-Ti	5.60	0.80	12.23	0.96
Nb-Cu	6.07	0.86	13.44	1.06
Ta-Zr	4.70	0.67	10.44	0.82

Table 6-7 – Reference values of S_{QMS} taken during tests CH$_4$_1 at $P_m=5\cdot10^{-5}$ Torr, at $Q=2\cdot10^{-2}$ Torr·l, with pairs of two different cathodes; the ratio $S_{QMS}/S_{QMS,Ti}$ is also showed for every coupling of materials.

The performance of Nb-Cu (86% and 106%) and Cu-Ti (80% and 96%) were still rather high, thanks to the presence of Nb and Ti, but in any case lower than others, due to the influence of the Cu cathode, especially when considering the overall S and thus also the sorption of H_2. Ta-Zr cathodes (67% and 82%) were in line with Ta-Ta ones, in spite of having one Zr component.
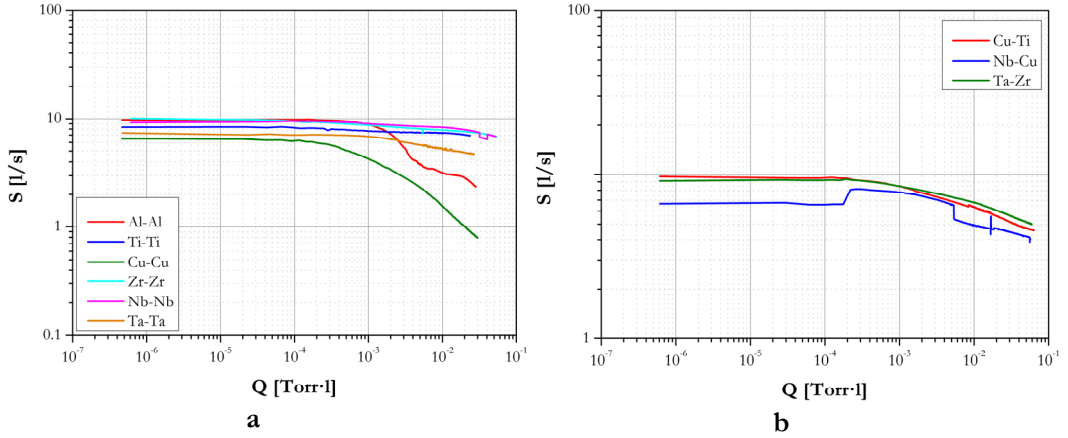
Figure 6-10 – S during CH_4 sorption tests at $P_m=5\cdot10^{-5}$ Torr, for $Q=2\cdot10^{-2}$ Torr·l, with pairs of a) identical cathodes and b) two different ones.

6.2.4. Ne sorption tests

Ne sorption tests overall followed the same trend observed with Ar, confirming the influence of the high-energy neutrals theory on the sorption of both these noble gases. Sorption curves made at $P_m=5\cdot10^{-5}$ Torr are shown in Figure 6-11a-b; the corresponding saturation values of pumping speed S_{QMS} and their ratio to Ti-Ti cathodes are resumed in Table 6-8.

Again, saturation pumping speed seemed to be somehow proportional to the mean atomic mass of the cathode materials. The overall pumping speed S of Ta-Ta cathodes was also in this case much lower than expected (0.49 l/s), while the corrected value $S_{QMS}=0.82$ l/s, net of H_2 influence, was in line with the above-mentioned trend. As for Ar and unlike N_2 and CH_4, Cu-Cu and Cu-Ti cathodes were not among the worst but simply followed the same trend as the other cathode configurations.
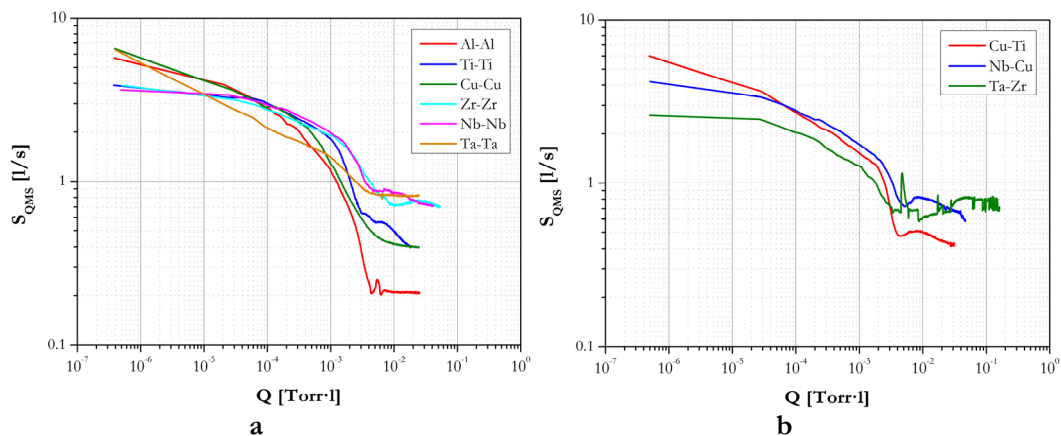
Figure 6-11 – S$_{QMS}$ during Ne sorption tests at P$_m$=5·10^{-5} Torr with pairs of a) identical cathodes and b) two different ones.

Ne_1		
Cathodes	**S$_{QMS}$ [l/s]**	*S$_{QMS}$/S$_{QMS,Ti}$*
Al-Al	0.21	*0.57*
Ti-Ti	0.37	---
Cu-Cu	0.40	*1.08*
Zr-Zr	0.70	*1.89*
Nb-Nb	0.71	*1.92*
Ta-Ta	0.82	*2.22*
Cu-Ti	0.43	*1.16*
Nb-Cu	0.59	*1.59*
Ta-Zr	0.80	*2.16*

Table 6-8 – Saturation values of S$_{QMS}$ during test Ne_1 at P$_m$=5·10^{-5} Torr with pairs of two different cathodes; the ratio S$_{QMS}$/S$_{QMS,Ti}$ is also showed for every coupling of materials.

6.3. Pumps with HUP cathodes

This section summarises the results of sorption tests made with HUP cathodes assembled in IP-LAB. The adopted testing schedule was the same described in the previous section (Table 6-4) and used for IP-LAB characterisations of pairs of identical bulk cathode plates and couplings of two different ones.

6.3.1. Ar sorption tests
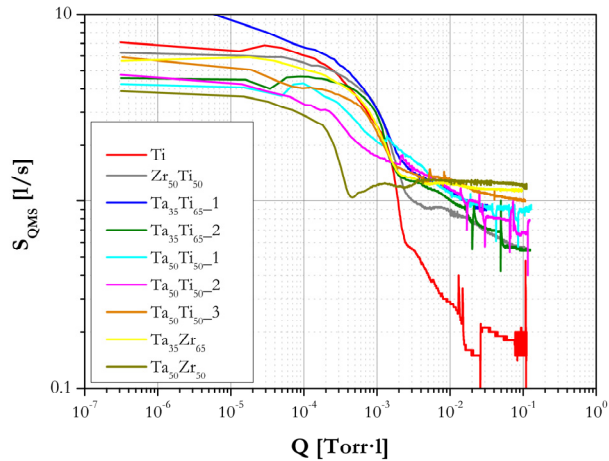
Figure 6-12 – S_{QMS} measured during Ar_1 sorption tests at $P_m=5\cdot10^{-5}$ Torr with several pairs of HUP cathodes.

Figure 6-12 shows the S_{QMS} curves of HUP pumps measured during the first sorption test Ar_1 at $P_m=5\cdot10^{-5}$ Torr. All these curves evolved in the same way: pumping speeds were initially comprised between 4 l/s and 7 l/s, before progressively decreasing until the attainment of their saturation values (generally around Q=0.1 Torr·l). Depending on the performance at saturation and on the elemental composition, HUP cathodes can be divided in three groups:

  – TaZr cathodes, whose pumping speeds were higher than 1.1 l/s;

−   TaTi and ZrTi cathodes, with pumping speeds comprised between 0.5 l/s and 1 l/s;

Ti cathodes, characterised by the lowest pumping speed observed (less than 0.2 l/s) and by the insurgence of strong fluctuations.

Table 6-9 gives an overview of all the measured saturation values of S_{QMS} of tests Ar_1; the ratio of each of them over the corresponding S_{QMS}=0.29 l/s of Ti-Ti cathodes (cf. Table 6-5) was also calculated. Ti HUP cathodes were specifically conceived in order to make possible a direct comparison between HUP cathodes and conventional diode ones, subjected to the same thermal treatment (3 h at 600 °C) and of the same elemental composition. It is worth noting that saturation pumping speed of these Ti HUP cathodes was only 62% of that measured with Ti-Ti bulk plates (0.18 l/s *vs.* 0.29 l/s). Conversely, saturation pumping speeds of $Ta_{35}Ti_{65}$ and $Ta_{50}Ti_{50}$ cathodes (with the exception of $Ta_{35}Ti_{65}$_2) were generally higher than that of a conventional noble-diode IP-5 pump, with one Ti and one Ta cathode, always at P_m=5·10^{-5} Torr. Moreover, pumping speed of this noble-diode pump was only 60% of those of both TaZr HUP mixtures.

Cathodes	Ar_1		Ar_2	
	S_{QMS} [l/s]	*$S_{QMS}/S_{QMS,Ti}$*	S_{QMS} [l/s]	*$S_{QMS}/S_{QMS,Ti}$*
Ti HUP	0.18	*0.62*	0.17	*0.65*
$Zr_{50}Ti_{50}$	0.56	*1.93*	0.53	*2.04*
$Ta_{35}Ti_{65}$_1	0.91	*3.14*	0.81	*3.12*
$Ta_{35}Ti_{65}$_2	0.54	*1.86*	0.76	*2.92*
$Ta_{50}Ti_{50}$_1	0.91	*3.14*	0.90	*3.46*
$Ta_{50}Ti_{50}$_2	0.78	*2.69*	0.91	*3.50*
$Ta_{50}Ti_{50}$_3	1.00	*3.45*	0.95	*3.65*
$Ta_{35}Zr_{65}$	1.20	*4.14*	1.11	*4.27*
$Ta_{50}Zr_{50}$	1.14	*3.93*	1.11	*4.27*
IP-5 ND	0.72	*2.48*	0.68	*2.62*

Table 6-9 – Saturation values of S_{QMS} during tests Ar_1 and Ar_2 at P_m=5·10^{-5} Torr with HUP cathodes; the ratio $S_{QMS}/S_{QMS,Ti}$ is also showed for every HUP composition ($S_{QMS,Ti}$=0.29 l/s or 0.26 l/s refers to Ti-Ti cathodes during Ar_1 or Ar_2, respectively).
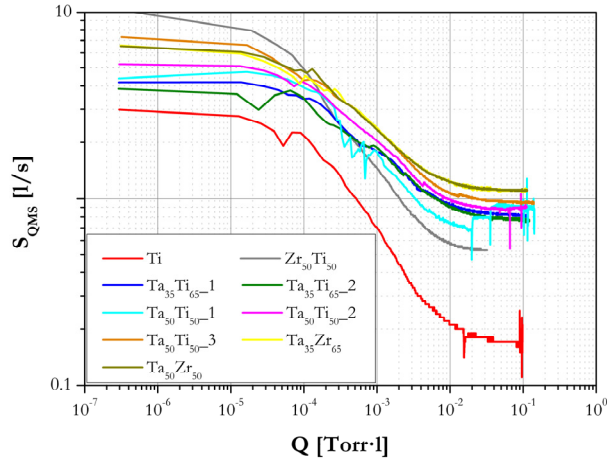
Figure 6-13 – S$_{QMS}$ measured during Ar_2 sorption tests at P$_m$=5·10^{-5} Torr with several pairs of HUP cathodes.

In parallel, Table 6-9 resumes also the saturation values measured during tests Ar_2 (*i.e.*, at the end of the testing sequence) and the corresponding ratios S$_{QMS}$/S$_{QMS,Ti}$ (this time referring to S$_{QMS}$=0.26 l/s of Ti-Ti bulk cathodes during test Ar_2). The entire sorption curves recorded during Ar_2 tests are shown in Figure 6-13 and confirm the trend of Ar_1 ones: Ti HUP cathodes were the worst performing (only 65% of conventional Ti-Ti ones), while all the tested TaTi HUP combinations resulted in saturation pumping speeds higher than that of the noble-diode IP-5 pump. Again, the highest values were obtained with TaZr HUP cathodes.

6.3.2. N₂ sorption tests
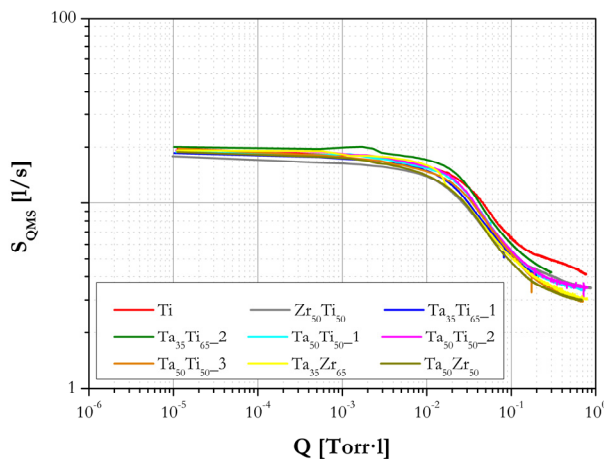
Figure 6-14 – S$_{QMS}$ measured during N₂_1 sorption tests at P$_g$=3·10^{-6} Torr with several pairs of HUP cathodes.

The sorption curves of ASTM F798-97 tests N₂_1 at P$_g$=3·10^{-6} Torr of HUP cathodes are shown in Figure 6-14. Contrary to the case of Ar, the differences in the pumping of N₂ were minimal among the several tested HUP compositions. Pumping speed S$_{QMS}$ was initially the same (about 20 l/s) for all the cathodes; little if any discrepancy was also noticeable in the progressive decrease towards saturation of each curve. These values were similar to those shown in the previous section for bulk cathode plates.

6.3.3. CH₄ sorption tests

Also in this case, the analysis of CH₄ sorption tests at P$_m$=5·10^{-5} Torr should necessarily include the evolution of the overall pumping speeds S (which takes into account also the pumping of H₂) as well as S$_{QMS}$.
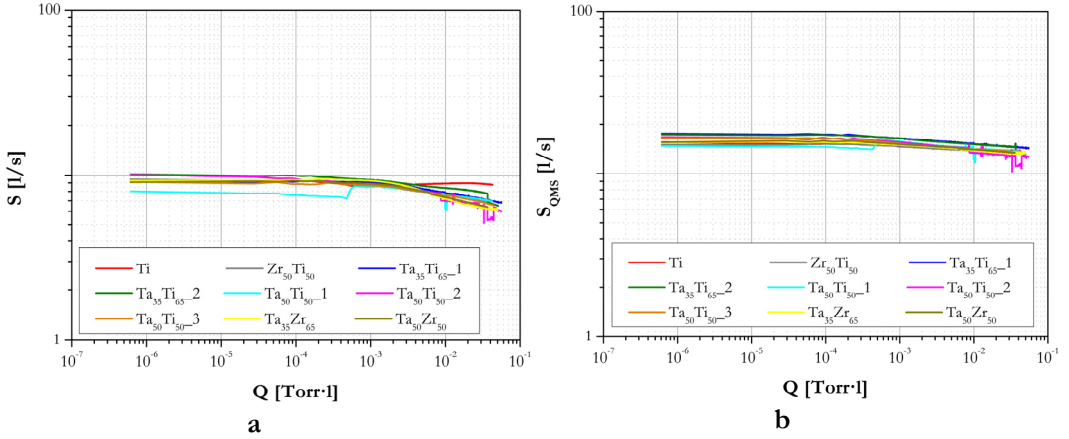
Figure 6-15 – a) S and b) S_{QMS} measured during CH_4 sorption tests at $P_m=5\cdot10^{-5}$ Torr with several pairs of HUP cathodes.

	CH_4_1			
Cathodes	**S [l/s]**	*S/S_{Ti}*	**S_{QMS} [l/s]**	*$S_{QMS}/S_{QMS,Ti}$*
Ti HUP	8.97	*1.28*	14.10	*1.11*
$Zr_{50}Ti_{50}$	7.24	*1.03*	13.69	*1.08*
$Ta_{35}Ti_{65}\_1$	7.46	*1.06*	14.95	*1.18*
$Ta_{35}Ti_{65}\_2$	8.14	*1.16*	14.95	*1.18*
$Ta_{50}Ti_{50}\_1$	7.35	*1.05*	14.10	*1.11*
$Ta_{50}Ti_{50}\_2$	6.81	*0.97*	13.31	*1.05*
$Ta_{50}Ti_{50}\_3$	7.15	*1.02*	13.98	*1.10*
$Ta_{35}Zr_{65}$	6.59	*0.94*	13.58	*1.07*
$Ta_{50}Zr_{50}$	6.83	*0.97*	13.86	*1.09*
IP-5 ND	8.79	*1.25*	15.02	*1.18*

Table 6-10 – Reference values of S_{QMS} taken during tests CH_4_1 at $P_m=5\cdot10^{-5}$ Torr, at $Q=2\cdot10^{-2}$ Torr·l, with HUP cathodes; the ratios of S and S_{QMS} to the corresponding values of Ti-Ti bulk cathodes (S=7.03 l/s and $S_{QMS}=12.70$ l/s, respectively) are also shown.

Figure 6-15a depicts the former ones, showing that little if any difference was noticeable among the various HUP compositions. The S values collected at $Q=2\cdot10^{-2}$ Torr·l and resumed in Table 6-10 show that most of these cathodes had substantially the same pumping speed of the reference Ti-Ti bulk ones; only Ti HUP cathodes resulted in a value 28% higher than the reference and close to the

one of the conventional noble-diode IP-5. The S_{QMS} curves in Figure 6-15b highlight an even less pronounced discrepancy among the tested HUP cathodes, which were all essentially equivalent to both the reference pump and the noble-diode one (Table 6-10).

A more comprehensive analysis of these CH_4 sorption tests, together with those performed on non-HUP cathodes made of different materials (Section 6.2.3), is given in the following (Section 6.5).

6.3.4. Ne sorption tests

The Ne sorption tests at $P_m=5\cdot10^{-5}$ Torr (Figure 6-16) followed the same trends observed with Ar, thus confirming that the SIP pumping mechanisms for these two gases are largely the same. All the pumping speeds S_{QMS} measured after saturation are shown in Table 6-11; the ratio $S_{QMS}/S_{QMS,Ti}$ was calculated using the reference value $S_{QMS}=0.37$ l/s of Ti-Ti bulk cathodes.
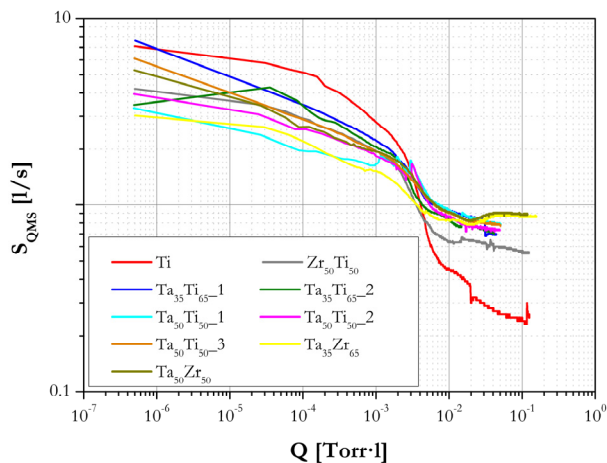
Figure 6-16 – S_{QMS} measured during Ne_1 sorption tests at $P_m=5\cdot10^{-5}$ Torr with several pairs of HUP cathodes.

The fraction of reference pumping speed ensured by the Ti HUP cathodes (68%) was comparable to the analogous Ar case. Again, TaZr cathodes gave the

best results, even if their Ne pumping speeds were lower compared to those measured for Ar. As for Ar, the performance of TaTi mixtures were in between these two extremes; their pumping speed were all about twice the reference one. Further aspects about this clear analogy between the pumping of Ar and Ne by SIPs in a wide range of cathode atomic masses are detailed in Section 6.4.

Ne_1		
Cathodes	**S_{QMS} [l/s]**	**$S_{QMS}/S_{QMS,Ti}$**
Ti HUP	0.25	*0.68*
$Zr_{50}Ti_{50}$	0.55	*1.49*
$Ta_{35}Ti_{65}\_1$	0.83	*2.24*
$Ta_{35}Ti_{65}\_2$	0.71	*1.92*
$Ta_{50}Ti_{50}\_1$	0.78	*2.11*
$Ta_{50}Ti_{50}\_2$	0.73	*1.97*
$Ta_{50}Ti_{50}\_3$	0.78	*2.11*
$Ta_{35}Zr_{65}$	0.87	*2.35*
$Ta_{50}Zr_{50}$	0.89	*2.41*
IP-5 ND	0.71	*1.92*

Table 6-11 – Saturation values of S_{QMS} during tests Ne_1 at $P_m=5\cdot10^{-5}$ Torr with HUP cathodes; the ratio $S_{QMS}/S_{QMS,Ti}$ is also showed for every HUP composition ($S_{QMS,Ti}=0.37$ l/s refers to Ti-Ti bulk cathodes).

6.4. Observations about the sorption of heavy noble gases

The data collected and presented in the previous sections allow some worthy observations about the pumping of noble gases by the experimental SIPs so far tested, other than conventional diode and noble-diode ones. A clear picture emerges from the analysis of these data, namely that saturation pumping speeds for Ar and Ne are strictly influenced by the mean atomic mass A of the cathode materials. This trend is clear for both couples of different cathode materials and HUP cathodes, however with some distinctions between these two groups, as will be explained in detail in the following.

6.4.1.   Bulk cathodes made of different materials

The sorption of noble gases by SIPs with innovative cathodes is one of the main focuses of this work. This section resumes the results obtained with pairs of bulk cathodes made of different materials (*viz.*, Al, Ti, Cu, Zr, Nb, Ta), which are presented in Section 6.2. This topic and its related results are of particular interest and were addressed also in a paper recently published on *Vacuum* in the form of a short communication[1].

As already mentioned, the mechanism of high-energy neutrals described by Jepsen [2] [4] led to the development of noble-diode pumps, which ensure higher sorption rates for noble gases (compared to diode SIPs) and avoid Ar instability. Apart from this, few other studies have been published in the past decades about the influence of the atomic mass on the sorption of noble gases. Vaumoron and De Biasio [5] found that stability is determined by the ratio R between the mean atomic mass of the cathode materials and that of the impinging gas ions: for a given pump geometry, there is a minimum R_{min} (~2.5 for flat cathodes) such that for $R > R_{min}$ the pump is stable and, the larger is R, the higher is the pressure at which instability can occur. Baker and Laurenson [6] studied instead the pumping behaviour of some combinations of Al, Ti, and Ta cathodes with He, Ne, Ar, and Kr; their conclusion was that pumping speed S is generically dependent on the same ratio R according to the following relationship, which results in the fact that pumping speed is higher when heavier cathodes pump lighter gases:

$$S \propto \log R$$

Lamont [7], on the basis of the energetic-neutrals theory, also found that Ar pumping speed of different cathode materials (*viz.*, Ti, Nb, Mo, Ta) is determined by their atomic masses.

The present experimental results can be therefore analysed in light of these considerations. Table 6-12 resumes the couplings of bulk cathode materials under exam; for each coupling, the mean atomic mass A (in atomic mass units) is also reported. Clearly, Ti-Ti and Ta-Ti correspond to conventional diode and noble-diode SIPs, respectively.

---

[1] T. Porcelli, F. Siviero, G. Bongiorno, P. Michelato, C. Pagani, "Influence of the cathode materials on the sorption of noble gases by sputter-ion pumps", *Vacuum* **122** (2015) 218-221.

Cathodes	Mean atomic mass A [u]
Al-Al	26.98
Ti-Ti	47.88
Cu-Ti	55.71
Cu-Cu	63.55
Nb-Cu	78.23
Zr-Zr	91.22
Nb-Nb	92.91
Ta-Ti	114.42
Ta-Zr	136.09
Ta-Ta	180.95

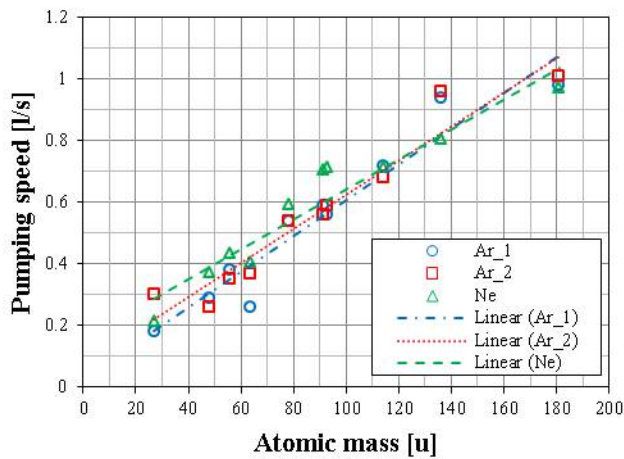**Table 6-12 – Mean atomic mass of each pair of tested bulk cathodes.**

Figure 6-17 – Linear dependence of Ar and Ne pumping speed S after saturation on the mean atomic mass A of the cathodes. Two different sets of Ar data are shown.

Quite unexpectedly, Ar pumping speed after saturation turns out to be linearly dependent on the mean atomic mass A of the cathodes (cf. Ar_1 in Figure 6-17). The parameters of this linear fit are reported in Table 6-13: the coefficient of determination $R^2=0.9275$ denotes that a linear dependence of S upon A fits well the experimental data. The second series of Ar sorptions (Ar_2 in Figure 6-17)—made with each SIP at the end of the testing sequence after the pumping of other

gases—confirms this trend: the slope and the coefficient R^2 of this new series of data are substantially equivalent to the previous ones (cf. Table 6-13).

Gas	Fit equation	m	q	R^2
Ar_1	S=m·A+q	0.0058	0.0271	0.9275
Ar_2	S=m·A+q	0.0055	0.0700	0.9346
Ne	S=m·A+q	0.0049	0.1563	0.9202
Ar_1	S=m·R+q	0.2325	0.0271	0.9275
Ar_2	S=m·R+q	0.2214	0.0700	0.9346
Ne	S=m·R+q	0.0984	0.1563	0.9202
All	S=m·ln(R)+q	0.3320	0.2665	0.6957

Table 6-13 – Fit parameters of the pumping speed S linear dependences on A and R for Ar and Ne, as well as of the logarithmic dependence on R for the whole set of data. The coefficient of determination R^2 of each fit is also shown.

As for Ne, a linear correlation with A is also easily recognisable (Figure 6-17), again with a very similar angular coefficient and a comparable R^2 value (Table 6-13). This confirms that the same mechanisms regulating the pumping of Ar by a SIP are also decisive when dealing with Ne.

As R is simply given by A over the atomic mass of the gas, Ar and Ne pumping speeds after saturation are linearly dependent also on R, with the same good R^2 values (Table 6-13). In this case, however, the trend line of Ne has a different angular coefficient (Figure 6-18a).

Since S depends linearly on R, this automatically rules out a logarithmic dependence on the same variable: if all the measured Ar and Ne pumping speeds are plotted together as a function of R (Figure 6-18b), a logarithmic fit gives a substantially lower coefficient of determination R^2, which is comparable to the one resulting from Baker and Laurenson's data (0.6957 *vs.* 0.7653, respectively). This is probably due to the fact that their set of data was too fragmentary to ascertain whether a logarithmic dependence of S on R could give the best fit or not. As a matter of fact, they examined only three pairs of cathode materials: Ti-Ti, Al-Ta and Ti-Ta. Moreover, the fact that pumping speed was simply measured after 4 h of pumping at $2 \cdot 10^{-6}$ Torr, without explicitly mentioning saturation, suggests that the new data might be more reliable. In the present study, depending on the cathodes, saturation was reached even after several hours of pumping.
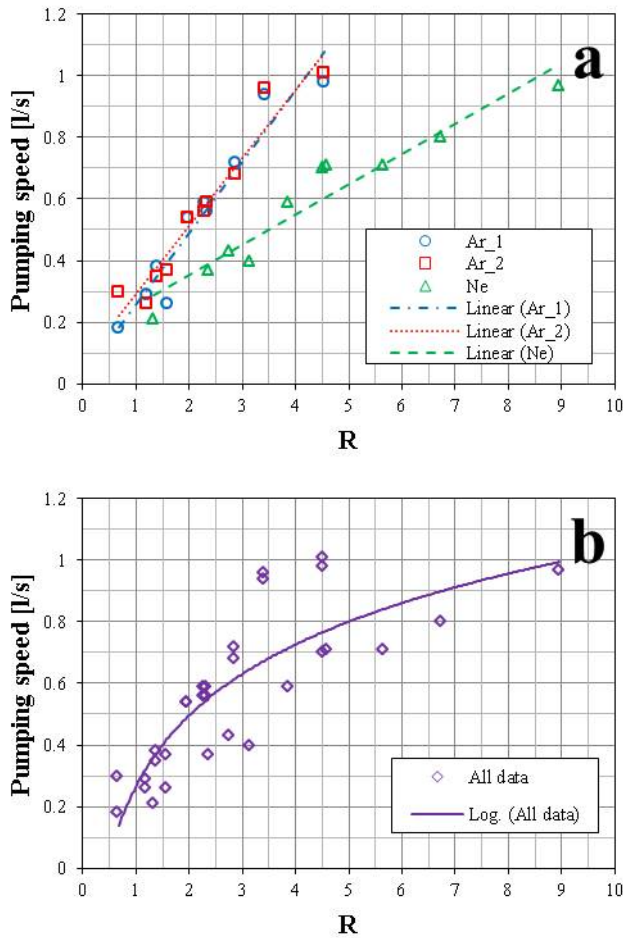
Figure 6-18 – a) Linear dependence of Ar and Ne pumping speed after saturation S on the ratio R. Two different sets of Ar data are shown. b) Logarithmic fit of all the Ar and Ne pumping speed values as a function of R.

The pumping of He, on the other side, cannot be included in this scheme: apart from the recurring difficulties in reaching saturation, which requires large quantities of He and very long sorption tests, there is no evidence of a clear dependence of He pumping speed after saturation on the mean atomic mass of the cathodes. This is probably ascribable to the intrinsic characteristics of He molecules. Compared to heavier noble gases, He atoms have a very low sputter yield and very small atomic mass and dimensions; these factors determine the ability of He ions to diffuse inside the cathodes, which thus represent the primary

location for He pumping [1]. The role of the energetic neutrals is conversely limited, as proven by the fact that using a noble-diode SIP instead of a diode one does not give any significant advantage in terms of He pumping speed [3].

A precise identification of the reasons behind the linear dependence of Ar and Ne pumping speeds on A is not trivial. The functioning of a SIP involves several competing chemical and physical effects and its overall pumping speed is thus dictated by the balance between ions adsorbed at the electrodes and released from them. In the specific case of noble gases, the implantation of ions in the cathodes and neutrals elsewhere is opposed to their thermally-induced release and, primarily, to the re-emission of ions from the cathodes induced by sputtering [8]. As thermal release is mostly important for He, whose pumping speed does not abide by the linear dependence on the cathode mean atomic mass, its influence on the establishment of a linear dependence should be negligible compared to the other concurrent phenomena. A decisive role is presumably played by the reflection and trapping of neutrals, whose contribution to the overall pumping speed becomes more important in the presence of heavier cathodes. The high-energy neutrals theory describes the fraction of energy retained by neutrals as a function of the ratio R [9]; however, this relationship is not linear. Moreover, as Ar and Ne pumping speeds after saturation have the same slope and are well superimposable when plotted against A, it follows that the atomic mass of the noble gas being pumped has a small influence on the pumping speed of the SIP, whose performance for Ar and Ne thus seems to be determined only by the choice of the cathode materials.

6.4.2. HUP cathodes

Gas	Cathodes	Fit equation	m	q	R^2
Ar_1	HUP	S=m·A+q	0.0107	-0.2824	0.8339
	Bulk	*S=m·A+q*	*0.0058*	*0.0271*	*0.9275*
Ar_2	HUP	S=m·A+q	0.0105	-0.2566	0.9598
	Bulk	*S=m·A+q*	*0.0055*	*0.0700*	*0.9346*

Table 6-14 – Fit parameters m and q of the pumping speed S linear dependence on the mean cathode atomic mass A of HUP and bulk cathodes during tests Ar_1 and Ar_2. The coefficient of determination R^2 of each fit is also shown.

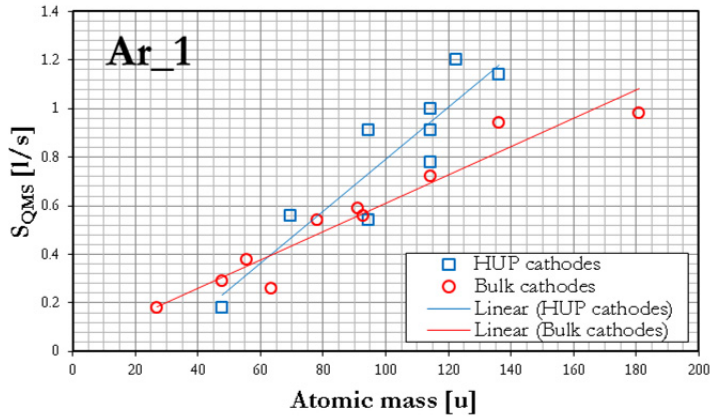An analogous reasoning can be made also about the pumping of noble gases by HUP cathodes.

Figure 6-19 – Pumping speed after saturation S$_{QMS}$ during tests Ar_1 of HUP and bulk cathodes as a function of the mean cathode atomic mass A.

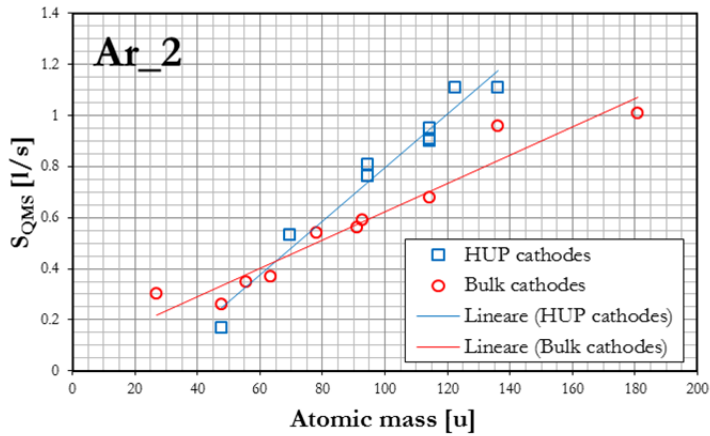**Figure 6-20 – Pumping speed after saturation S$_{QMS}$ during tests Ar_2 of HUP and bulk cathodes as a function of the mean cathode atomic mass A.**

Again, by taking into account Ar pumping speed S after saturation, a linear dependence on the mean atomic mass A is clearly recognisable. This seems to be true for both Ar_1 and Ar_2 series of tests (Figure 6-19 and Figure 6-20), whose

parameters m and q of the linear fit are almost identical, as in the previous case of bulk cathodes (Table 6-14). This confirms that, once saturation for a certain gas is reached, pumping speed of a SIP for that specific gas remains constant and becomes well-reproducible. Quite surprisingly, however, the angular coefficient m of HUP cathodes is larger compared to the case of bulk cathode plates (cf. Table 6-14) and thus, for a given A value, the pumping speed of HUP cathodes is in most cases higher than that of bulk ones. This trend seems to be true, in particular, for large values of A; the linear trend lines of these two sets of data intersect around A=65 u.

Gas	Cathodes	Fit equation	m	q	R^2
	HUP (1100 °C)	S=m·A+q	0.0090	-0.0192	0.8589
Ar_1	HUP (800 °C)	S=m·A+q	0.0120	-0.5957	1.0000
	Bulk	*S=m·A+q*	*0.0058*	*0.0271*	*0.9275*
	HUP (1100 °C)	S=m·A+q	0.0090	-0.0767	0.9454
Ar_2	HUP (800 °C)	S=m·A+q	0.0075	0.0502	1.0000
	Bulk	*S=m·A+q*	*0.0055*	*0.0700*	*0.9346*

Table 6-15 – Fit parameters m and q of the pumping speed S linear dependence on the mean cathode atomic mass A of HUP and bulk cathodes during tests Ar_1 and Ar_2. The coefficient of determination R^2 of each fit is also shown. HUP cathodes are divided according to their annealing temperature.

Further details can be obtained if HUP cathodes are distinguished according to their annealing thermal treatment; in this case, the performance improvement given by the adoption of HUP cathodes seems also to be larger for cathodes annealed at a higher temperature (cf. Figure 6-21 and Figure 6-22).

For both Ar_1 and Ar_2 tests, Ti HUP cathodes annealed at 600 °C gave the worst results and their pumping speed was even lower than that of conventional Ti bulk cathodes with the same atomic mass.

Cathodes annealed at 800 °C (*i.e.*, $Ta_{35}Ti_{65}\_2$ and $Ta_{50}Ti_{50}\_2$) were an exception because, unlike all the others, there was a large discrepancy (cf. Table 6-15) between pumping speeds measured during Ar_1 (0.54 l/s and 0.78 l/s, respectively) and Ar_2 (0.76 l/s and 0.91 l/s, respectively). Pumping speeds measured during Ar_1 were therefore comparable to those of bulk cathodes and lower than those of HUP cathodes with the same atomic mass annealed at 1100

°C. On the other side, the values measured during Ar_2 tests were in line with those of HUP cathodes annealed at higher temperature.
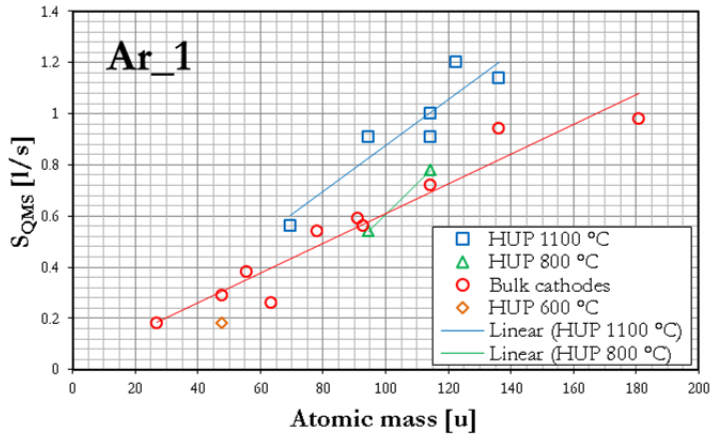

Figure 6-21 – Pumping speed after saturation S$_{QMS}$ during tests Ar_1 of HUP and bulk cathodes as a function of the mean cathode atomic mass A. HUP cathodes are divided according to their annealing temperature.
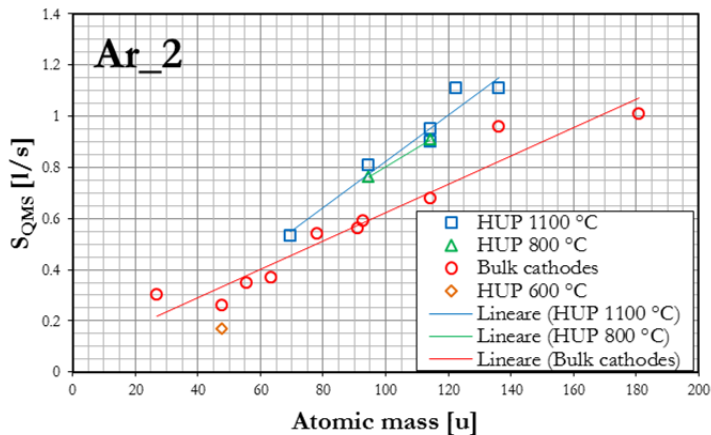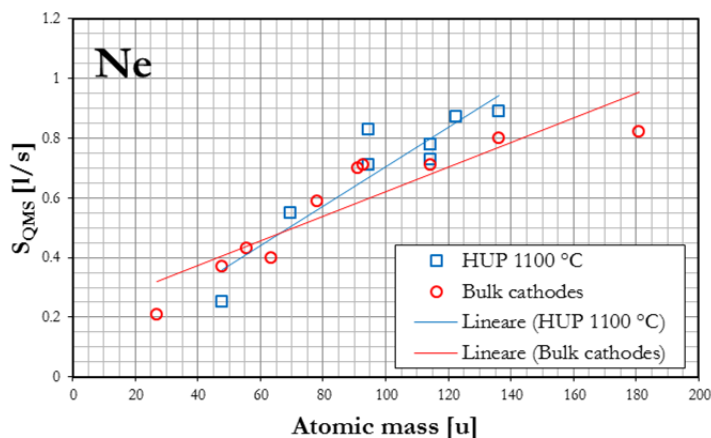

Figure 6-22 – Pumping speed after saturation S$_{QMS}$ during tests Ar_2 of HUP and bulk cathodes as a function of the mean cathode atomic mass A. HUP cathodes are divided according to their annealing temperature.

This seems to prove that the Ar pumping speed of these two pairs of cathodes annealed at 800 °C has been somehow influenced by the prolonged sorption of Ar and other gases during the testing sequence, which might have modified in some way the cathode surface through for instance sputtering; further hints about this topic could be given by the physicochemical analyses (FESEM/EDX and XRD) of the cathodes resumed in Chapter 7.

Cathodes	Fit equation	m	q	R²
HUP (1100 °C)	S=m·A+q	0.0046	0.2864	0.7609
HUP (800 °C)	S=m·A+q	0.0010	0.6154	1.0000
HUP (all together)	S=m·A+q	0.0066	0.0421	0.8403
Bulk	*S=m·A+q*	*0.0041*	*0.2067*	*0.8227*

Table 6-16 – Fit parameters m and q of the pumping speed S linear dependence on the mean cathode atomic mass A of HUP and bulk cathodes during test Ne_1. The coefficient of determination R² of each fit is also shown. HUP cathodes are divided according to their annealing temperature.
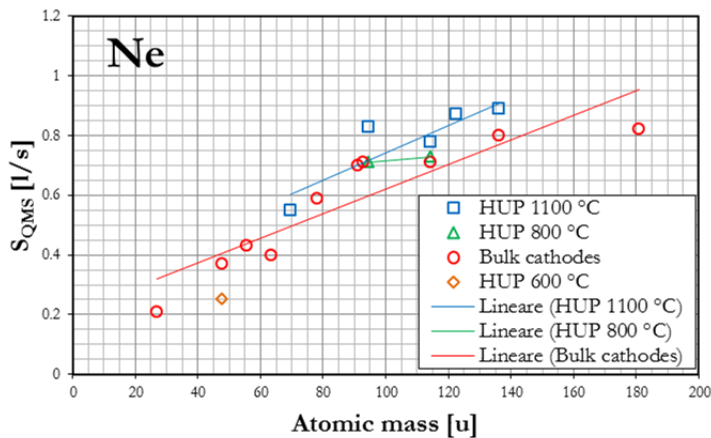

Figure 6-23 – Pumping speed after saturation S_{QMS} during tests Ne_1 of HUP and bulk cathodes as a function of the mean cathode atomic mass A.

As for Ne, the observed trend follows closely the one of Ar, confirming once again that their sorption by SIPs evidently obeys the same mechanisms. Pumping speed after saturation linearly depends with a good approximation on the

mean atomic mass of the cathodes (Figure 6-23). Again, the angular coefficient m of this linear fit is larger than that of bulk cathodes (Table 6-16); however, m=0.0066 obtained with HUP cathodes during Ne tests is not so close to the angular coefficients observed during Ar_1 and Ar_2 tests with the same cathodes (0.0107 and 0.0105, respectively). The angular coefficients of bulk cathodes, instead, were much more similar, regardless of the gas being pumped: 0.0041 for Ne and 0.0058 and 0.0055 for Ar_1 and Ar_2, respectively. Nevertheless, the fit lines of HUP and bulk cathodes in the case of Ne intersect again around A=65 u, as for Ar.

Generally speaking, in the case of Ne the difference between bulk and HUP cathodes are less pronounced, although the higher performances of these latter are still noticeable. This aspect is confirmed also by distinguishing the HUP cathodes on the basis of their annealing temperature: there is little if any difference between bulk and HUP annealed at 800 °C but also between bulk and HUP annealed at 1100 °C, whose linear fits have quite the same angular coefficients. Ti HUP cathodes annealed at 600 °C were also in this case the worst performing ones. In light of these results, it seems that the beneficial effects given by the use of HUP cathodes in the pumping of Ar are somehow reduced when considering Ne; a possible involvement of sputtering and cathode surface modifications caused by this latter are discussed in Chapter 7.

Figure 6-24 – Pumping speed after saturation S_{QMS} during tests Ne_1 of HUP and bulk cathodes as a function of the mean cathode atomic mass A. HUP cathodes are divided according to their annealing temperature.

6.4.3. Kr sorption tests

Kr sorption tests were not made with all the SIP configurations under investigation, thus it is still not possible to draw a clear picture about the pumping of this gas as a function of the adopted cathode materials. Nevertheless, some observations about the pumping of this gas are feasible.

Only two pairs of bulk cathodes (Ti-Ti and Ta-Zr, Figure 6-25a) and four pairs of HUP cathodes ($Zr_{50}Ti_{50}$, $Ta_{50}Ti_{50}\_3$, $Ta_{35}Zr_{65}$, and $Ta_{50}Zr_{50}$, Figure 6-25b) have been characterised for Kr through the usual sorption tests at $P_m=5\cdot10^{-5}$ Torr. Tests on Ti-Ti cathodes resulted in a saturation pumping speed S_{QMS} equal to 0.17 l/s only. Pumping speed of Ta-Zr cathodes progressively decreased and at the end it was even lower than 0.1 l/s.

TaZr HUP cathodes reached instead the highest pumping speeds; $Ta_{35}Zr_{65}$ and $Ta_{50}Zr_{50}$ cathodes were almost equivalent (0.59 l/s and 0.57 l/s, respectively), in spite of their different atomic masses. $Ta_{50}Ti_{50}\_3$ and $Zr_{50}Ti_{50}$ gave lower pumping speeds (0.49 l/s and 0.33 l/s, respectively), apparently in accordance with the linear dependence typical of Ar and Ne pumping. For a linear dependence of the type S=mA+q, the angular coefficient m of these HUP cathodes (all annealed at 1100 °C) was 0.0039 ($R^2=0.9207$), lower than m=0.0090 for Ar and similar to m=0.0046 for Ne.
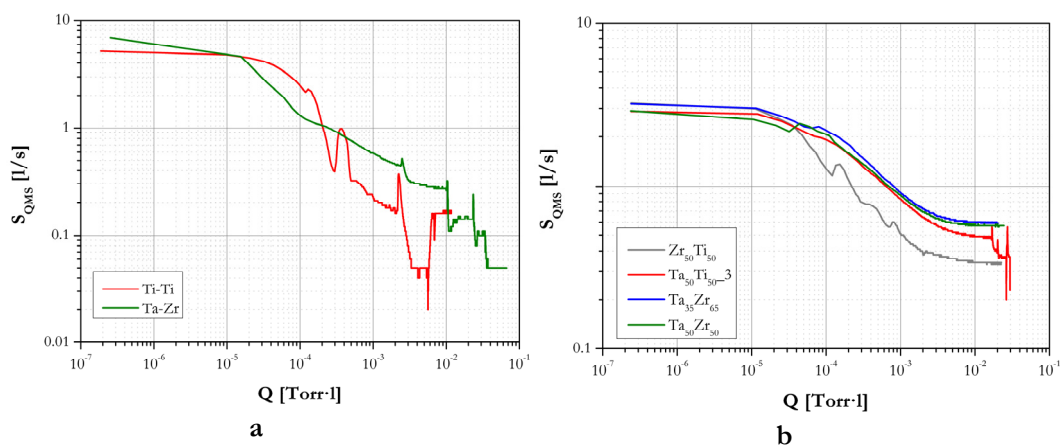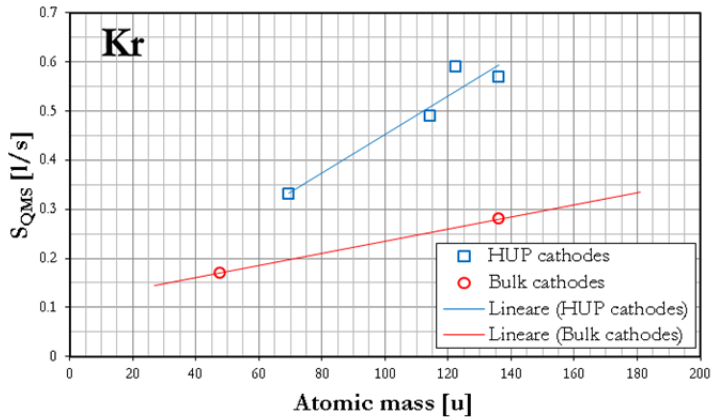

Figure 6-25 – S_{QMS} measured during Kr_1 sorption tests at $P_m=5\cdot10^{-5}$ Torr with different pairs of a) bulk and b) HUP cathodes.

Figure 6-26 – Pumping speed after saturation S$_{QMS}$ during tests Kr_1 of some HUP and bulk cathodes as a function of the mean cathode atomic mass A.

However, these data are still too fragmentary and other Kr tests should be possibly made in the future in order to ascertain the effective compliance of Kr pumping to the same rules valid for Ar and Ne. In addition, Xe sorption tests might help in confirming the validity of this model for all the noble gases other than He.

6.5. Observations about the sorption of CH$_4$

As CH$_4$ pumping mechanisms of SIPs completely differ from those ensuring the sorption of noble gases, all the considerations made in Section 6.4 about the best-performing cathode configurations are clearly no more valid when considering CH$_4$.

CH$_4$ sorption tests on bulk cathode plates (cf. Section 6.2.3) showed that Nb-Nb and Zr-Zr, followed by Ti-Ti, were the best configurations, both in terms of S and S$_{QMS}$. On the contrary, Cu-Cu were by far the worst ones, both considering S and S$_{QMS}$. Al-Al and Ta-Ta cathodes were placed in-between, Al-Al being very poor in terms of S but almost equal to Ti-Ti when considering S$_{QMS}$. Nb-Cu and Cu-Ti cathodes gave good results despite the presence of a Cu cathode in each of them, while Ta-Zr were in line with Ta-Ta ones.
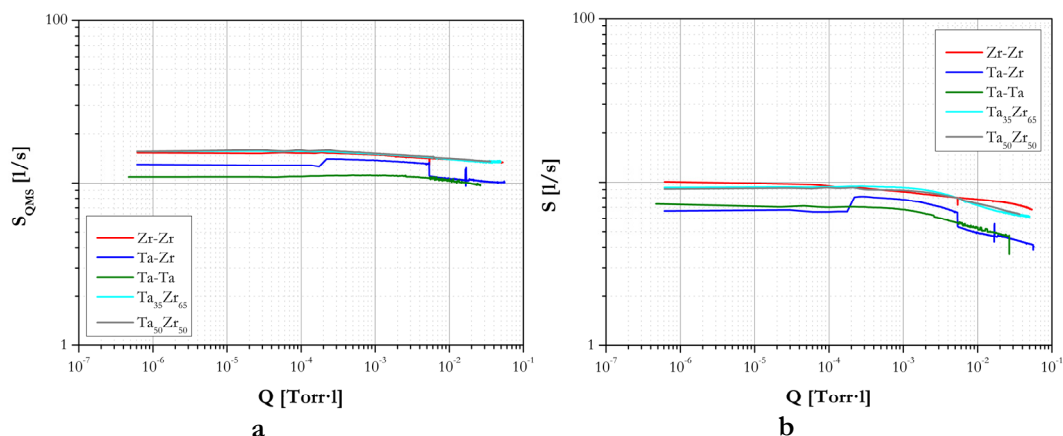
Figure 6-27 – a) S_{QMS} and b) S during CH_4 sorption tests of bulk and HUP cathodes comprising Ta and Zr.

On the other side, tests on HUP cathodes (cf. Section 6.3.3) revealed that all the configurations under exam were more or less equivalent to the conventional Ti-Ti diode configuration in terms of S_{QMS} (Table 6-10). Small differences were present among HUP cathodes also in terms of S; Ti HUP cathodes—which had been the worst for Ar and Ne—were indeed the best when considering the overall pumping speed S during CH_4 pumping.

Figure 6-27a shows that Zr-Zr, $Ta_{35}Zr_{65}$ and $Ta_{50}Zr_{50}$ cathodes were perfectly equivalent in terms of S_{QMS} during CH_4 pumping, while Ta-Zr and Ta-Ta where very similar but lower than the other three. On one hand, as already mentioned, the presence of a single Ta cathode in the Ta-Zr layout was sufficient to align it to Ta-Ta instead of Zr-Zr. On the other side, the presence of Ta (35 at.% or 50 at.%)—homogeneously dispersed inside TaZr HUP cathodes—did not affect their performance with respect to Zr-Zr ones. If the overall pumping speed S is taken into account (Figure 6-27b), the same trends are confirmed; S of Zr-Zr cathodes was in this case slightly higher than $Ta_{35}Zr_{65}$ and $Ta_{50}Zr_{50}$, consistently with the better getter properties of Zr compared to Ta.

When considering combinations of Ta and Ti (Figure 6-28a-b), the performances of $Ta_{35}Ti_{65}$ HUP cathodes were slightly higher compared to $Ta_{50}Ti_{50}$ ones containing more Ta. The scenario previously traced for Ta and Zr was in this case not fully respected, since the noble-diode SIP (that is, Ta-Ti) was better than TaTi HUP cathodes in terms of S_{QMS}, instead of being equivalent to Ta-Ta ones, which gave the lowest value. When taking into account S, the noble-diode SIP was

instead equivalent to the TaTi HUP configurations but still far better than Ta-Ta. The noble-diode SIP was also substantially equivalent to Ti HUP cathodes, both in terms of S and S_{QMS}. However, most of CH_4 tests on noble-diode SIPs were made at $P_m=2\cdot10^{-6}$ Torr, according to the initially-adopted testing sequence. One noble-diode SIP was later tested only once at $P_m=5\cdot10^{-5}$ Torr, after a new series of characterisations; the noble-diode curves in Figure 6-28a-b still need to be confirmed by further tests made in the same conditions on a new SIP.

Finally, $Zr_{50}Ti_{50}$ were perfectly equivalent to Zr-Zr ones and better than Ti-Ti ones; in order to fully confirm the proposed scenario, a hypothetical pair of Zr-Ti bulk cathodes, if tested, would have to be more similar to Ti-Ti than Zr-Zr.
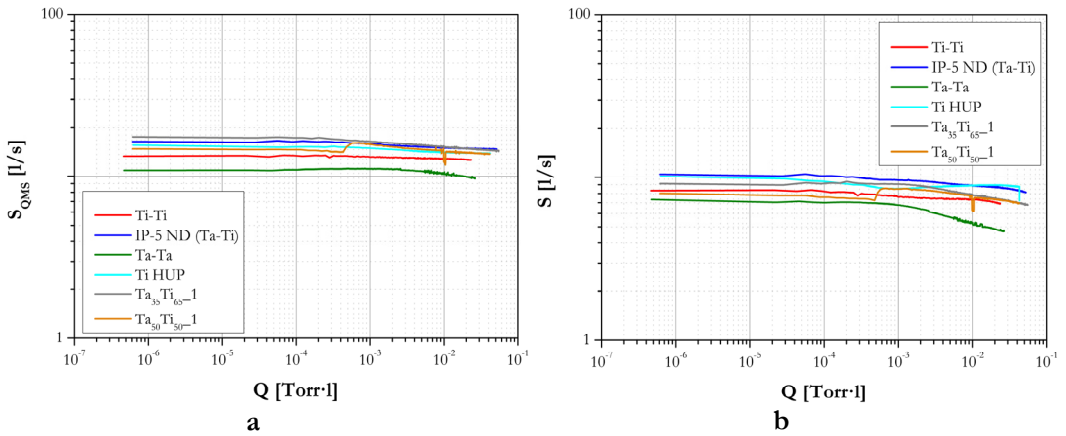
Figure 6-28 – a) S_{QMS} and b) S during CH_4 sorption tests of bulk and HUP cathodes comprising Ta and Ti.

In conclusion, these results indicate that the mean atomic mass of the cathodes plays no role in the sorption of CH_4. The presence of a cathode material with good getter properties (*viz.*, Zr, Ti and Nb) seems conversely to be decisive. This is of course true when considering S—which takes into account H_2, a getterable gas—but also S_{QMS}: a good getter material has likely also a catalytic effect in the dissociation of CH_4 molecules. It is worth noting that HUP cathodes allow to keep the good performance of one of their components (*e.g.*, Zr), even if the other one (*e.g.*, Ta) is low-performing. On the other side, when coupling two separate bulk cathode plates, the overall pumping performances are aligned to those of the worst component. In view of the coupling with NEG, a high H_2 pumping speed is not essential; a material able to efficiently crack CH_4 molecules

would be instead crucial in order to increase the performance of a SIP. In this framework, both Ti and Zr are good options for an optimised CH_4 pumping; Zr should be however preferred because, thanks to its higher atomic mass, it would provide higher pumping speeds than Ti when pumping noble gases. From this point of view, TaZr HUP cathodes might be the best options if both Ar pumping and CH_4 sorption need to be optimised, thanks to their high atomic mass and to the getter properties of Zr.

6.6. Peculiar behaviour of helium

As already mentioned in Chapter 2, the pumping mechanism of SIPs for He differs from those for heavier noble gases and, in some way, it resembles the one for H_2. This is mainly due to the very small atomic mass of He (4.0026 u) compared to other noble gases.

This difference is reflected by the inability to identify a clear dependence of He pumping speed on the mean cathode atomic mass, as for heavier noble gases (cf. Sections 6.4.1 and 6.4.2). He sorption curves of bulk and HUP cathodes are shown in the next Section 6.6.1, followed by the discussion of some important issues and experimental findings encountered during He pumping tests.

6.6.1. Results of He sorption tests

The sequence of sorption tests adopted for cathode characterisations on IP-LAB initially included an ASTM F798-97 He sorption at $P_g=3\cdot10^{-6}$ Torr (cf. Table 6-4).

He sorption curves made at $P_g=3\cdot10^{-6}$ Torr with several pairs of bulk cathode plates are shown in Figure 6-29a. The performance of these cathodes was clearly not dictated by their mean atomic mass, as for Ne, Ar and Kr. Saturation of Ti-Ti cathodes corresponded to 0.45 l/s; however, previous tests on another diode SIP had evidenced a saturation pumping speed equal to 0.27 l/s. Cu-Cu cathodes were unexpectedly very good in terms of saturation pumping speed (0.64 l/s) and comparable to Nb-Cu ones. The apparent good performance of Cu in He pumping seemed to be confirmed also by Cu-Ti cathodes, which gave again the

same pumping speed. Saturation pumping speed of Nb-Nb was instead equal to 0.43 l/s. Saturation was instead not reached with Al-Al and Ta-Ta cathodes, but their trend seemed to be approximately the same of the previous examples, so that a saturation pumping speed of the same order of magnitude might be presumptively supposed also for them.
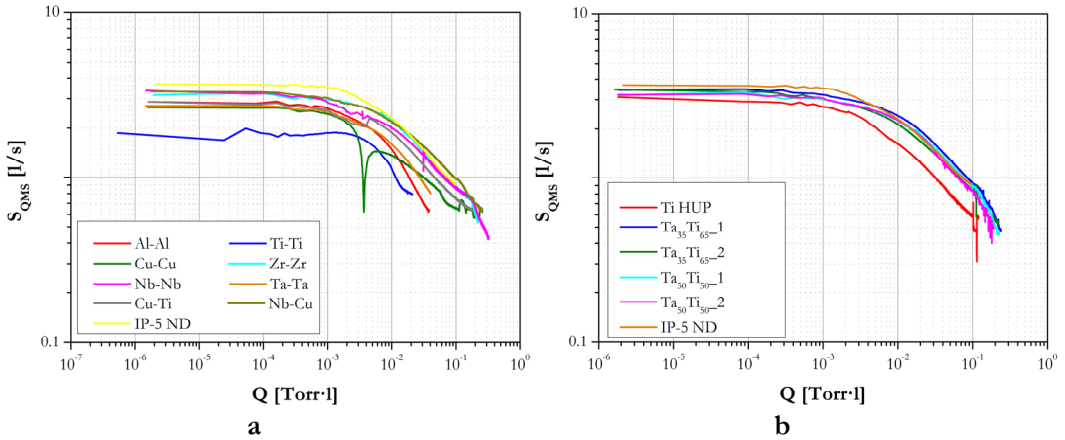

Figure 6-29 – Sorption curves of a) bulk cathodes and b) HUP cathodes.

As for HUP cathodes, results are missing for $Zr_{50}Ti_{50}$, $Ta_{35}Zr_{65}$ and $Ta_{50}Zr_{50}$. Two $Ta_{35}Ti_{65}$ and two $Ta_{50}Ti_{50}$ pairs were tested: their curves were all perfectly equivalent and superimposable to the curve obtained with the noble-diode SIP. Their saturation pumping speeds were all comprised between 0.45 l/s and 0.52 l/s. On the other side, the curve of Ti HUP cathodes ran along lower values but its final saturation pumping speed was again comparable to the others (0.58 l/s).

Generally speaking, the attainment of saturation conditions during He pumping was difficult and required large quantities of gas compared to the other gas species under test. In most cases, pumping speed clearly tended towards a saturation value without however reaching it completely. As explained in the following, this might be due to the peculiar mechanisms for He pumping in SIPs and to the continuous balance between He molecules adsorbed into the pump and desorbed from it.

6.6.2. **Memory effects: He removal from IP-LAB**

On average, the quantity of He pumped during each ASTM F798-97 sorption test at $P_g=3\cdot10^{-6}$ Torr was equal to about $2\cdot10^{-1}$ Torr·l.
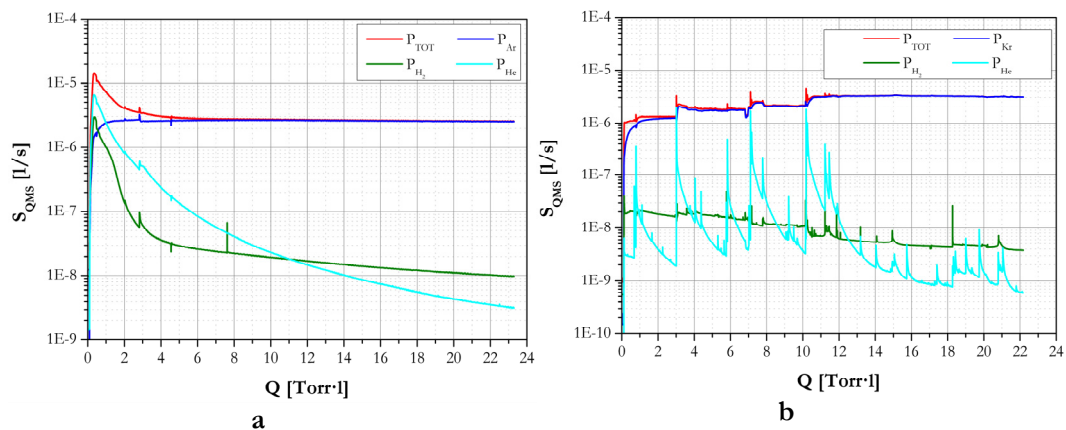
Figure 6-30 – He regurgitation stimulated by the simultaneous sorption of a) Ar and b) Kr.

This gas was probably mainly sorbed by the electrodes, which were each time replaced by new ones. However, a substantial fraction of it was undoubtedly pumped also in other inner surfaces of IP-LAB. This is confirmed by the fact that, as the number of tested cathode materials progressed, it progressively became more and more difficult to reduce He residual pressure through purging after each sorption of this gas. While He partial pressure easily decreased during test Ar_2 of the first pairs of Ti cathodes tested (Figure 6-30a), He regurgitation was much more evident during test Kr_1 of Ta-Zr cathodes, resulting in a continuous series of dramatic He peaks (Figure 6-30b).

Kr, due to its high atomic mass, probably promoted a very effective sputtering of the SIP elements; however, similar peaks were observed also during Ar, N_2, Ne and CH_4 tests on the same cathodes. As Ta-Zr cathodes did not undergo a He sorption test, these peaks were entirely ascribable to sputtering and release of He not from the electrodes but from the other inner surfaces of the SIP.

In order to face this problem, IP-LAB was disassembled when the tests on Ta-Zr HUP cathodes were over. The inside of the pump was treated with a diluted solution of HCl and HF, which caused the exfoliation of the upper superimposed

layers of sputtered metals, where He atoms were presumably trapped. Afterwards, the pump was baked in vacuo at 350 °C for 24 hours, in order to further promote the diffusion and release of He. IP-LAB was then reinstalled on the test-bench and cathode characterisations resumed. As a result of these treatments, He residual pressure during SIP functioning was largely decreased and He peaks of such intensity did not arise anymore, confirming the important contribution to He pumping given by the inner surfaces of the SIP.

6.6.3.   Memory effects: He regurgitation and purging

Purging techniques contemplating the use of different gases were also brought into focus and the effectiveness of Ar and O_2 purging—after the sorption of sizeable amounts of He—was investigated. Data presented in this section, in particular, were summarised in a technical poster presented at the *19th International Vacuum Congress* (IVC-19), which was held in September 2013 in Paris.

	Gas	Test type	Set pressure [Torr]
1	He	ASTM	$Pg=3 \cdot 10^{-6}$
2	O_2	ASTM	$Pg=3 \cdot 10^{-6}$
3	He	ASTM	$Pg=3 \cdot 10^{-6}$
4	Ar	ASTM	$Pg=3 \cdot 10^{-6}$
5	O_2	ASTM	$Pg=3 \cdot 10^{-6}$

Table 6-17 – Series of He, O_2 and Ar sorption tests made on two IP-10 pumps.

Two pumps were used to perform these tests, both with a nominal N_2 pumping speed of 10 l/s: one noble-diode pump (IP-10_03 ND) and one standard-diode (IP-10_04). The adopted experimental procedure was the same for both pumps and included a series of five ASTM F798-97 tests of He, O_2 and Ar (cf. Table 6-17): a one-step purging of O_2 came after the first He sorption, while the second one was followed by a two-steps purging of Ar and then O_2.
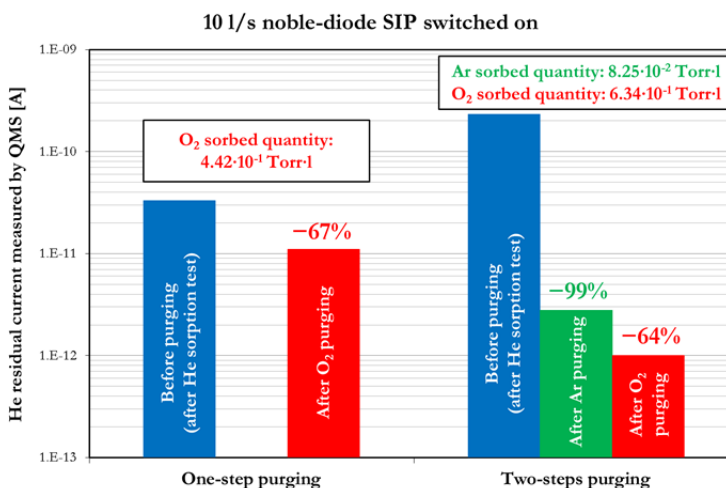
Figure 6-31 – He residual currents measured with IP-10_03 ND, in case of one-step or two-steps purging.

Every gas sorption was performed during the day, in order to have enough time for the system to recover its base pressure at the end of the test during the following night. Each morning, before the beginning of a new sorption of gas, the residual currents measured by QMS were recorded in each one of the following configurations:

- TMP pumping and SIP pumping;
- TMP pumping and SIP switched off;
- TMP isolated and SIP switched off;
- TMP isolated and SIP pumping.

Figure 6-31 summarises the variations of He residual current ($m/q=4$) measured by QMS after each sorption, with the TMP isolated and the noble-diode SIP switched on. The one-step purging consisted in the sorption of $4.42 \cdot 10^{-1}$ Torr·l of O_2, which caused a 67% reduction of the He residual current. In the two-steps process, instead, the initial sorption of only $8.25 \cdot 10^{-2}$ Torr·l of Ar resulted in a 99% current reduction; afterwards, the sorption of $6.34 \cdot 10^{-1}$ Torr·l of O_2 during the second step led to a further 64% current decrease.

Regarding the standard-diode SIP (cf. Figure 6-32), the one-step purging even resulted in a consistent increase (+242%) of He residual current after the sorption of $4.55 \cdot 10^{-1}$ Torr·l of O_2. Again, the sorption of a much smaller quantity of Ar ($2.07 \cdot 10^{-2}$ Torr·l) during the first part of the two-steps purging caused a 99%

reduction of the current, while the subsequent O_2 sorption ($4.72 \cdot 10^{-1}$ Torr·l) only resulted in a further 14% decrease.
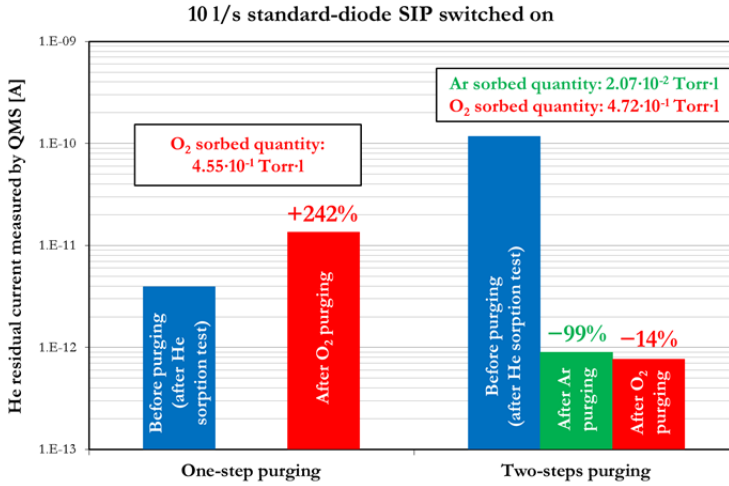

Figure 6-32 – He residual currents measured with IP-10_04, in case of one-step or two-steps purging.

IP-10_03 ND					
	Q **[Torr·l]**	**TMP on, SIP on**	**TMP on, SIP off**	**TMP off, SIP off**	**TMP off, SIP on**
1st O_2	$4.42 \cdot 10^{-1}$	-44%	-11%	-5%	-67%
1st Ar	$8.25 \cdot 10^{-2}$	-68%	-42%	-66%	-99%
2nd O_2	$6.34 \cdot 10^{-1}$	-42%	-39%	-67%	-64%

IP-10_04					
	Q **[Torr·l]**	**TMP on, SIP on**	**TMP on, SIP off**	**TMP off, SIP off**	**TMP off, SIP on**
1st O_2	$4.55 \cdot 10^{-1}$	+55%	+16%	+47%	+242%
1st Ar	$2.07 \cdot 10^{-2}$	-70%	-55%	-93%	-99%
2nd O_2	$4.72 \cdot 10^{-1}$	-7%	-9%	-31%	-14%

Table 6-18 – Percentage variations of He residual current following each stage of one-step or two-steps purging processes. Data are reported for both noble-diode (IP-10_03 ND) and standard-diode (IP-10_04) pumps.

These results thus demonstrate that, compared to O_2, Ar purging gives better results in terms of diminution of He residual current. Smaller quantities of Ar, in particular, are more effective than larger quantities of O_2: in a two-steps process made up of a Ar purging followed by a O_2 one, Ar causes a drastic reduction of the initial He residual current (-99% with both pumps), while the further decrease ascribable to O_2 is much more limited (especially with the standard-diode SIP). Furthermore, the one-step O_2 purging even led to a significant increase of He residual current during the treatment of the standard-diode pump.

Table 6-18 briefly summarises the percentage variations of He residual current measured after each purging stage in all the four possible pumping configurations (*i.e.*, with TMP and SIP alternatively switched on or off), for both the pumps under exam. Even if with some differences in the percentages involved, the trends observed in the previous figures, with TMP isolated and SIP switched on, are confirmed also in the other three pumping configurations.

6.6.4. Thermal desorption of He

The thermally-driven desorption of He during SIP functioning was also investigated. A 5 l/s diode SIP was intentionally dosed with significant quantities of He and used to make this kind of evaluation. As the SIP was not new, the first step consisted in the sorption of $8 \cdot 10^{-2}$ Torr·l of Ar, in order to purge the pump and to remove any influence of its previous sorption history. Afterwards, prior to starting the heating process, the pump was polluted with 0.1 Torr·l of He. The pump body was then heated in steps of 10 °C each, from room temperature up to 100 °C, using a heating tape. The pump has always been switched on during the test and a QMS has been used to monitor the evolution of partial pressures; for each step, it was necessary to wait until the attainment of a uniform temperature of the pump body and of stable total and partial pressure readings by the BAG and the QMS, respectively.

The ion currents measured by QMS during the progressive heating of the SIP are depicted in Figure 6-33. Mass 4 refers to He and mass 40 to Ar; masses 2 and 28 are added as reference for other residual gases. The plot shows an appreciable increase of He residual current starting from 60–70 °C; the final current measured at 100 °C was almost one order of magnitude higher than the

initial one taken at room temperature ($1.0 \cdot 10^{-12}$ A *vs.* $1.7 \cdot 10^{-13}$ A, respectively). Ar current also increased but on a much smaller scale (from $9 \cdot 10^{-14}$ A to $2 \cdot 10^{-13}$ A). H_2 residual current had a significant initial peak, in correspondence of the first heating step, and then quickly dropped to a substantially constant value comparable to He one. The total pressure measured by BAG remained in the 10^{-10} Torr range during the whole test. The fluctuations are due to the inability of the heating system to regulate and keep a perfectly-constant SIP temperature.
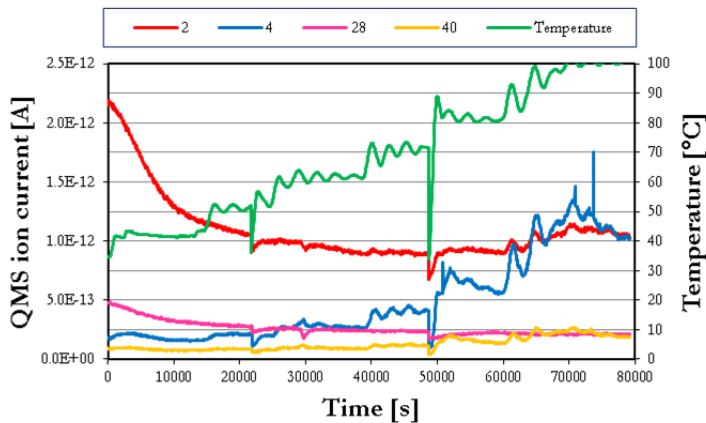
Figure 6-33 – First thermally-driven gas desorption from a SIP, after the sorption of 0.1 Torr·l of He.

At the end of the test, the system recovered the initial room-temperature conditions and the SIP underwent a second, longer He sorption (0.5 Torr·l). Afterwards, temperature was again increased step by step up to 100 °C according to the same procedure as before (Figure 6-34). It is worth noting that, already at room temperature, He residual current was considerably higher than in the previous case ($1.5 \cdot 10^{-12}$ A *vs.* $1.7 \cdot 10^{-13}$ A, respectively). At 100 °C, He current was on average equal to $7.5 \cdot 10^{-12}$ A, *i.e.* 7.5 times higher than in the first test at the same temperature. As the initial He current was in this case higher, the current increase of the second test between room temperature and 100 °C was less pronounced than before: the final He current was only five times higher, compared to an increase of one order of magnitude observed in the first test. Again, the total pressure in the system was in the 10^{-10} Torr range during the whole test.
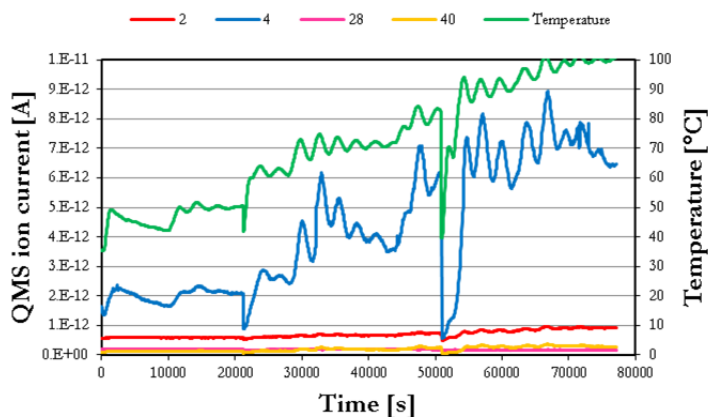
Figure 6-34 – Second thermally-driven gas desorption from a SIP, after the sorption of 0.5 Torr·l of He.

6.6.5. *General considerations about He pumping*

All these experimental findings and observations can be discussed in light of the knowledge about He pumping by SIPs and, more in general, He absorption in metals.

As already mentioned, the sorption of He by SIPs do not follow the same rules as heavier noble gases. While the pumping of these latter is given by the implantation and burial of ions in the cathodes and of high-energy neutrals elsewhere inside the pump [2], the pumping mechanism for He somehow resembles the one for H_2. In the case of He, due to its light atomic mass, there is little if any difference between the energies retained by neutrals off of Ti and Ta cathodes; this in turn results in the fact that the use of noble-diode SIPs instead of diode ones do not give any advantage in terms of He pumping speed. Moreover, it has been found that only few % of He pumped by a diode SIP is normally buried inside the anodes and the pump body, so that the most part of the sorbed gas should be implanted in the cathodes [3].

On the other side, the pumping of He seems to be mostly determined—as for H_2—by diffusion of gas molecules and ions into the cathodes. The main difference is however given by the fact that He molecules, unlike H_2 ones, cannot dissociate and form any kind of stable chemical compound (*e.g.*, hydrides) with the

cathode materials. This predominant sorption of He at the cathodes explains why He pumping speed tends to decrease as the partial pressures of heavier gases increase: the higher sputter yield of these latter enhances the desorption from the cathodes of previously-pumped He [1].

As He atoms have very small dimensions and cannot be bounded by the cathode material, desorption of previously-pumped He from both cathodes and other surfaces of a SIP—unlike heavier noble gases—can take spontaneously place even at room temperature [10]. It has been repeatedly observed that, once a significant quantity of He has been pumped by a diode SIP, He re-emission might be detected for the rest of its working life [7]. At any given time, the overall He pumping speed is thus determined by the balance between the amount of gas pumped by the SIP and the quantity of previously-pumped gas desorbed from the components of the SIP itself. This might account for the difficulty to saturate SIPs and obtain stable values of pumping speed during the previously-described sorption tests (cf. Figure 6-29). The steady pressure increase and pumping speed decrease were in this case dictated by the continuously-increasing release of previously-sorbed He; the complete saturation of the bulk cathodes through diffusion of He atoms might even lead to the zeroing of a SIP pumping speed, after which a thorough regeneration would be needed in order to restore its sorption properties [5]. The large quantities of He pumped by all the tested SIP without reaching saturation conditions are also probably dictated by the fact that significant quantities of this gas can be absorbed through diffusion in the bulk cathodes, again due to the very small molecule dimensions.

The interaction of noble gases—and in particular of He—with metals has been extensively investigated in the past due to its great relevance, among the others, in the field of metallurgy for nuclear applications. He ions can implant into the cathodes if they are accelerated by an intense electric field, as is the case of SIP cathodes. Since the solubility of He in metals is very low, it tends to be trapped at defects such as vacancies and dislocations and at the grain boundaries where, depending on the He concentration, temperature, and stress loading conditions, it may lead to the growth of voids and the precipitation of He bubbles [11]. Among the noble gases, He is the most prone to the formation of bubbles, due to its higher diffusivity compared to the others. These bubbles may have non-negligible dimensions (up to 1000 Å), whose increase is boosted by high-temperature conditions. Pressure inside bubbles might be very high and their formation might ultimately result in the so-called He embrittlement, consisting in a reduction of the

bonding strength at the grain boundaries and in the induction of intergranular fractures.

These mechanisms seem to be consistent with a number of phenomena recently observed during He pumping experiments on SIPs. The strong He peaks detected by QMS during the sorption of Kr (cf. Figure 6-30), for instance, might be caused by the simultaneous release of significant quantities of He provoked by the sudden rupture through sputtering of He bubbles enclosed inside the cathode material. In this framework, the fact that a short Ar purging was much more effective than a longer O_2 one in the lowering of He residual current—with both diode and noble-diode SIPs (cf. Figure 6-31 and Figure 6-32)—was probably ascribable to the heavier atomic mass of Ar and to its sputtering effect. Another reason for this might be that, being Ar a noble gas as He, it could implant in the cathodes only at the same locations (*viz.*, dislocations, voids, grain boundaries) already occupied by He atoms, thus replacing them, while O_2 would be preferably pumped through the formation of chemical bonds with the cathode material. The effectiveness of treating IP-LAB with a diluted solution of HCl and HF was instead probably dictated by the exfoliation of the inner surfaces of the pump, which likely facilitated the removal of the He atoms trapped inside the surface etched layer. The subsequent bake-out at 350 °C stimulated a further release of He atoms trapped more in depth, thanks to the thermally-enhanced diffusivity of the gas. Similarly, the increase in He residual current measured by QMS while heating a SIP up to 100 °C (cf. Figure 6-33 and Figure 6-34) should be ascribed to the increase in He diffusivity inside the material driven by the higher temperature.

References

[1] M. Audi and M. De Simon, "The influence of heavier gases in pumping helium and hydrogen in an ion pump," *J. Vac. Sci. Technol. A,* vol. 6, no. 3, pp. 1205-1208, 1988.

[2] R. L. Jepsen, "The physics of sputter-ion pumps," in *Proc. 4th Int. Vacuum Congr.*, London, 1968.

[3] K. M. Welch, D. J. Pate and R. J. Todd, "Pumping of helium and hydrogen by sputter-ion pumps. II. Helium pumping," *J. Vac. Sci. Technol. A,* vol. 11, no. 4, pp. 1607-1613, 1993.

[4] I. Brodie, L. T. Lamont and R. L. Jepsen, "Production of high-energy neutral atoms by scattering of ions at solid surfaces and its relation to sputtering," *Phys. Rev. Lett.,* vol. 21, no. 17, pp. 1224-1226, 1968.

[5] J. A. Vaumoron and M. P. De Biasio, "Argon and rare gas instability with heavy metal cathode Penning Pumps," *Vacuum,* vol. 20, no. 3, pp. 109-111, 1970.

[6] P. Baker and L. Laurenson, "Pumping mechanisms for the inert gases in diode Penning pumps," *J. Vac. Sci. Technol.,* vol. 9, no. 1, pp. 375-379, 1972.

[7] L. Lamont, "A novel diode sputter-ion pump," *J. Vac. Sci. Technol.,* vol. 6, no. 1, pp. 47-51, 1969.

[8] L. James and G. Carter, "Ion induced re-emission of inert gases in an ionization pump," *Trans. 9th Nat. Vac. Symp. AVS,* p. 502, 1962.

[9] C. Snoek and J. Kistemaker, "Fast ion scattering against metal surfaces," *Advances in electronics and electron physics,* vol. 21, pp. 67-99, 1966.

[10] E. Brown and J. H. Leck, "Desorption of gas in the cold cathode ionization gauge," *Brit. J. of Appl. Phys.,* vol. 6, no. 5, pp. 161-164, 1955.

[11] J. Leteurtre, V. Levy, Y. Quéré and Y. Adda, "Etude de la précipitation des gaz rares dans les métaux," in *5e Colloque de Métallurgie - Les gaz dans les métaux*, Saclay, France, 1961.

7. FESEM/EDX and XRD analyses

Along with the pumping speed characterisations discussed in Chapter 6, a series of analyses has been carried out in parallel for all the cathodes under investigation.

Field-emission scanning-electron microscopy (FESEM) was used to get information about the surface morphology and topography of each cathode, focusing in particular on the eventual modifications induced by sputtering phenomena during SIP functioning. In addition, energy-dispersive X-ray analysis (EDX) allowed to obtain qualitative and quantitative data about the chemical composition of the samples, again paying special attention to the effects of the sorption mechanisms. A Zeiss Supra 55VP field-emission scanning electron microscope, equipped with an Oxford Instruments PentaFETx3 energy-dispersive X-ray spectrometer, was employed for this purpose.

HUP cathodes were also analysed by X-ray diffraction (XRD), with the aim of studying any possible influence of both HUP sintering process and subsequent thermal treatment on their crystal structure. XRD analyses have been made on a PANalytical X'Pert Pro X-ray diffraction system equipped with a X'Celerator detector.

7.1. FESEM/EDX analyses of SIP cathodes

7.1.1. *Ti cathodes of conventional diode SIPs*

FESEM/EDX analyses of Ti cathodes of conventional diode SIPs provided some interesting results that were presented also in a paper published on the *Journal of Vacuum Science and Technology A*[1]. It is worth noting that, although surface analyses of the electrodes of SIPs had been already carried out in the past [1] [2] [3] [4], no previous study was specifically focused on the effects of pumping significant quantities of noble gas on the cathode surface.

The discussion focuses on three pairs of cathodes tested in IP-LAB, which for the sake of simplicity will be referred to in the following as α, β, and γ. Pumps α and β pumped a series of gases in the same sequence but in different quantities (cf. Table 7-1), whereas pump γ sorbed a larger quantity of Ar (*i.e.* $5.8 \cdot 10^{-1}$ Torr·l) and none of the other gases.

Each test was carried out under a constant incoming flux of gas at $P_m = 5 \cdot 10^{-5}$ Torr; N_2 tests were instead made at $P_g = 3 \cdot 10^{-6}$ Torr.

Sorption test	Gas	Gas sorbed quantity [Torr·l]	
		Pump α	Pump β
1	Ar	$1.8 \cdot 10^{-2}$	$3.4 \cdot 10^{-2}$
2	N_2	$1.2 \cdot 10^{-1}$	$2.6 \cdot 10^{-1}$
3	CH_4	$2.4 \cdot 10^{-2}$	$6.3 \cdot 10^{-2}$
4	Ne	$1.8 \cdot 10^{-2}$	$3.1 \cdot 10^{-2}$
5	He	$2.1 \cdot 10^{-2}$	$1.8 \cdot 10^{-1}$
6	Ar	$9.0 \cdot 10^{-2}$	$3.5 \cdot 10^{-2}$

Table 7-1 - Series of sorption tests performed on pumps α and β and the corresponding amounts of sorbed gas.

Upon the disassembly of the SIPs, erosion pits created by sputtering in the middle of each cathode (Figure 2, "A") and, to a lesser extent, in the middle of

---

[1] T. Porcelli, F. Siviero, G. Bongiorno, P. Michelato, C. Pagani, "Growth of microscopic cones on titanium cathodes of sputter-ion pumps driven by sorption of large argon quantities", *J. Vac. Sci. Technol. A* **33**, 05E109 (2015).

each circular area corresponding to the four anodes ("B") were easily seen with a naked eye. Darker circular lines resembling the profile of each anode were visible as well ("C"). These lines represent the areas where the material was redeposited after being sputtered.
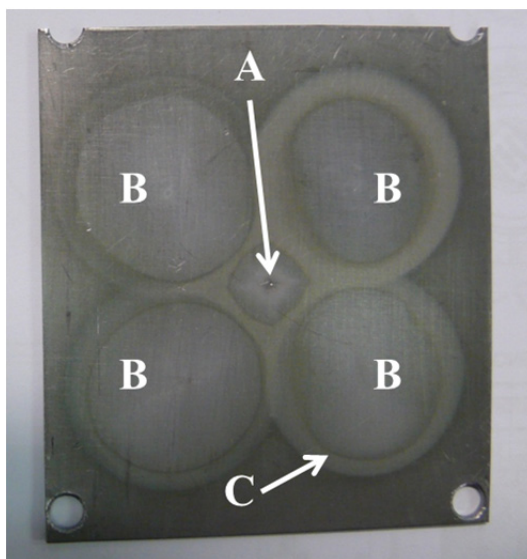
Figure 7-1 – Surface modifications seen on a Ti cathode after sorption of gas and disassembly from IP-LAB.
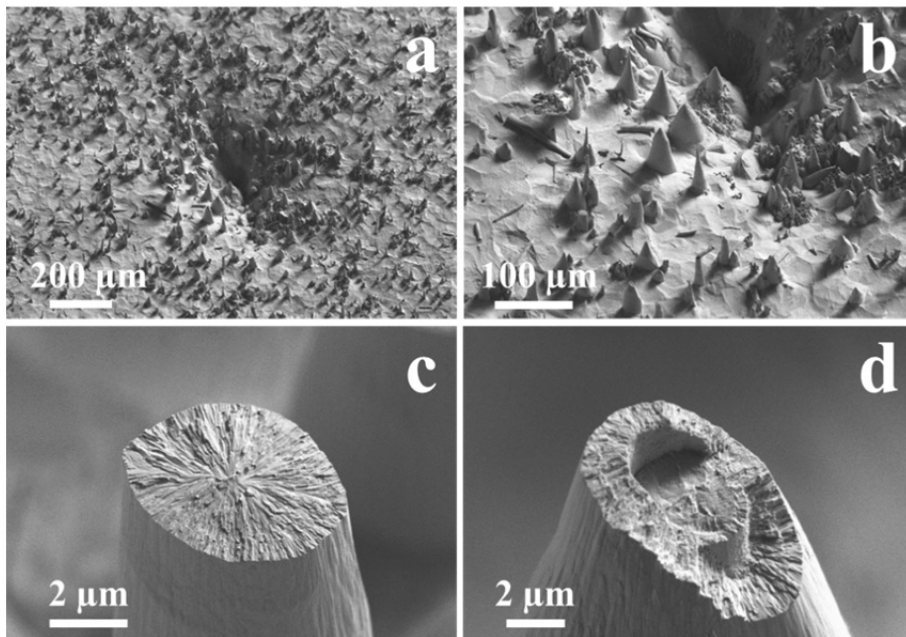
Pump a

The FESEM analyses of the first pair of Ti cathodes (pump α) revealed microscopic cones created by erosion due to ion bombardment (Figure 7-2a) around the central pit "A" (cf. Figure 7-1). The cones were instead absent in circular areas "B". The pit, measured by cutting the sample and observing the resulting section with a microscope, measured 180 μm in maximum depth. It is important to note that the cones formed in the region of the cathodes where sputtering prevails over redeposition, that is where a net erosion effect is visible.

Typical dimensions of the cones ranged between 10 μm in base diameter for smaller cones and over 20 μm for the larger ones (Figure 7-2b). Cones were randomly distributed around the central pit, apparently with a predominance of larger ones in proximity to the centre.

Columnar growth and radial symmetry were recognisable in the cross-sections of broken cones (Figure 7-2c). Smaller cones had a uniform composition, while the larger ones were comprised of two distinct concentric layers (Figure 7-2d), clearly the result of discrete and consecutive sputtering processes.

The EDX analyses showed the presence of Ar (around 3 to 4 at.% on average) in the cross-section of broken small cones (*e.g.* the ones in the middle of Figure 7-2b). The outer layer of the larger cones, which resulted from a successive deposition, exhibited a lower Ar concentration (less than 1 at.% on average), while the percentage of Ar in their inner core was equivalent to that of smaller cones. Further analyses placed the highest Ar concentration in the tips of the thin cones (up to 6 at.%). No other element (N, C, Ne) was detected inside these structures. In contrast to cones' composition, no Ar at all was found in the Ti substrate beneath them.

Figure 7-2 – Area "A" of pump α: a) microscopic cones around the central pit of a cathode; b) presence of cones of different sizes; c) radial symmetry on the cross-section of a broken cone; d) concentric layers of one of the larger cones.

It is worth noting that, since Ar is a noble gas, and thus unable to form chemical bonds with other elements, the impact of the EDX electron beam might

be sufficient to promote Ar escape from the cones during the scanning process. Therefore, the quantity of Ar trapped inside the cones might be higher than the quantities recorded.

Finally, Figure 7-2b shows the possible origin of the cones. Clusters of several small dendrites produced by the sputtering were present on the Ti surface. These are possible nucleating points for the subsequent growth of the larger cones. Afterwards, the cones may have incorporated these structures at their bases while growing. The precursor of these small clusters seems to be in turn a thin layer of fine Ti dust, which had settled on the cathodes and was clearly observable by FESEM. This dust was likely produced by sputtering.

Pump β

The FESEM/EDX analyses of pump β showed the presence of conic structures on the cathodes, though with some distinction from the cones observed in pump α.

Figure 7-3a shows the cross-section of one of the cones, which were found to have a tree-like structure with rings of different thickness and morphology, showing evidence of concentric growth (cf. Figure 7-3b).
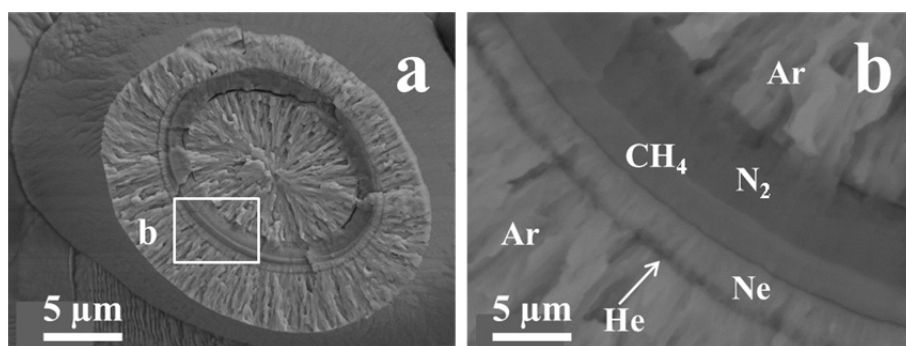
Figure 7-3 – Pump β: cross-section of a broken cone, evidencing a) tree-like growth rings and b) their thickness in an enlarged view.

The sequence of rings is in direct correlation with the pumping history of the SIP. As recorded by EDX, starting from the centre, each ring corresponds to the sorption of a different gas: Ar, N_2, CH_4, Ne, He and, again, Ar. The two

thickest layers (*i.e.* the innermost and the outermost, respectively) were clearly produced during the sorption of Ar.
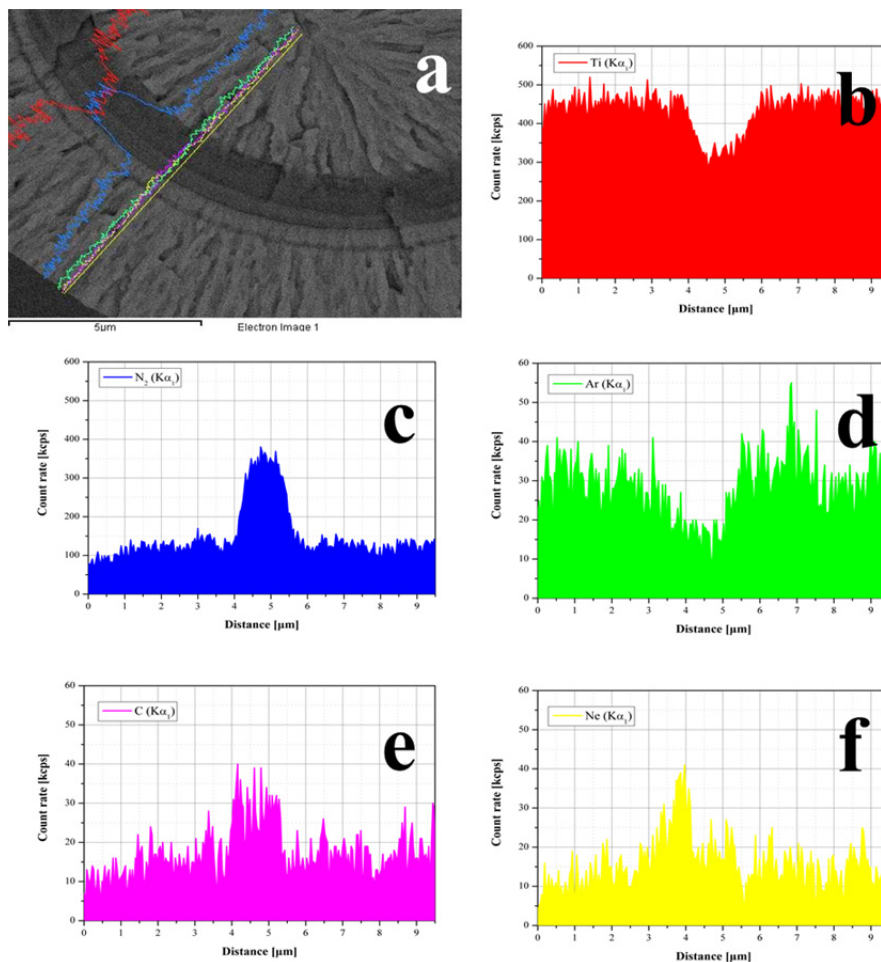

Figure 7-4 – a) EDX mapping along the cross-section radius of a broken cone, showing the contribution of the gases to each sputtered layer: b) Ti, c) N₂, d) Ar, e) C, f) Ne.

This is consistent with Ar being the most effective in the sputtering of Ti among the gases used. The morphology of these rings showed evidence of columnar growth, as did that of the smaller ring produced during the Ne sorption. The contributions of N_2 and CH_4, on the other hand, resulted in a completely different and much more dense and compact morphology (cf. Figure 7-3a). Finally,

the thinnest ring (*i.e.* the second from the outside) formed due the sorption of He. This is consistent with the fact that this light gas, possessing an atomic weight of 4 u, has the lowest sputtering effectiveness among the gases studied. Though, the quantity of sorbed He was found to be larger than that of Ar.

The EDX analyses performed on the cross-section shown in Figure 7-3 confirmed that the bands correspond to the sputtering by individual gases (cf. Figure 7-4). A mapping performed along the radius of the cross-section, over a total length of 10 μm, starting from the outer surface of the cones, detected the presence of each gas in its corresponding ring. The plots in Figure 7-4 are based on the $K\alpha_1$ x-ray emission lines. He, of course, cannot be detected through EDX analyses and its ring was thus identified by deduction.

EDX punctual analyses performed on other cone cross-sections further proved the above gas distribution. These studies also clearly demonstrated the presence of each gas in its corresponding ring. The amounts of Ar found in the innermost and outermost rings were similar to amounts found in the analyses on pump α. 3 to 5 at.% of both Ne and C was detected in their corresponding layers.

In contrast, the quantities measured for N_2 in its layer ranged from 39 to 57 at.%; this seems to indicate the formation of 1:1 stoichiometric TiN compounds due to sputtering. In fact, TiN thin films are commonly fabricated by reactive sputtering.

The origin of the two Ar-containing concentric layers in the large cones of pump α is most likely the same as in the case of pump β. The likely reason for the absence of additional layers containing N_2, CH_4, Ne and He in pump α is the smaller amounts sorbed due to the smaller gas loads (cf. Table 7-1).

Pump γ

Compared to α and β, pump γ was exposed to a much larger quantity of Ar and none of the other gases.

Compared to the previous cases, the FESEM analyses performed on pump γ revealed a marked increase in the density of the cones around the central pit of both cathodes. The shape of these structures is strongly correlated with the cones' distance from the centre of the cathode: the further they were, the thinner they were (cf. Figure 7-5a). Furthermore, the slant in all the cones was oriented along a specific direction, regardless of their shape and size (cf. Figure 7-5b). Figure 7-5c clearly shows that this progressive variation of cones' morphology, as well as their

preferential orientation, correlate with the electromagnetic field lines inside the Penning cell.

In the backscattering FESEM imaging mode, the cones appeared darker than the underlying cathode. The cones therefore have a less dense structure than the bulk or are comprised of lighter elements (cf. Figure 7-5d). The smaller cones, in particular, were darker than larger and broken ones. Moreover, cones' tips (and thus cones' inner layers) appeared brighter than the outer layers.
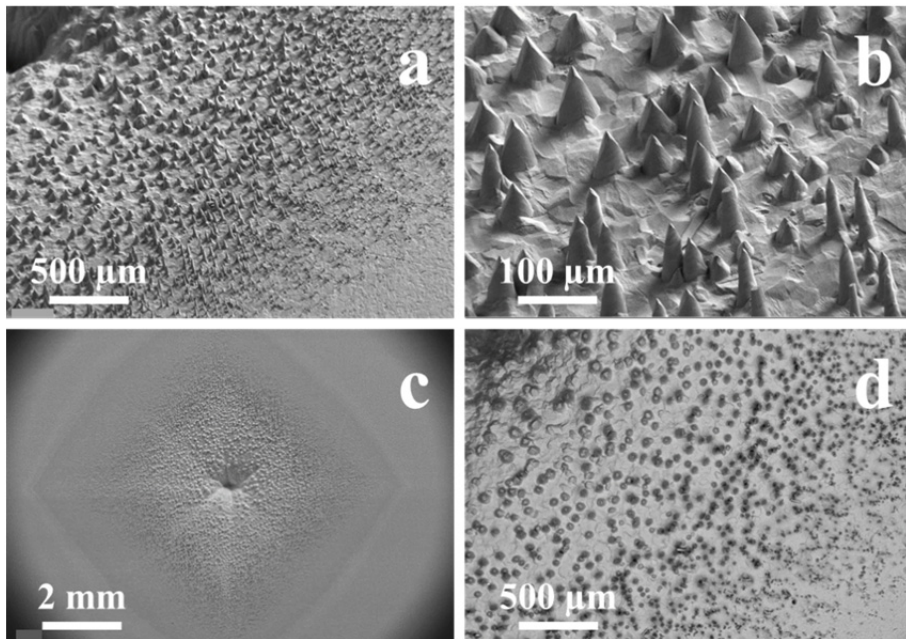
Figure 7-5 – Pump γ: a) cones' shape dependence on field lines and distance from the central pit; b) evidence of a same preferential growth orientation for cones of different shapes; c) overview of the central portion of the cathode; d) backscattering mode imaging of cones.

Unlike pumps α and β, where the cones were found only around the pit in the central "A" region, pump γ also exhibited cones in the middle of the circular areas corresponding to the insides of the Penning cells (area "B" in Figure 7-1). This feature is likely due to the higher Ar load. The density of the cones on a cathode, as well as their appearance not only in area "B" but also in "A" correlate to the quantity of Ar sorbed by pump γ.

The EDX analyses of the cones in pump γ found quantities of Ar comparable to those observed in pumps α and β (*i.e.* about 1 at.% present in the cones' cross-sections and external surfaces). The structure of these cones was uniform and without concentric layers, due to the fact that pump γ absorbed only Ar in a single sorption and did not sorb any of the other gases.

As in pumps α and β, no Ar was found in the Ti substrate beneath the cones. On the other hand, significant quantities of Ar (6 to 9 at.%) were buried in the Ti substrate in the surrounding outer area, near the net redeposition lines (Figure 7-1, "C"), where cones were not present.

Possible reasons behind the formation of cones

It is well known that, under certain conditions, a cathode surface during sputtering may become covered by patterns of microscopic cones [5]. Their formation had initially been attributed to the presence of *seed* atoms with lower sputter yield on the cathode surface. A cluster of impurities of this kind would protect the underlying material from being sputtered away. Hence, the cones would not grow on the cathode but would instead result from the excavation of the surrounding material. The seed clusters would then be found at cones' apices.

However, it was lately demonstrated that cones would actually originate from higher melting temperature impurities, that agglomerate at the cone base [6] [7]. It has also been pointed out that a minimum cathode temperature equal to approximately one third of the cathode's melting point is necessary for cone formation. Nevertheless, cones' formation has also been reported for initially-uncontaminated metal surfaces that were bombarded by high-energy gas ions, among which N^+, Ne^+, and Ar^+ have been investigated [8].

In the present study, the radial symmetry and the columnar growth observed in the cross-sections of broken cones clearly indicate that they grew on the cathodes due to the sputtering of the Ti atoms from the surrounding area; cone formation through excavation of the cathode can thus be ruled out. This is further confirmed by the results of the FESEM imaging of cathode sections cut through the central pit, that clearly show a consistent depression in the original cathode profile caused by erosion. The presence of cones, whose tips are taller than the pristine cathode surface, further confirms the growth of cones by sputtering as the predominant mechanism of cone formation.

It is worth noting, moreover, that impurities have never been detected either in the cone tips or at their bases on Ti substrate, which was clean due to sputtering. The absence of impurities is also consistent with the high grade of purity of the Ti employed in the manufacturing of the cathodes. Nucleation of cones due to seed clusters of a different metal, therefore, cannot be the reason for cone formation in this case.

As mentioned above, a thin redeposited layer of sputtered Ti acts as an initial nucleation point for cones, which grow by capture of atoms ejected from the cathode's surface. As these structures increase in height, their tips focus the electric field, promoting the implantation of the incoming gas ions into the bulk of cones, as the EDX analyses confirm. At the same time, these high-energy gas ions impinge on the cones and erode them. The Ti atoms thus sputtered away are subsequently deposited elsewhere in the surroundings, contributing to the formation and growth of other cones. The radial symmetry of the inner structure of the cones confirms their progressive growth fed by the sputtered atoms originating in the surroundings. As the SIP continues to operate, cathode material is continuously sputtered and implanted, bouncing among the growing cones. This process results in an increase of the size and the density of the cones. A few of them grow more and more to the detriment of others, the latter being incorporated into the larger ones (cf. Figure 7-2b). It is possible that the increase in the electric field on tips of the cones induces arcing phenomena that might be in turn responsible for the fracture of cones, whose tips can be found on the substrate among their truncated bases (cf. Figure 7-2b). Thin and slender cones are of course more prone to fracture than broader ones.

The presence of Ar undoubtedly plays a key role in cones' formation, as suggested by the fact that the density of cones on each pair of cathodes increased with the corresponding absorbed quantity of this gas (cf. pumps α and γ). Moreover, the longer Ar sorption test performed on pump γ yielded cones not only in the usual position "A" around the erosion pit in the middle, but also in the central part "B" of each anodic cell.

This latter observation suggests that the cones initially grow where the field (and hence sputtering and erosion) is more intense, *i.e.* in the irregular central area resulting from the intersection of the four Penning cells, as confirmed by ANSYS simulations of the field inside the pump (cf. Figure 7-6). As the Ar pumping and hence the sputtering proceed, cones also develop on other portions of the cathodes, basically in "B" areas in correspondence of the anodes.
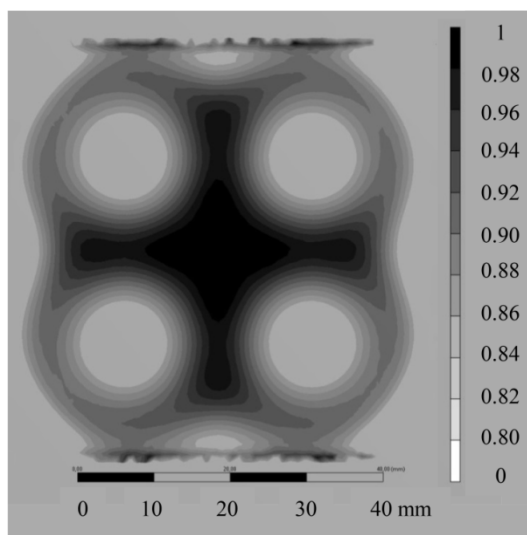
Figure 7-6 – ANSYS simulation of the electric field on the cathode surface during pump operation; the results are normalised to the highest electric-field value and expressed in terms of its percentage of the highest value. The areas with a field lower than 80% of the maximum value are not taken into account.

In light of the observations presented, a mechanism fed by Ar sputtering and driven by the applied electromagnetic field represents a plausible scenario for cone growth. This latter condition is clearly dictated by the evolution in density, morphology and orientation of cones along the electric field lines, as observed in pump γ (Figure 7-5b). The impact of the other gases (He, CH_4, Ne, and N_2) on the growth of cones, on the other hand, is limited, as the relatively thin (compared to Ar) cone layers produced during the pumping of these gases in pump β indicate. Ar, being the heaviest gas of those studied and also being the most similar in atomic mass to the substrate (40 u *vs.* 48 u, respectively), is the most effective in sputtering Ti among the gases under exam [9] and thus it seems to be the only one able to initiate the formation of cones. The thickness of the columnar-grown layers containing Ar in the cones in pump β attests to its sputtering effectiveness. The growth of the cones during Ar sputtering seems to be a specific characteristic of Ti. SIPs with tantalum cathodes have been investigated similarly to pumps α, β, and γ (cf. Section 7.1.2). The FESEM analyses revealed that the cathode surface had clearly been eroded and excavated due to sputtering (the erosion is of course much more evident on cathodes that underwent a long Ar sorption test). However, no sign of cones' formation was observed on the Ta cathodes. The

EDX studies found no Ar atoms in the erosion areas. As expected, Ar was found in the outer net-deposition areas.

In light of all these arguments, the presence of cones on the Ti cathodes but not on the Ta ones, together with the cone growth being driven by the Ar sputtering of the Ti surface, seems to correlate with the chance of Ar instability to arise when pumping large quantities of this gas with diode SIPs; as already mentioned, noble-diode SIPs mounting a Ta cathode are instead immune from this phenomenon [10] [11] [12]. The cones have been found only in regions of the Ti cathodes characterised by net erosion. There regions therefore constitute the preferential locations for the implantation of Ar atoms into the cathodes; these are areas where the ions could not be otherwise permanently buried. Moreover, no Ar was detected in the Ti substrate beneath the cones, whereas significant quantities of Ar, as expected, were found in the net-redeposition areas, where cones were not present. The Ar buried in these latter areas cannot be easily reemitted, while the cones, especially if large and densely distributed, are subject to continuous sputtering and regrowth processes, that might allow the release of Ar trapped inside them.

If the cones are assumed with base diameter and height equal on average to 30 μm and 60 μm, respectively, the volume of an average cone is of the order of 10^{-8} cm^3. Since the density of Ti is 4.5 g/cm^3 and its atomic mass 48 u, the approximate number of atoms contained in a cone comprised solely of Ti can be calculated using Avogadro constant and is equal to $8 \cdot 10^{14}$. If Ar makes up 5 at.% of the cone, the total number of Ar atoms in each cone will be therefore of the order of $4 \cdot 10^{13}$. The following assumptions and simplifications have been made in this calculation:

- 4.5 g/cm^3 is the density of bulk Ti, while the cones grown by sputtering will presumably have a less dense structure; however, this discrepancy can be considered negligible for the purpose of this study.
- As Ar atoms are dispersed inside cones made of Ti, it is reasonable to assume their total number as simply equal to 5% of the overall number of atoms calculated with Ti density.

Following these assumptions, the quantity of Ar in each cone would be equal to about $1.2 \cdot 10^{-6}$ Torr·l, since 7.5 Torr·l of gas at room temperature contains $2.45 \cdot 10^{20}$ atoms. Few thousands of cones can be roughly observed on each cathode of pump γ, which sorbed $5.8 \cdot 10^{-1}$ Torr·l of Ar. Therefore, the amount of gas trapped inside cones is of the order of a few percent of the total, the rest

having been buried in net-redeposition areas or implanted in other pump elements. Nevertheless, the contribution of the Ar trapped in the cones is still considerable, especially considering that they are piled in a small fraction of each cathode's total area. Furthermore, the quantity of Ar released during a single instability cycle by analogous SIPs under similar experimental conditions can be estimated from the observed pressure increase and is equal to about $2.0 \cdot 10^{-4}$ Torr·l. This amount corresponds to the quantity of Ar contained in approximately 170 cones. These rough calculations indicate that the quantity of Ar trapped inside cones is consistent with the likely role of cones in the development of instability phenomena, as suggested by the experimental findings.

7.1.2. Couples of bulk cathodes made of different materials

FESEM/EDX imaging was made also on couples of bulk cathode materials other than Ti-Ti, *viz.*, Al-Al, Cu-Cu, Zr-Zr, Nb-Nb, Ta-Ta, Cu-Ti, Nb-Cu, and Ta-Zr. A brief summary of the most significant observation is given below for each of these couplings.

Al-Al cathodes
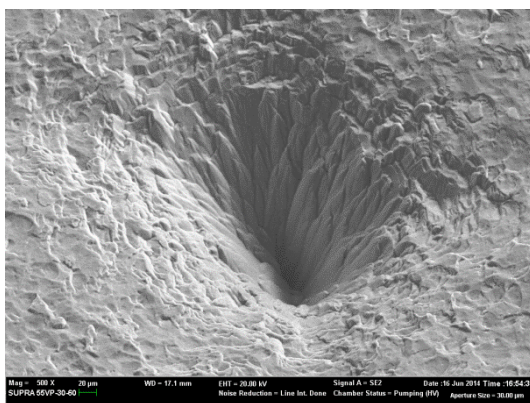
Figure 7-7 – Aerial FESEM view of the central pit of an Al cathode.

The surface of Al cathodes appeared heavily excavated in the central area and a wide and deep pit was present (Figure 7-7). No trace of cones was noticeable

and no Ar was detected inside the cathodes in correspondence of the anodes, probably due to the removal of previously-implanted atoms caused by the intense sputtering and excavation of the cathodes. This is consistent with the fact that Al has the lowest atomic mass (27 u) and its sputter yield is higher than those of the other tested materials, with the only exception of Cu [13].

Cu-Cu cathodes
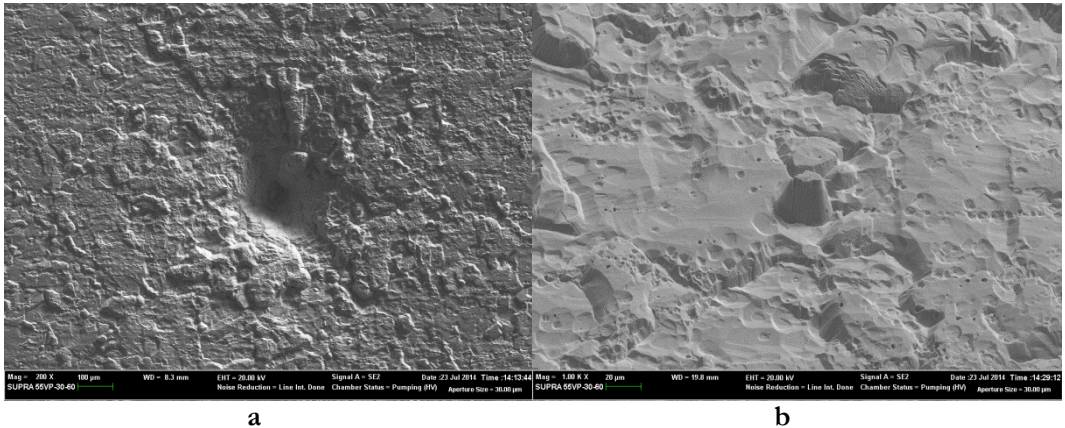
Figure 7-8 – a) Erosion pit in the middle of a Cu cathode; b) presence of micro holes created by sputtering on the surface of the same cathode.

The surface of Cu cathodes was even more excavated, as Cu—being a noble metal—has by far the highest sputter yield among the materials under investigation [13]. This aspect was confirmed after the use of Cu cathodes even by a simple inspection of IP-LAB by naked eye, which evidenced the widespread presence of a Cu sputtered layer on the anodes and on the inner surfaces of the pump. Also in this case, a wide and deep pit was observed in the middle of each cathode (Figure 7-8a). The strong sputtering occurred was proven also by the presence of several micro holes on the cathode surface (Figure 7-8b).

Another pair of Cu cathodes was analysed, which—unlike the usual testing sequence—pumped larger quantities of Ar and He and none of the other gases. In this case, the cathode surface was even more sputtered, with a very large central pit (Figure 7-9a). Patterns of very small cones (diameter <1 μm) were noticeable in some areas of the cathodes; however, their small size and the complete lack of Ar

inside them proved that they were probably not similar to those observed on Ti cathodes (Figure 7-9b).

a   b
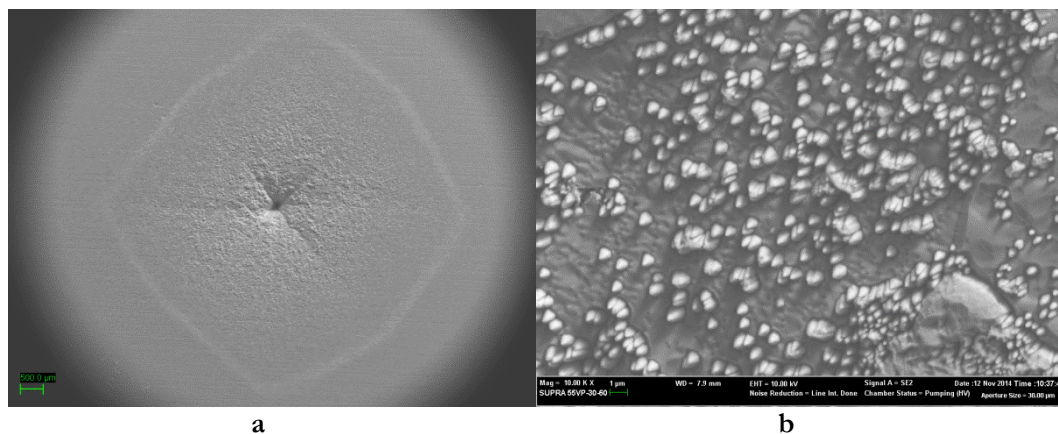
Figure 7-9 – a) Aerial view of the central portion of a Cu cathode which pumped large amounts of Ar and He; b) patterns of very small cones on the surface of the same cathode.

Zr-Zr cathodes

Few large cones were found on the surface of these cathodes in proximity of the central pit (Figure 7-10). At a closer look, the structure of cones' sections was similar to the one of cones on Ti cathodes: the radial growth of columnar structures around a very small inner ring was recognisable (Figure 7-10b). EDX analyses made on these sections evidenced the presence of consistent amounts of Ne and Ar (Figure 7-11a and Table 7-2), on average rather higher compared to those observed in cones on Ti cathodes. Ne seemed to be concentrated in the small inner ring (15.78 at.% for spectrum 1 in Figure 7-11a), while Ar was found in smaller concentrations in the outer radially-grown layer. The observed small fraction of Hf (~1.25 at.%) was an intrinsic characteristic of the supplied cathode material. No trace of other gases (He, CH_4, N_2) was detected and there was no evidence of other concentric layers with a more compact morphology, as those observed in the previous cases.

The signs of sputtering were recognisable on the cathode surface beneath the cones, where Ar and Ne were as usual not present. The cathode surface was fragmented in a pattern of irregular polygons—mostly hexagons—distinguishable

in two different groups according to their morphological appearance and probably corresponding to the crystal grains (Figure 7-11b). This distinction was however merely morphological and it was not supported by any backscattering or EDX observation about the chemical composition of the sample or the eventual inclusion of adsorbed gas molecules.

a   b
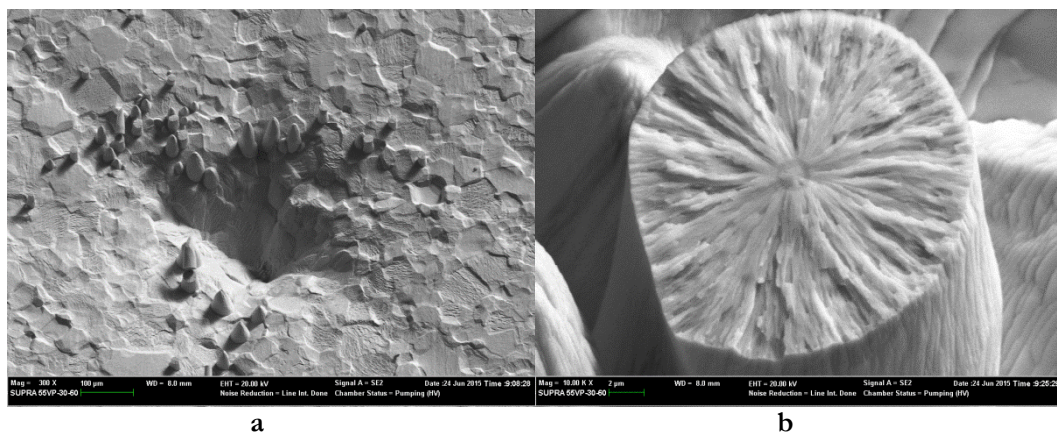
Figure 7-10 – a) Presence of cones around the central pit of a Zr cathode; b) section of one of these cones, evidencing the presence of a radially-symmetrical columnar growth.

Spectrum	Elements [at.%]			
	Ne	Ar	Zr	Hf
1	15.78	---	82.96	1.26
2	---	4.64	94.14	1.22
3	---	2.96	95.77	1.27

Table 7-2 – Elements detected by EDX in Zr bulk cathodes in the spots of Figure 7-11a (all results are in at.%).
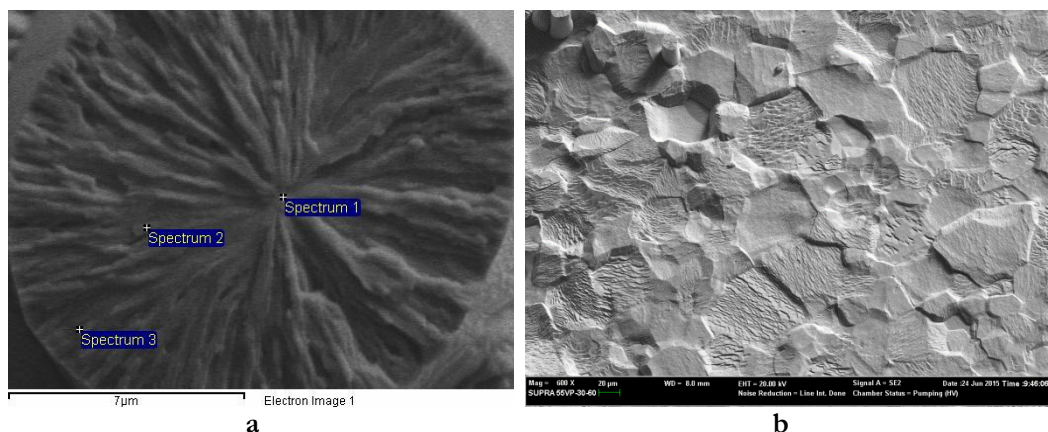
Figure 7-11 – a) EDX analyses on the cross-section of a broken Zr cone; b) pattern of irregular polygons on the cathode surface.

Nb-Nb cathodes

On the contrary, Nb cathodes were not affected by the presence of cones. The extent of the central pit and of the sputtered area was smaller compared to the previous cases (Figure 7-12a), even to the naked eye. At a closer look, the effects of sputtering were nevertheless clear (Figure 7-12b).
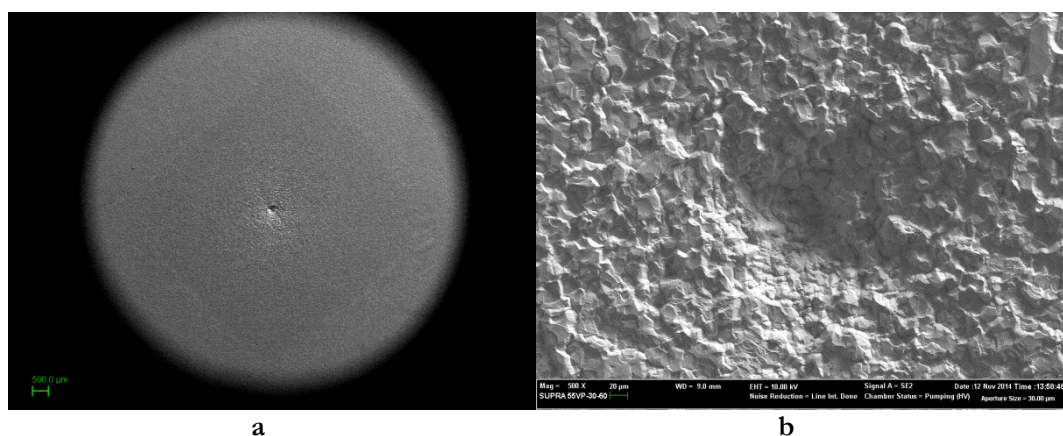
Figure 7-12 – a) Aerial view of the central portion of a Nb cathode; b) closer view of the pit in its middle.

On a smaller scale, the sputtered Nb surface was covered by peculiar structures, mainly patterns of small aligned pyramids (Figure 7-13a) or parallel close-packed sheets (Figure 7-13b), surrounded by more compact cathode portions. No sign of any pumped gas was in any case detected by EDX, neither in these protruding objects nor in the surrounding flat cathode surface. This was quite odd, since Nb and Zr—on which patterns of Ne and Ar-rich cones have been documented—have almost the same atomic mass (93 u *vs.* 91 u, respectively) and sputter yield.

| a | b |
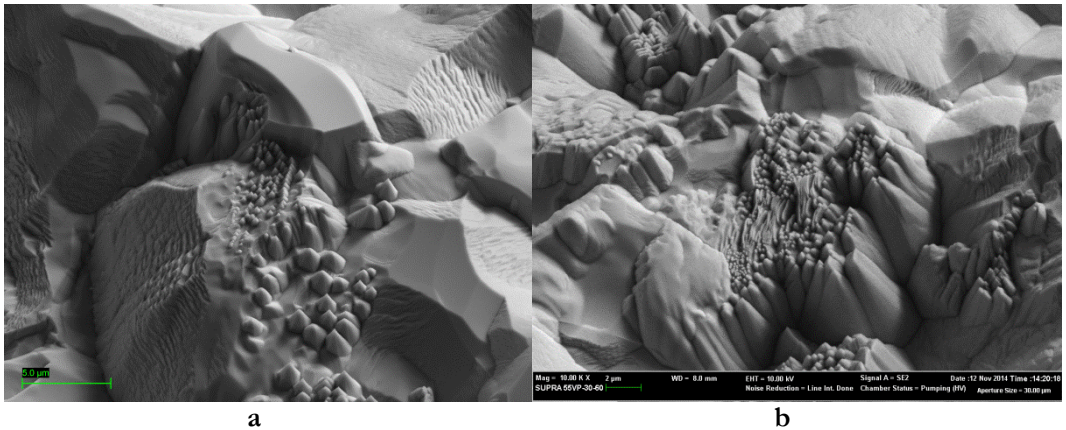
Figure 7-13 – a) Microscopic pyramids on Nb cathode surface; b) other sputtering morphologies observed on the same cathode.

Ta-Ta cathodes

After the first usual series of sorption tests performed in IP-LAB, the effects of sputtering on Ta cathodes were negligible in comparison with the other materials. Erosion was noticeable on the surface but this was the only case in which a real pit in the middle of the cathodes was not present (Figure 7-14a). No trace of any implanted gas molecules was detected by EDX.

Following this first series of sorption tests and FESEM/EDX analyses, these Ta cathodes were reinstalled in IP-LAB and a further, very long Ar sorption tests (about 0.6 Torr·l) was made with them. Afterwards, the samples were again inspected by FESEM/EDX. A pit was at this point present in the middle of each cathodes and erosion of the surface was more evident in its close surroundings

(Figure 7-14b). Apart from this, there were no other signs of sputtering like, for instance, cones.

a　　　　　　　　　　　　　b
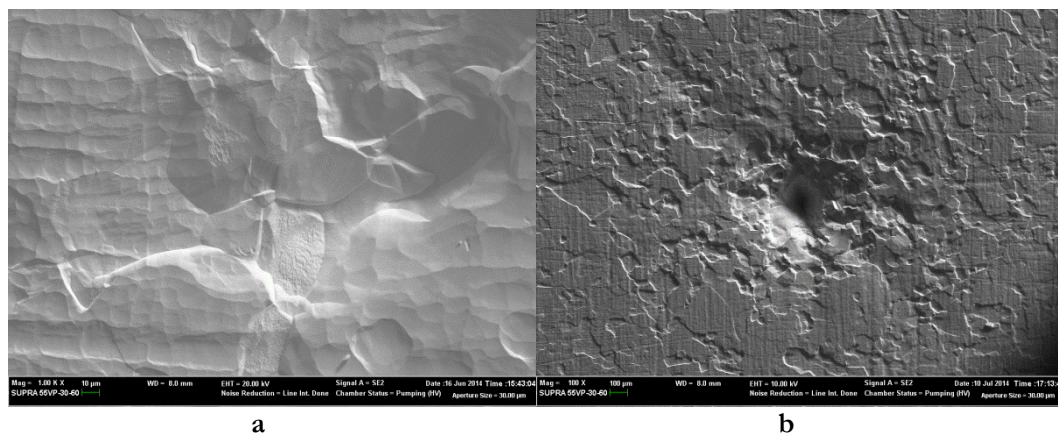
Figure 7-14 – a) Central area of a Ta cathode after the standard sequence of sorption tests; b) Erosion pit in the middle of the same Ta cathode after the further sorption of 0.6 Torr·l of Ar.

Cu-Ti cathodes

Couples of cathodes, each one made of a different material, were analysed by FESEM/EDX in order to find any possible mutual influence of each cathode on the other one during SIP functioning.

The surface of a Cu cathode that had worked together with a Ti one was heavily sputtered, as in the case of Cu-Cu cathodes (Figure 7-15a and Figure 7-15b). Around the central pit and inside each cell in correspondence of the anodes, the EDX revealed that the surface was entirely made of Cu and neither Ti nor any gaseous element was detectable. Outside these zones, in net-redeposition areas, Ti was instead observed and it was always associated with certain amounts of Ar. Table 7-3 shows an example of how the relative concentrations of Ar, Cu, and Ti were able to vary upon EDX mapping of small areas—each one relatively close to the others—in proximity of the net-redeposition line corresponding to the anode edges.

a   b
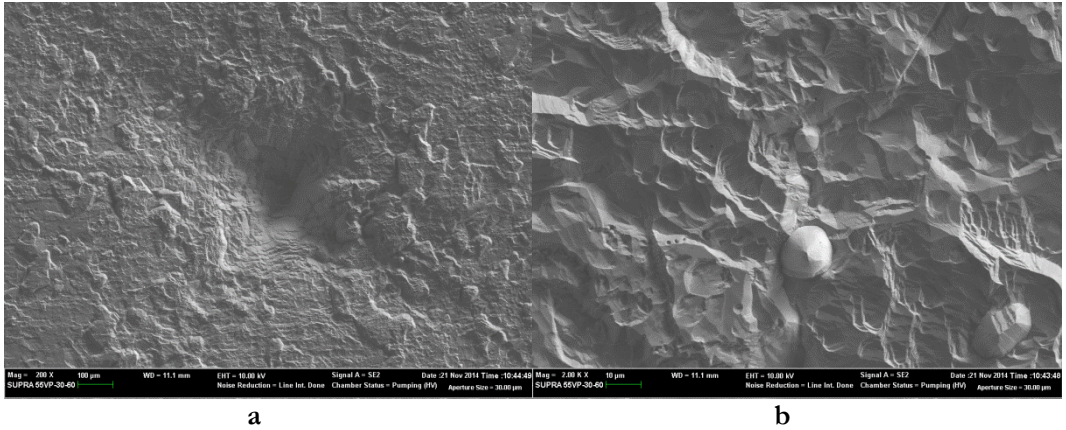
Figure 7-15 – a) Erosion pit in the middle of the Cu cathode which worked with a Ti one; b) closer view of the same cathode.

Spectrum	Elements [at.%]			
	N	Ar	Ti	Cu
1	---	---	---	100.00
2	2.58	1.10	9.32	87.00
3	---	5.11	39.81	55.08

Table 7-3 – Elements detected by EDX in the Cu cathode of the Cu-Ti coupling in three spots close to the net-redeposition line (all results are in at.%).

a   b
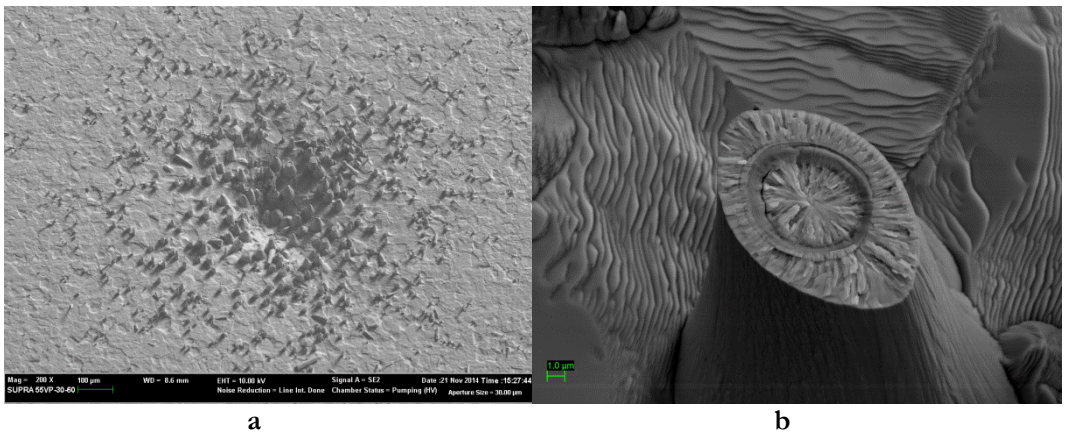
Figure 7-16 – a) Erosion pit in the middle of a Ti which worked with a Cu one; b) section of a broken cone situated near the erosion pit.

On the other side, the Ti cathode was covered with a dense pattern of cones around the central erosion pit (Figure 7-16a). To a lesser extent, cones were found also in the middle of each circle in correspondence of the four anodes. A closer look at the section of broken cones evidenced the usual growth along concentric rings, where the contribution of each pumped gas (Ar, N_2, CH_4, Ne) was recognisable according to the adopted sequence of sorption tests (Figure 7-16b). Similarly to the previous case, the other metal (*i.e.*, Cu) was not detected by EDX in sputtered areas but it was observable in net-redeposition zones, where also implanted Ar atoms were found.

Nb-Cu cathodes

These cathodes did not have any particular feature other than those already mentioned for the two corresponding pairs of identical cathodes (i.e., Cu-Cu and Nb-Nb). The erosion was generally much more pronounced in the Cu cathode than in the Nb one (Figure 7-17a and Figure 7-17b). Cones were missing on both cathodes and each metal was found on the other cathode only in net-redeposition areas.

a   b
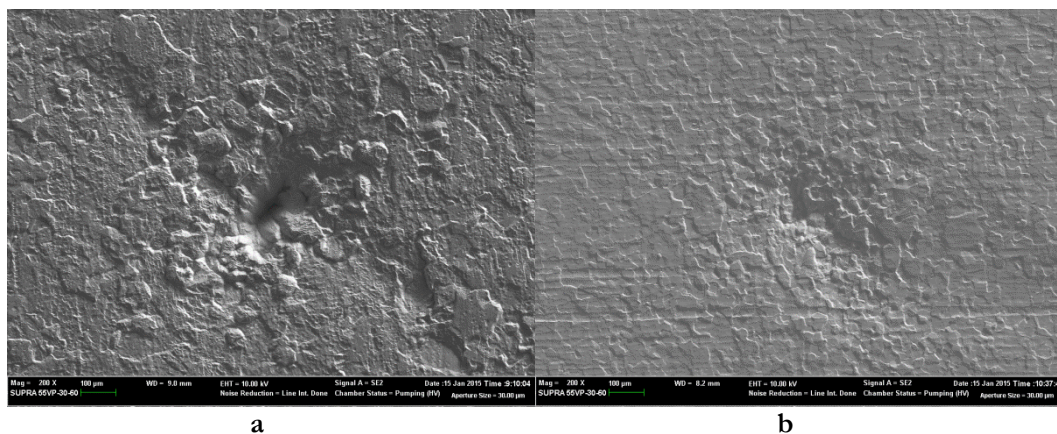
Figure 7-17 – a) Erosion pit in the middle of the Cu cathode of the Nb-Cu coupling; b) erosion pit in the Nb cathode.

Ta-Zr cathodes

Also Ta-Zr cathodes did not give any additional information with respect to Ta-Ta and Zr-Zr ones. The Zr sample was much more eroded than the Ta one (Figure 7-18a and Figure 7-18b). In both cases, cones were not present.

a   **b**
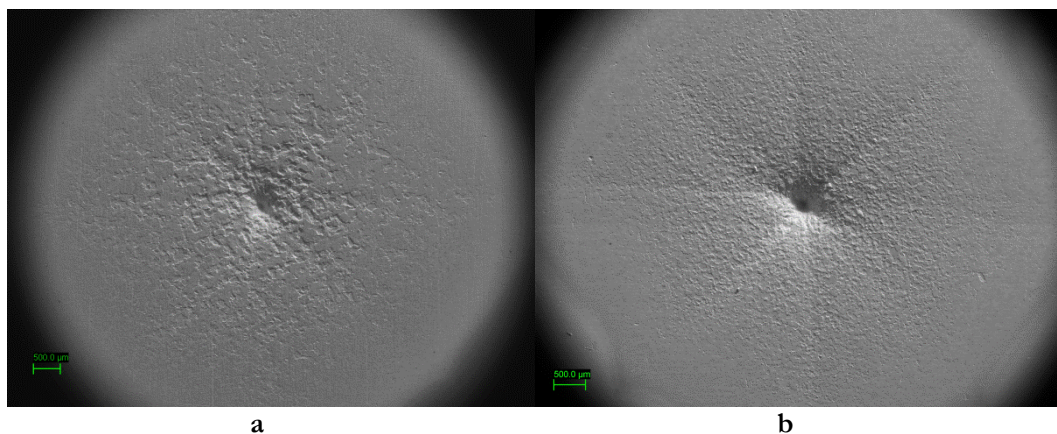
Figure 7-18 – Aerial view of the centre of Ta-Zr cathodes: a) Ta; b) Zr.

7.1.3. HUP cathodes

Ti HUP cathodes

When disassembled from IP-LAB at the end of their series of sorption tests, Ti HUP cathodes appeared particularly eroded compared to the others, even to the naked eye. This peculiarity was confirmed by FESEM imaging of the samples, which highlighted a very wide and deep pit in the middle of each cathode, surrounded by a dense pattern of microscopic cones (Figure 7-19a). It is worth noting how these cones—in contrast to those previously observed on Ti bulk cathodes of conventional SIPs—were clearly arranged radially around the central pit: moreover, even their cross-sections were not perfectly circular but elongated along the circumferences circumscribing the pit (Figure 7-19b). The backscattering imaging evidenced a darker colouring of the cones compared to the cathode

surface beneath them, thus proving that also in this case cones had a less dense structure or a lower atomic mass (Figure 7-20a).
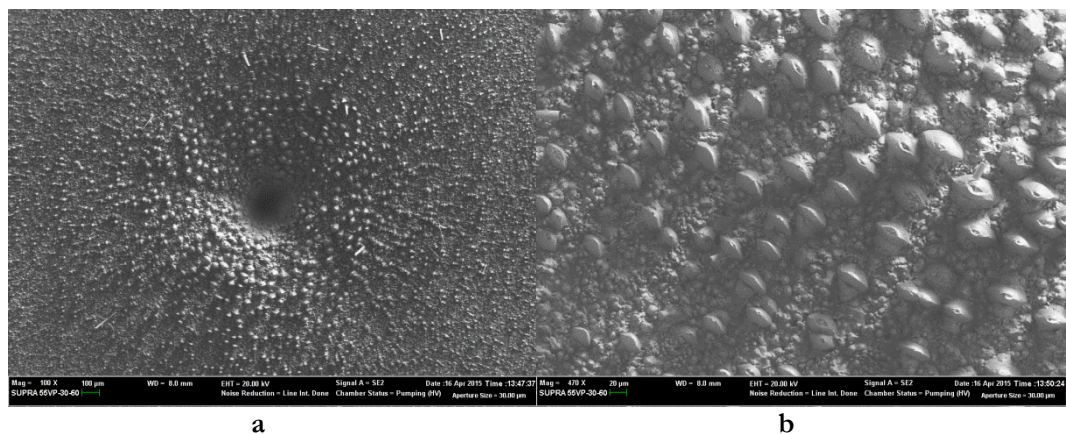
Figure 7-19 – Ti HUP: a) overview of the central pit of a cathode; b) closer view of the microscopic cones surrounding the central pit along concentric lines.
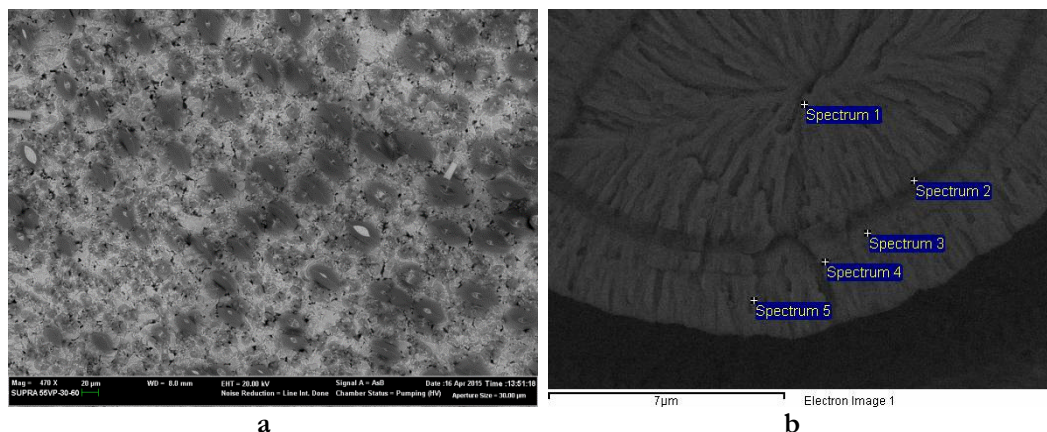
Figure 7-20 – Ti HUP: a) backscattering imaging of cones around the central pit; b) EDX analyses on the cross-section of a broken cone, evidencing its tree-like structure.

A further analogy with cones observed on Ti cathodes of conventional diode SIPs was represented by the tree-like growth recognisable in the cross-section of broken cones, evidencing a series of concentric rings of different thickness. As in the previous case, the sequence of rings and their composition was directly linked

to the pumping history of the SIP, as confirmed by EDX analyses: starting from the centre, each gas used in the testing sequence (CH_4, Ne, N_2, Ar) was roughly detected in its corresponding ring, with the usual exception of He (Figure 7-20b and Table 7-4). In general, the EDX evidenced the presence of significant quantities of Ar (few at.%) inside the cones.

	Elements [at.%]				
Spectrum	C	N	Ne	Ar	Ti
1	---	---	---	1.55	98.45
2	---	37.76	---	1.51	60.73
3	3.52	---	6.92	---	89.56
4	---	---	2.82	1.51	95.67
5	---	---	---	2.98	97.02

Table 7-4 – Elements detected by EDX in TI HUP cathodes in the spots of Figure 7-20b (all results are in at.%).

a   b
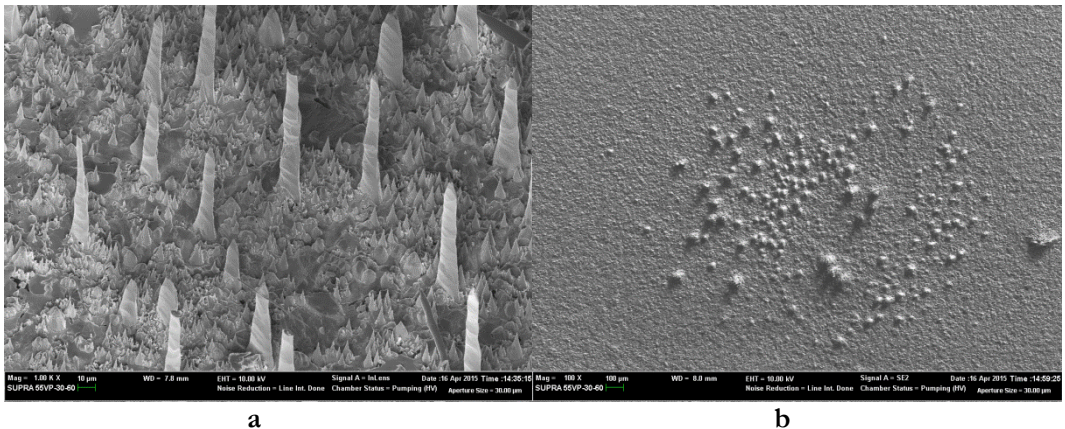
Figure 7-21 – Ti HUP: a) large and small cones covering the cathode surface around the central pit; b) cones in the middle of one of the circular areas in correspondence of the anodes.

The density of cones was by far higher compared to all the previous examples; they were arranged in an array of larger and slender cones surrounded by a forest of much smaller ones, which completely covered the underlying cathode surface (Figure 7-21a). In addition, cones were found also in the middle of the four circular areas in correspondence of the anodes (Figure 7-21b), even

though they were not so many and not as sharp as around the central pit. This abundance of cones on Ti HUP cathodes might be possibly related to their scarce pumping performance during the sorption tests. Their Ar and Ne pumping speeds, in particular, were the lowest among all the tested cathodes, even lower than those ensured by conventional diode SIPs.
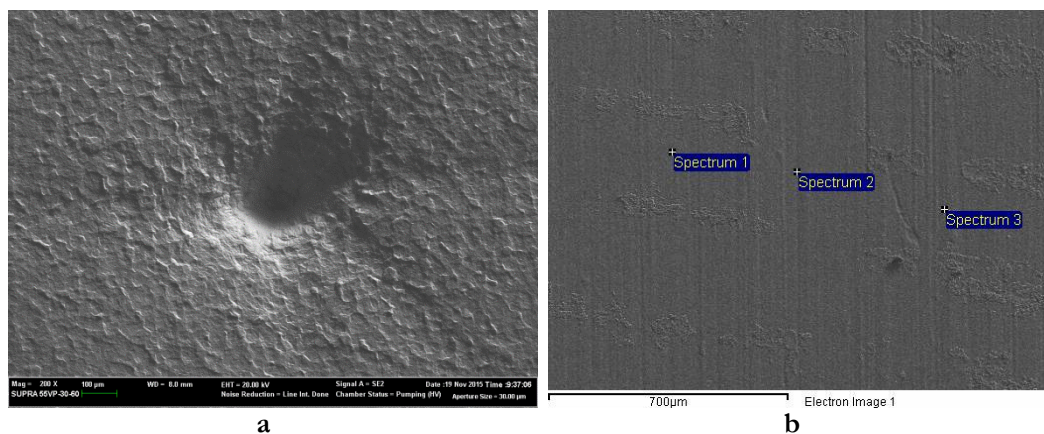
ZrTi cathodes

Figure 7-22 – a) Overview of the central erosion pit of a $Zr_{50}Ti_{50}$ HUP cathode; b) EDX spots in proximity of the projection of the anode edges.

| Spectrum | Elements [at.%] | | | |
	Ar	Ti	Kr	Zr
1	---	47.22	---	52.78
2	---	41.21	---	58.79
3	6.20	43.60	1.25	48.95

Table 7-5 – Elements detected by EDX in a $Zr_{50}Ti_{50}$ HUP cathode in the spots of Figure 7-22b (all results are in at.%).

Quite unexpectedly, cones were not found on $Zr_{50}Ti_{50}$ HUP cathodes, whose surface was simply excavated by sputtering around the usual central erosion pit (Figure 7-22a). EDX analyses made in this central area did not evidence the presence of any implanted gas species: the composition was always very close to the nominal one (50 at.% Ti and 50 at.% Zr). On the contrary, significant

quantities of Ar and Kr were found, as expected (these cathodes underwent also a Kr sorption test at the end of the sequence), along the projections of the anode edges (Figure 7-22b and Table 7-5); however, there was no noticeable morphological difference between these implantation sites and the neighbouring areas (Figure 7-22b).

$Ta_{35}Ti_{65}\_1$ cathodes

$Ta_{35}Ti_{65}\_1$ cathodes have been annealed at 1100 °C for 40 min. At first glance, the effects of sputtering and SIP functioning on their surface were not so evident as in the previous cases (see for instance Ti HUP cathodes in Figure 7-19a) and the central pit was much less deep and wide (Figure 7-23a, which has the same magnification and working distance of Figure 7-19a, and Figure 7-23b). No trace of cones was noticed, neither in the areas in correspondence of the anodes nor around the central pit.

FESEM imaging with secondary electrons evidenced the coexistence on the cathode surface of two interwoven phases with different morphology: one rougher and the other smoother and made of an array of irregular hexagons. By backscattering imaging, these zones were clearly different, the smooth ones being darker than the others (Figure 7-24a). By EDX, bright areas were on average much richer in Ta than dark ones; EDX spectra made on extended areas comprising both phases resulted instead in the nominal 35-65 composition ratio (Table 7-6).

a   b
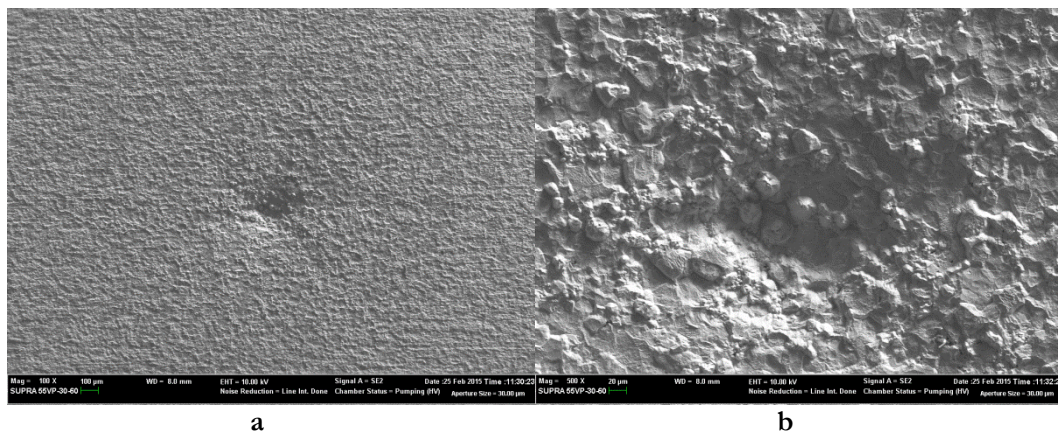
Figure 7-23 – $Ta_{35}Ti_{65}\_1$: a) overview of the central pit of a cathode; b) closer view of the same area.
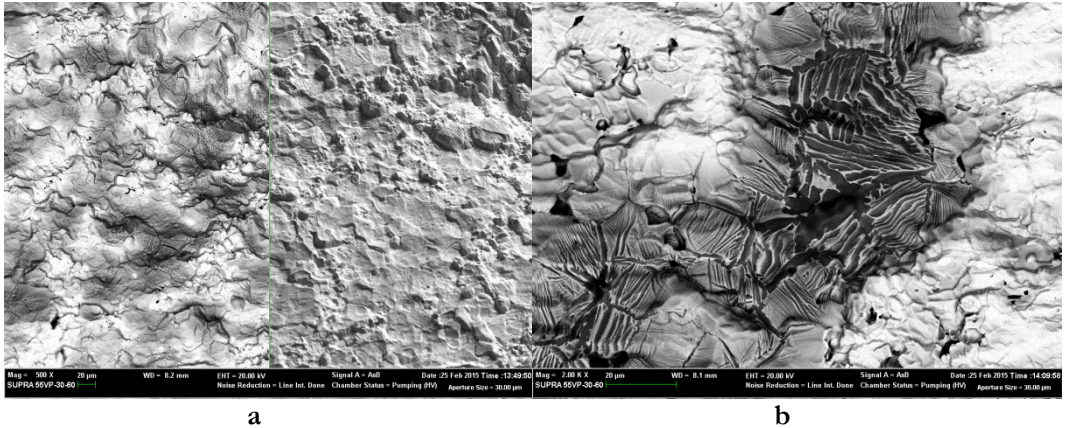
Figure 7-24 – Ta$_{35}$Ti$_{65}$_1: a) Backscattering (left) and secondary-electrons (right) imaging evidencing the presence of two different morphologies; b) view of a the lamellar structures growth in the Ti-enriched areas.

Using a higher magnification, dark areas revealed a peculiar lamellar structure alternating dark and bright layers and resembling an eutectic system (Figure 7-24b). The characteristic length of these lamellar areas was of the order of few tenth of μm. The EDX analyses showed that the darkest lamellae were made almost entirely of Ti (only 3 at.% Ta on average); the greyer ones still had a clear predominance of Ti (about 20 at.% Ta).

	Elements [at. %]	
	Ti	**Ta**
Dark areas	85	15
Bright areas	15	85
Extended areas	65	35

Table 7-6 – Mean elemental composition detected by EDX in dark and bright areas of Ta$_{35}$Ti$_{65}$_1 cathodes (all results are in at. %).

Ta$_{35}$Ti$_{65}$_2 cathodes

Conversely, the appearance of Ta$_{35}$Ti$_{65}$_2 cathodes, which had been annealed at 800 °C for 3 h, was quite different. Erosion signs were more pronounced and the central pit was larger and deeper compared to Ta$_{35}$Ti$_{65}$_1 ones (cf. Figure 7-25a

and Figure 7-25b, which have the same magnification and working distance of Figure 7-23a and Figure 7-23b, respectively).
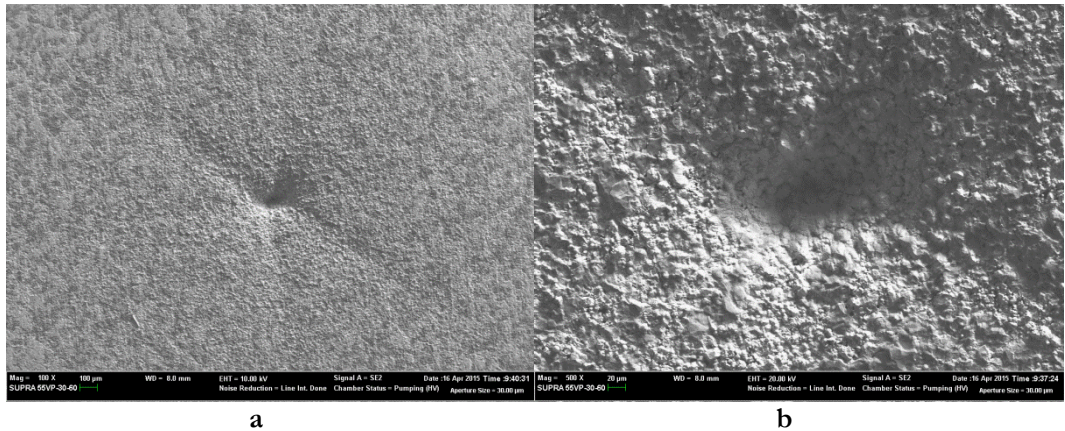

a   b

Figure 7-25 – Ta$_{35}$Ti$_{65}$_2: a) overview of the central pit of a cathode; b) closer view of the same area.

Spectrum	Elements [at.%]	
	Ti	Ta
1	100.00	---
2	59.53	40.47
3	1.52	98.48
4	83.15	16.85
1	79.22	20.78

Table 7-7 – Ta$_{35}$Ti$_{65}$_2: elemental composition detected by EDX in the spots of Figure 7-27a and on the extended area of Figure 7-27b (all results are in at.%).

Rough and smooth zones were still noticeable but with a clear predominance of the previous ones. At the same time, the division between these two different morphologies seemed to be more definite (Figure 7-26); this might be a consequence of the lower annealing temperature of these cathodes compared to Ta$_{35}$Ti$_{65}$_1 ones, where thermally-driven interdiffusion was probably more enhanced (800 °C *vs.* 1100 °C, respectively). Table 7-7 shows the wide variation of Ti and Ta atomic percentage measured by EDX in four different spots of Figure 7-27a; the last row describes the average elemental composition calculated on a

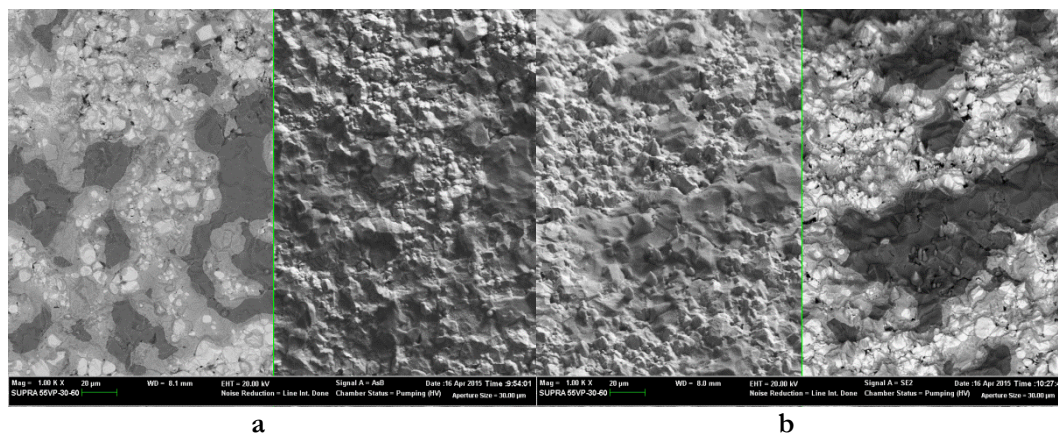larger area which comprises both phases, showing that in this case the nominal 35-65 Ta-Ti ratio was not respected.

Figure 7-26 – Ta$_{35}$Ti$_{65}$_2: backscattering and secondary-electrons imaging of two separated areas (a, b) evidencing in each one the presence of two different morphologies.
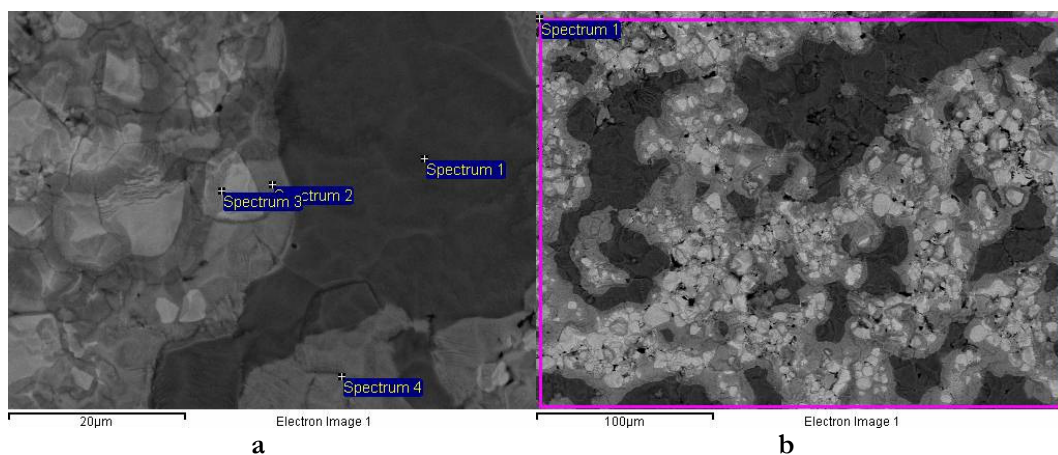

Figure 7-27 – Ta$_{35}$Ti$_{65}$_2: a) EDX analysis spots in zones with different morphology; b) EDX analysis on an area comprising both morphologies.

This discrepancy might originate during SIP functioning from sputtering, which could possibly lead to a preferential accumulation of Ti atoms coming from other areas or from the opposite cathode. Another feature probably ascribable to

the low-temperature thermal treatment was the absence of any kind of lamellar structures, as those observed in $Ta_{35}Ti_{65}\_1$ cathodes.

$Ta_{50}Ti_{50}$ cathodes prior to the thermal treatment

a   b
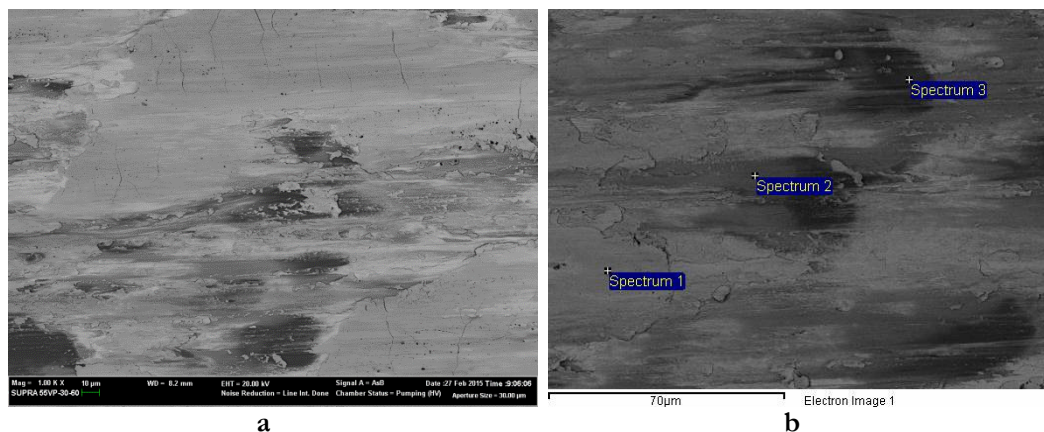
Figure 7-28 – $Ta_{50}Ti_{50}$ prior to the thermal treatment: a) morphology of the cathode surface; b) spots chosen for EDX analysis.

	Elements [at.%]			
Spectrum	C	O	Ti	Ta
1	11.78	28.87	27.53	31.82
2	10.01	---	79.84	10.15
3	7.49	---	90.76	1.75

Table 7-8 – $Ta_{50}Ti_{50}$ prior to the thermal treatment: elemental composition detected by EDX in the spots of Figure 7-28b (all results are in at.%).

One $Ta_{50}Ti_{50}$ cathode was analysed by FESEM/EDX also before undergoing the annealing thermal treatment. Its surface was of course much smoother than the others were, since the cathode was new and sputtering never occurred on its surface. In spite of the lack of a high-temperature annealing, by backscattering imaging it was already possible to distinguish small, dark (i.e., Ti-rich) areas dispersed in a whiter and thus Ta-rich matrix (Figure 7-28a). Moreover, a large fraction of the cathode surface was covered by a thick, light-coloured layer of different nature, which was identified by EDX as a carbonaceous oxide layer

(Figure 7-28 and Table 7-8). Its absence on the other cathodes seems to confirm the effectiveness of the thermal treatment in the cleaning of the cathode surfaces and in the removal of contaminants.

$Ta_{50}Ti_{50}\_1$ cathodes

As $Ta_{35}Ti_{65}\_1$ cathodes, $Ta_{50}Ti_{50}\_1$ ones underwent a thermal treatment at 1100 °C for 40 min. Figure 7-29a and Figure 7-29b show the central pit with the same magnification and working distance comparable with the previous images of Ti HUP, $Ta_{35}Ti_{65}\_1$ and $Ta_{35}Ti_{65}\_2$.
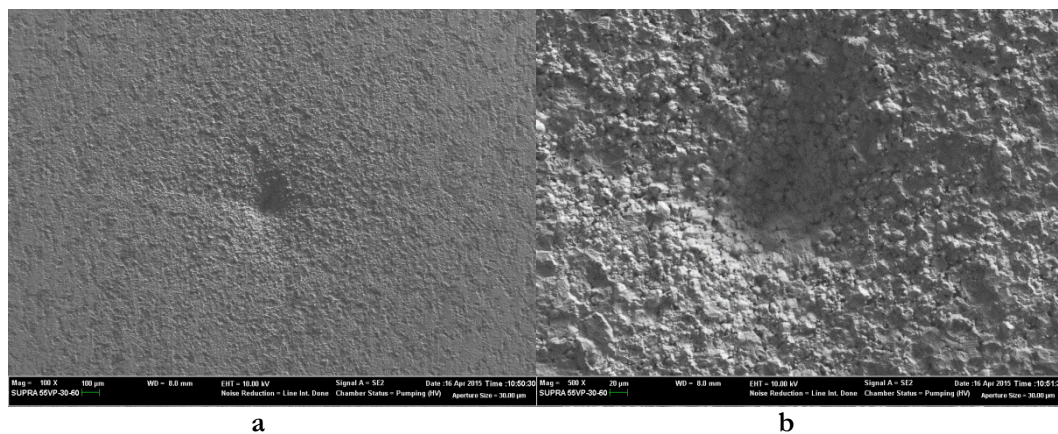
Figure 7-29 – $Ta_{50}Ti_{50}\_1$: a) overview of the central pit of a cathode; b) closer view of the same area.

At a closer look, lamellar structures similar to those of $Ta_{35}Ti_{65}\_1$ cathodes were observed in several different locations (Figure 7-30); interestingly, these lamellae were always found in proximity of large, dark areas, as if they were the result of a sort of diffusion mechanism starting from these points. The presence of lamellae on $Ta_{35}Ti_{65}\_1$ and $Ta_{50}Ti_{50}\_1$ cathodes, both annealed at 1100 °C for 40 min, might be thus a consequence of the chosen thermal treatment. Compared to $Ta_{35}Ti_{65}\_1$, however, the extent of these lamellae and their characteristic dimensions were smaller. The elemental composition of these areas measured by EDX is reported in Table 7-9 and it is in line with the analogous areas of $Ta_{35}Ti_{65}\_1$ cathodes.
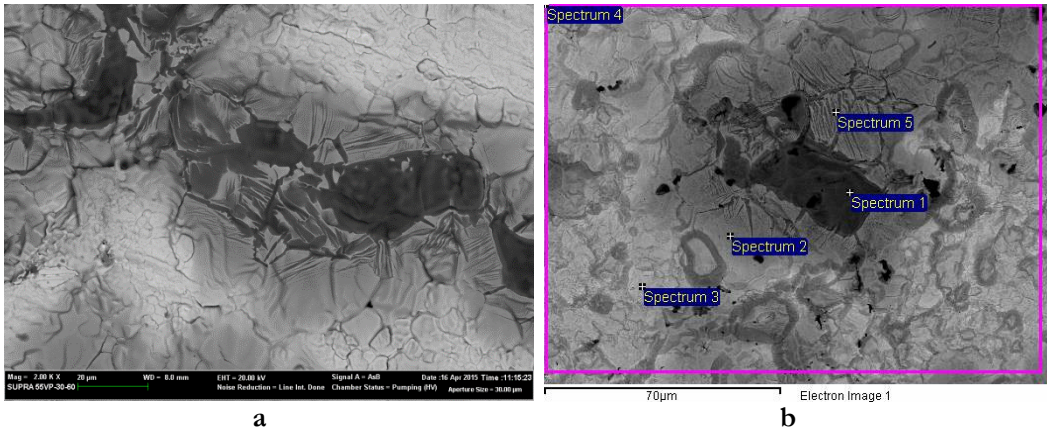
a   b

Figure 7-30 – Ta$_{50}$Ti$_{50}$_1: a) and b) backscattering imaging of lamellar structures in the surroundings of dark, Ti-rich nuclei.

Spectrum	Elements [at.%]		
	N	Ti	Ta
1	---	100.00	---
2	---	73.61	26.39
3	---	---	100.00
4	4.73	56.56	38.70
5	---	80.65	19.35

Table 7-9 – Ta$_{50}$Ti$_{50}$_1: elemental composition detected by EDX in the spots of Figure 7-30b (all results are in at.%).

As for the previous cases, the backscattering and secondary-electrons FESEM imaging revealed the coexistence of two different morphologies on the surfaces of these cathodes: bright, rough and Ta-rich areas juxtaposed to darker, smoother and Ti-richer ones (Figure 7-31a). Lamellar structures were found only in these latter smooth zones. Again, a sort of array of irregular hexagons was recognisable in the darker and smoother portions of the cathode surface (Figure 7-31b).
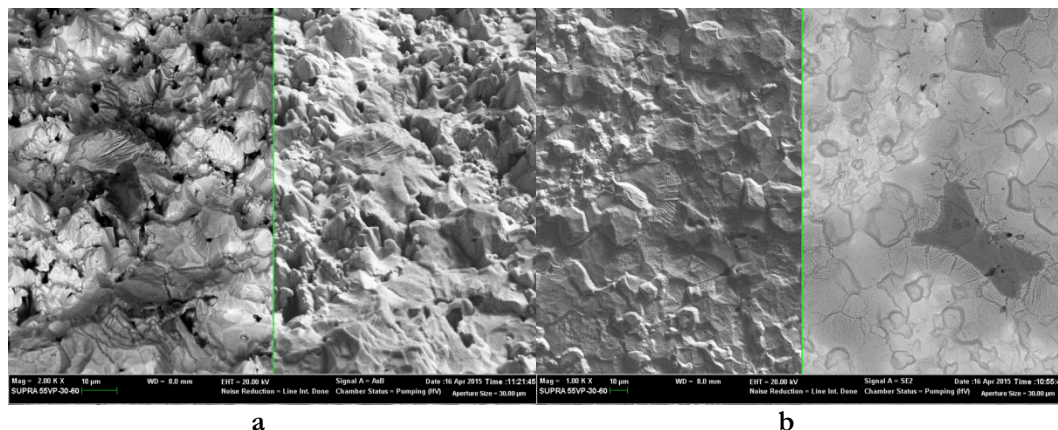
Figure 7-31 – Ta$_{50}$Ti$_{50}$_1: a) backscattering and secondary-electrons imaging of evidencing the presence of two different morphologies; b) presence of irregular hexagons and lamellae in the smooth portions of the cathode surface.

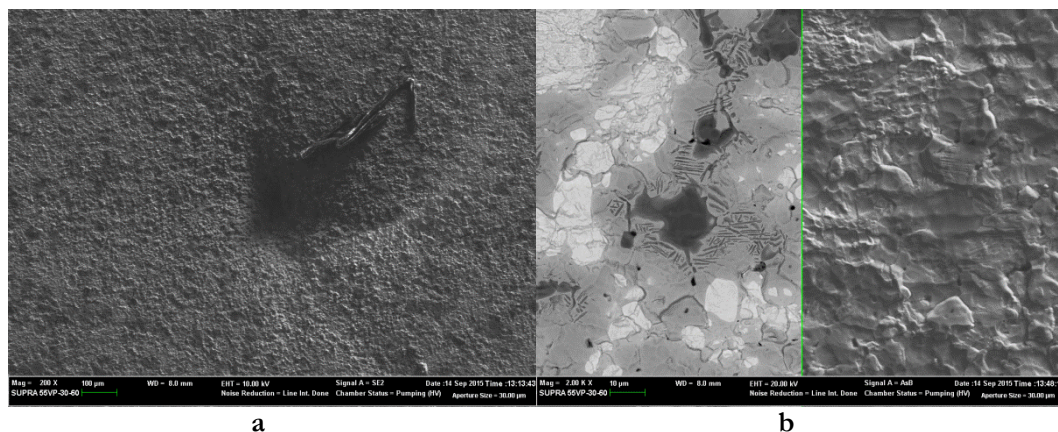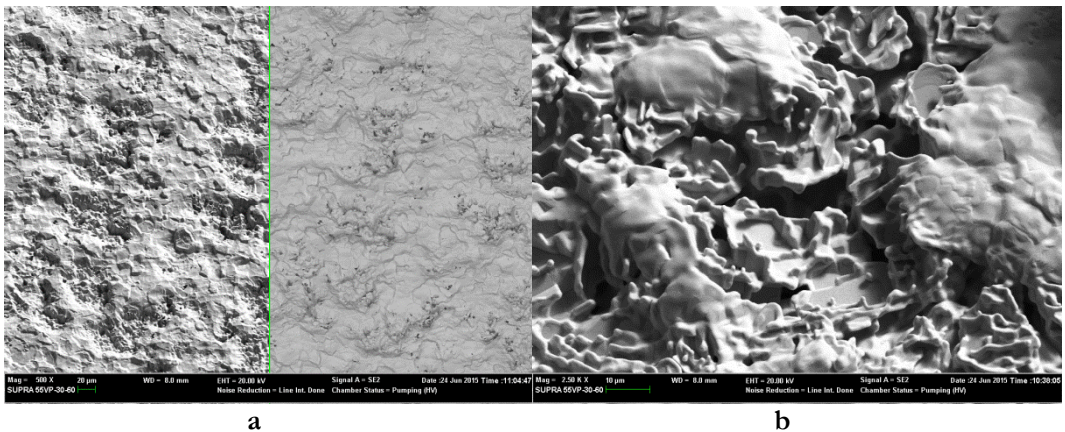*Ta$_{50}$Ti$_{50}$_2 cathodes*

Figure 7-32 – a) Overview of the central pit of one of the Ta$_{50}$Ti$_{50}$_2 cathodes; b) view of some dark Ti-rich areas surrounded by narrow lamellae.

Ta$_{50}$Ti$_{50}$_2 HUP cathodes (annealed at 800 °C for 3 h) were similar to the other TaTi HUP compositions under test. The surface around the central pit was highly corrugated (Figure 7-32a), especially in correspondence of the brighter Ta-richer areas evidenced by backscattering imaging and EDX. Some of these corrugations resembled cones but seemed to be eroded by sputtering; neither Ar

nor any other gas was found inside them. Small dark lamellae were found also on these cathodes around the dark Ti-rich zones (Figure 7-32b), however to a lesser extent than in the previous cathodes annealed at 1100 °C.

Ta$_{50}$Ti$_{50}$_3 cathodes

Ta$_{50}$Ti$_{50}$_3 cathodes have been annealed at 1100 °C for 72 h. Their surface was similar to the other Ta$_{50}$Ti$_{50}$ cathodes, but the alternation of Ta-rich and Ti-rich rough and smooth areas was not so evident as in the previous cases, likely due to a much higher interdiffusion occurred during the 72 h long thermal treatment (Figure 7-33a). Probably for the same reason, lamellae were not observed on these cathodes. Consistently with the long annealing at high temperature, the cathode surface seemed to be completely modified and, in some areas, it was fissured and characterised by an array of interconnected cavities (Figure 7-33b).

a   **b**

Figure 7-33 – a) surface of a Ta$_{50}$Ti$_{50}$_3 cathode, showing the absence of distinct dark and bright Ti-rich and Ta-rich areas; b) closer view of a fissured portion of the cathode.

Ta$_{35}$Zr$_{65}$ cathodes

Ta$_{35}$Zr$_{65}$ cathodes annealed at 1100 °C for 3 h were different from the various TaTi HUP cathodes described above. The area around the central pit was covered by a pattern of cone-resembling structures separated by flatter areas

(Figure 7-34a). The pit was not as deep and wide as in other cathodes with a lower atomic mass. By backscattering imaging, a pattern of dark and bright areas, respectively rich in Zr and Ta, was noticeable. These zones were clearly distinct and there was no intermediate colour gradation; typical elemental compositions of these areas measured by EDX are shown in Table 7-10. Unlike TaTi cathodes, this colour (that is, elemental) pattern was not associated with a precise morphological distinction between smooth and rough areas (Figure 7-34b). The EDX did not reveal any implanted gas species in these sputtered portions of the cathodes.

a   b
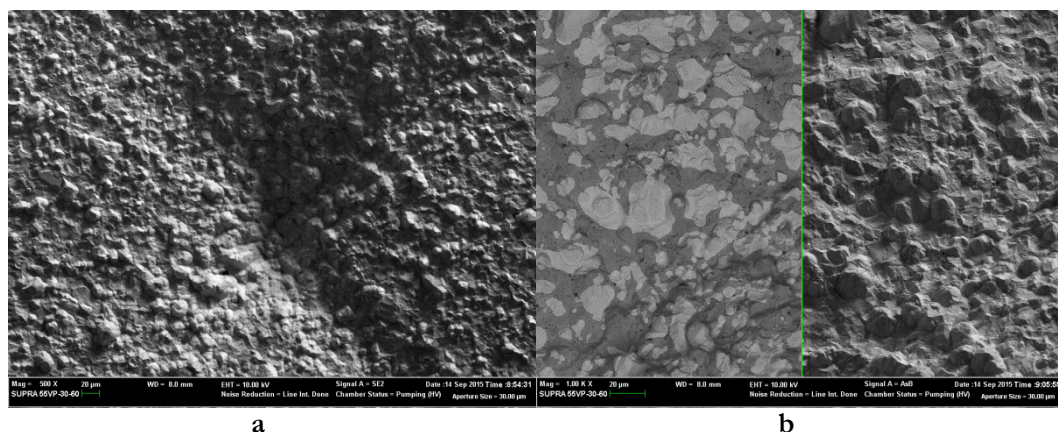
Figure 7-34 – a) Overview of the central erosion pit of a Ta$_{35}$Zr$_{65}$ HUP cathode; b) backscattering and secondary-electron view of an enlarged area of the same cathode.

|	Elements [at.%]	
Spectrum	Zr	Ta
Dark area	95.96	4.04
Bright area	---	100.00

Table 7-10 – Typical elemental composition detected by EDX in dark and bright areas of Ta$_{35}$Zr$_{65}$ HUP cathodes.

Ta$_{50}$Zr$_{50}$ cathodes

Ta$_{50}$Zr$_{50}$ HUP cathodes have also been thermally treated at 1100 °C for 3 h and their surface after the use in IP-LAB had the same characteristics of the

previous Ta$_{35}$Zr$_{65}$ ones, in spite of the slightly different elemental composition (Figure 7-35a).

Again, dark and bright areas evidenced by EDX were clearly distinct but they were not accompanied by a parallel definite distribution of flat and rough zones (Figure 7-35b). Implanted gases were not detected in the eroded areas of these cathodes.
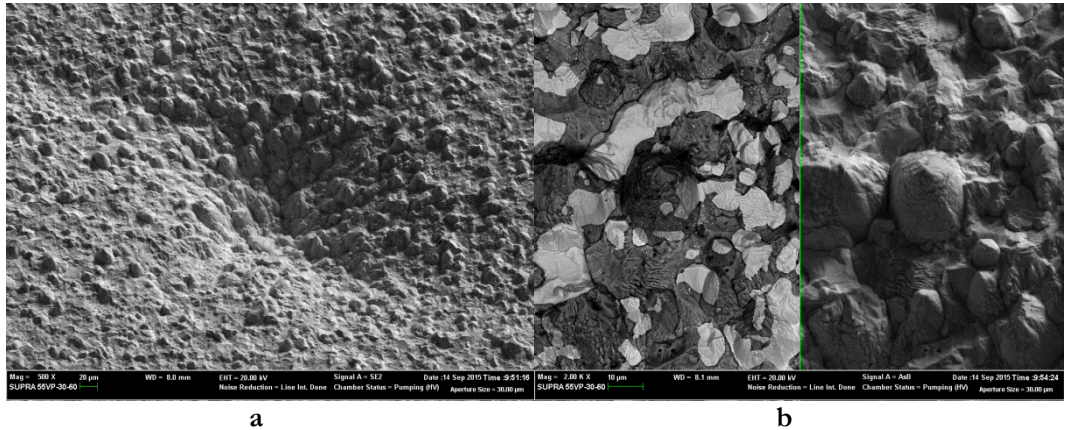
Figure 7-35 – a) Overview of the central erosion pit of a Ta$_{50}$Zr$_{50}$ HUP cathode; b) backscattering and secondary-electron view of an enlarged area of the same cathode.

7.2. XRD analyses of HUP cathodes

HUP cathodes have been analysed also by XRD, in order to ascertain any possible influence of the HUP process and of the thermal treatments on their crystal structure and to find a connection with their sorption performance and the results of FESEM/EDX imaging.

The XRD technique relies on the identification of a diffraction pattern given by the constructive interference of X-rays with a crystalline compound, according to Bragg's law [14]. Each peak corresponds to the constructive interference defined by a precise combination of the following parameters satisfying Bragg's law:

$$n\lambda = 2d \sin \theta$$

where λ is the wavelength of the incident X-rays, θ is the angle of incidence, d is the spacing between two lattice planes and n is an integer number. It follows that it is possible to identify each material through the position of its characteristics peaks by comparison with reference tables, since every crystalline substance gives a unique pattern of X-rays reflected from the planes of its crystal lattice. The crystal structure of an unknown material can be thus determined, together with its lattice size and crystal orientation, since the d and θ parameters are directly related to the Miller indices h,k,l of a lattice. Additionally, the relative intensity of each peak can be used to derive quantitative information about the composition of a sample and variations in a peak's width or position indicate a change in its crystallinity or the presence of residual strains in the lattice, respectively. The full width at half maximum (FWHM) of a peak is an important parameter for the collection of information about crystallinity, crystal size and lattice strains; the larger is this number, the lower is crystallinity.
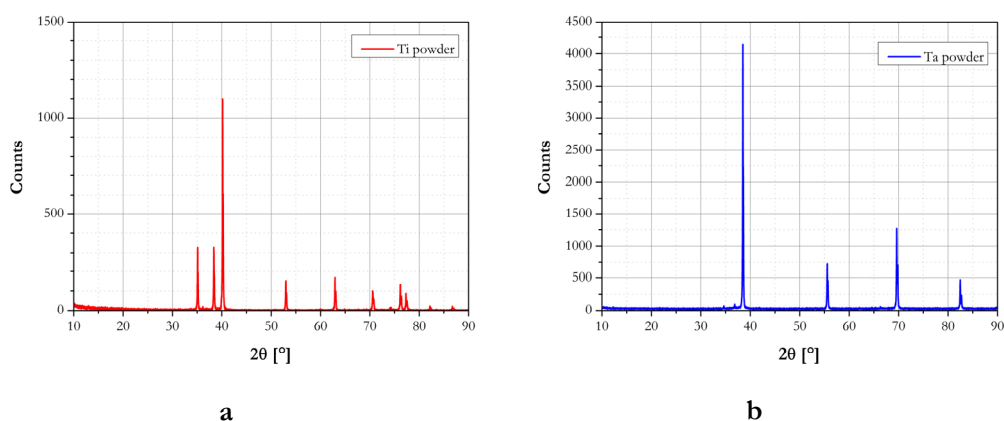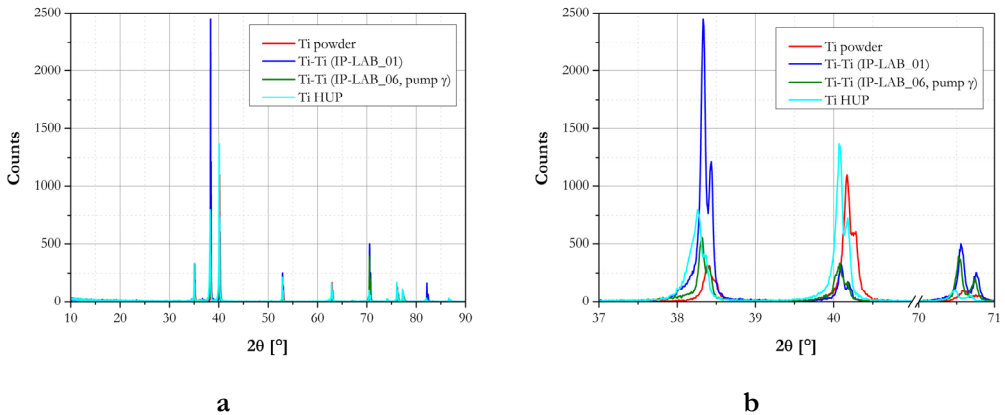

Figure 7-36 – Diffraction patterns of a) Ti powders and b) Ta powders.

Preliminary analyses were made on the Ti and Ta powders employed in the preparation of TaTi HUP cathodes. The diffraction pattern of Ti powders evidenced the characteristic peaks of an hexagonal close-packed (HCP) crystalline lattice (Figure 7-36a); Ti α phase has an HCP lattice and it is stable at room temperature, while the transition to the β phase—which is body-centred cubic

(BCC)—takes place at 882 °C. On the other side, the pattern of Ta powders (Figure 7-36b) identified a BCC structure (α phase), consistently with the fact that Ta tetragonal β phase is metastable.

The spectrum of Ti powders was also compared to those of all the tested Ti cathodes, both bulk and HUP. All these cathodes had been annealed at 600 °C prior to the installation and use in IP-LAB. The overlapping of the main peaks indicates that the HCP structure of Ti powders was maintained in every case (Figure 7-37a). A closer view of the three main peaks (Figure 7-37b) shows that, as expected, the two spectra of Ti bulk cathodes were very similar. The peaks belonging to Ti powders and Ti HUP cathodes were substantially equivalent, even if slightly shifted.

Figure 7-37 – a) Diffraction patterns of Ti powders together with those of Ti-Ti and Ti HUP cathodes after their use in IP-LAB; b) enlarged view comparing the main peaks of the same spectra.

An analogous comparison was made between Ta powders and Ta bulk cathodes (Figure 7-38a). These latter had the same BCC structure of Ta powders, however with some differences in the shape of the peaks, which were much more defined in the case of powders (Figure 7-38b).
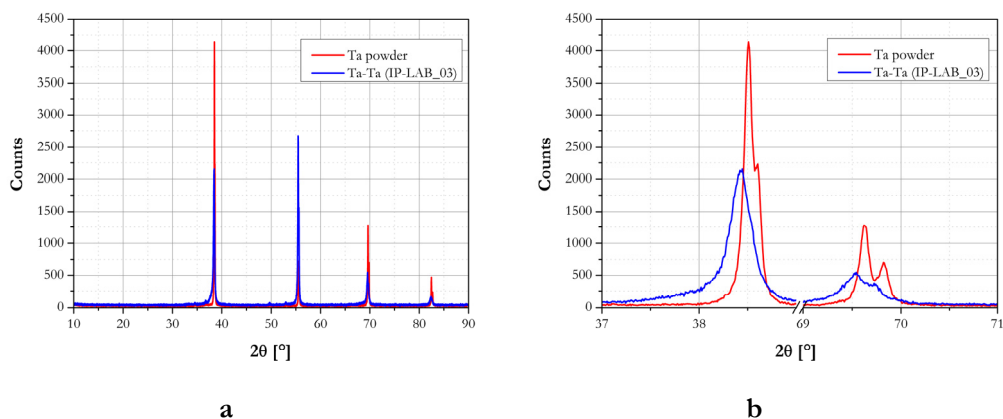
a

b

Figure 7-38 – a) Diffraction patterns of Ta powders and Ta-Ta cathodes after their use in IP-LAB; b) enlarged view comparing the two main peaks of the same spectra.
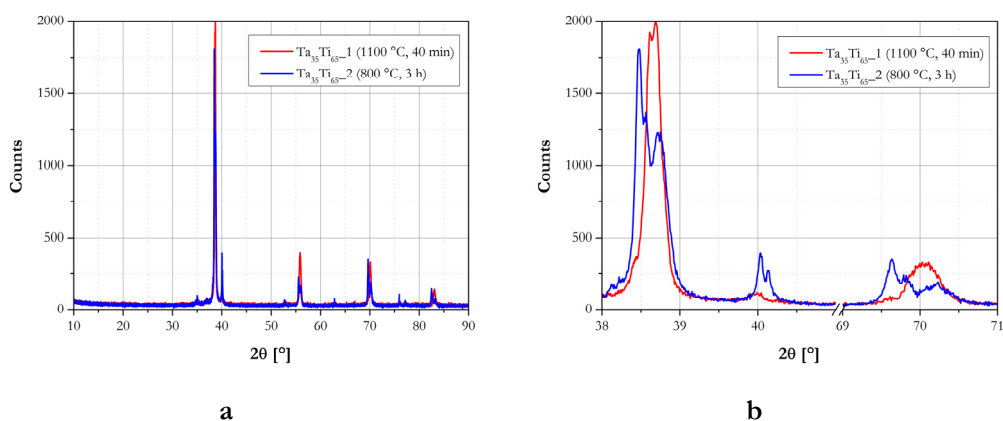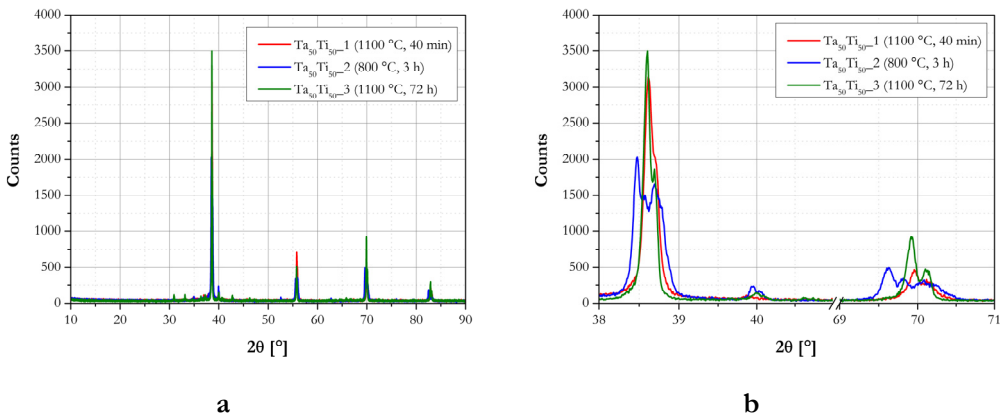

a

b

Figure 7-39 – a) Diffraction patterns of $Ta_{35}Ti_{65}$ HUP cathodes after their use in IP-LAB; b) enlarged view comparing the main peaks of the same spectra.

The differences between $Ta_{35}Ti_{65}\_1$ and $Ta_{35}Ti_{65}\_2$ HUP cathodes, which underwent different thermal treatments (40 min at 1100 °C and 3 h at 800 °C, respectively), are addressed in Figure 7-39a and Figure 7-39b. For both cathodes, the XRD analysis evidenced the presence of BCC Ta and BCC Ti, thus proving a changing of Ti crystalline structure from HCP to BCC during the HUP process. The presence of two separate summits ascribable to Ta and Ti for every main peak

of the $Ta_{35}Ti_{65}\_2$ sample (enlarged view in Figure 7-39b) demonstrated the lower sintering degree obtained with the low-temperature annealing, while the treatment at higher temperature resulted in peaks with a single top, thus indicating a higher degree of sintering. The FWHM measured on the main peak was 0.23 for the sample annealed at 1100 °C and 0.46 for the one treated at 800 °C, evidencing the higher crystallinity of the first sample.

In a similar way, BCC Ta and BCC Ti were found also in all the $Ta_{50}Ti_{50}$ samples (Figure 7-40a). Eventual differences in the presence or not of two summits in the main peaks—indicating a more or less pronounced sintering of Ta and Ti powders—were in this case not so evident as before (Figure 7-40b). However, the main peaks of cathodes annealed at 1100 °C were very similar (regardless of the treatment duration, 40 min or 72 h) and much sharper than in the case of the annealing at 800 °C. The FWHM of the main peak was equal to 0.18 for $Ta_{50}Ti_{50}\_1$ cathodes annealed at 1100 °C and to 0.40 for $Ta_{50}Ti_{50}\_2$ annealed at 800 °C.

a　　　　　　　　　　　　　　　　　**b**

Figure 7-40 – a) Diffraction patterns of $Ta_{50}Ti_{50}$ HUP cathodes after their use in IP-LAB; b) enlarged view comparing the main peaks of the same spectra.

a   **b**
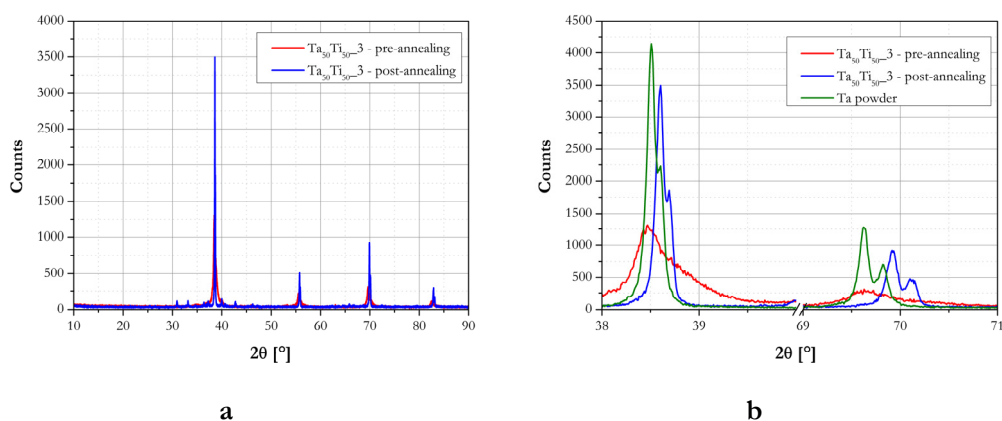
Figure 7-41 – a) Diffraction patterns of Ta$_{50}$Ti$_{50}$_3 cathodes before and after the 72 h thermal treatment at 1100 °C; b) enlarged view of the two main peaks, compared to Ta powders spectrum.

XRD analyses gave also useful information about the effects of the high-temperature thermal treatment made on each pair of HUP cathodes prior to testing their sorption performance in IP-LAB. Figure 7-41a shows two XRD spectra of Ta$_{50}$Ti$_{50}$_3, taken respectively before and after the 72 h long annealing at 1100 °C. Both Ta and Ti had also in this case a BCC lattice, confirming the previous observations made on other Ta$_{35}$Ti$_{65}$ and Ta$_{50}$Ti$_{50}$ HUP cathodes. The observed correspondence in the position of each peak before and after the annealing indicates that the crystalline structure of the compound was not overall affected by the thermal treatment; however, a closer look at the two main peaks of both spectra (Figure 7-41b) demonstrates that a slight shift occurred during the annealing and that both shape and intensity of peaks were modified. The post-annealing peaks, in particular, were much more well-defined and sharp, clearly indicating an increase in the crystallinity of the sample; the FWHM parameter for the main peak, in particular, was 0.46 before the thermal treatment and 0.11 after it.

Finally, the XRD analyses of Ta$_{35}$Zr$_{65}$ and Ta$_{50}$Zr$_{50}$ cathodes were compared with those made on Zr and Ta powders used to produce them. The crystal structure of both TaZr composition was not modified during the HUP process and the following thermal treatment: the peaks typical of the crystal lattice of Zr (HCP) and Ta (BCC) powders were still separated and clearly recognisable (Figure

7-42a). The crystallinity of these two pairs of cathodes, estimated through the usual FWHM, was substantially the same (Figure 7-42b).
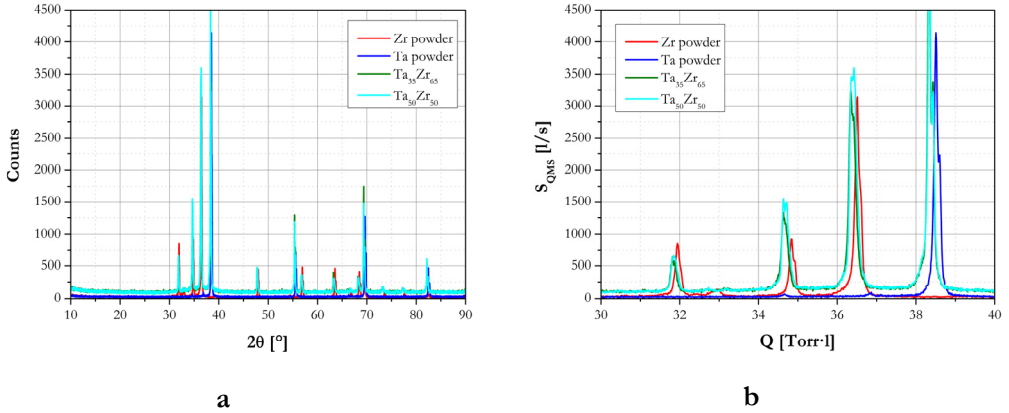

Figure 7-42 – a) Diffraction patterns of Ta$_{35}$Zr$_{65}$ and Ta$_{50}$Zr$_{50}$ cathodes compared to Zr and Ta powders; b) enlarged view showing the main peaks of the same spectra.
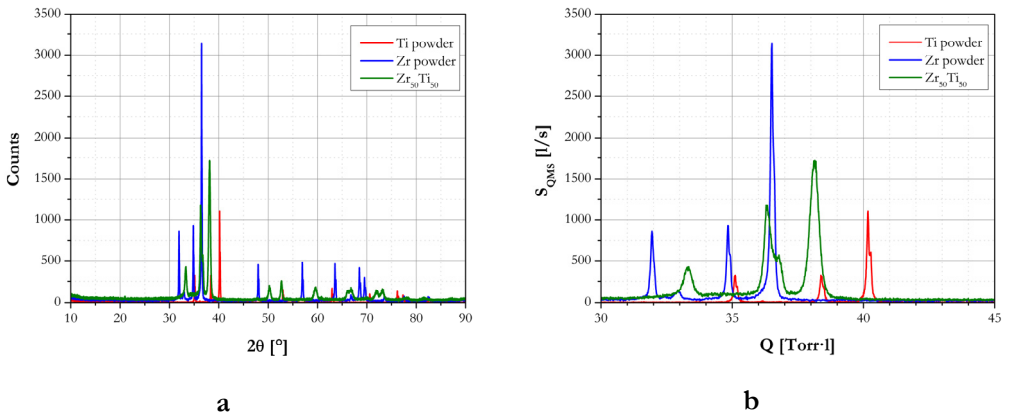

Figure 7-43 – a) Diffraction patterns of Zr$_{50}$Ti$_{50}$ cathodes compared to Ti and Zr powders; b) enlarged view showing the main peaks of the same spectra.

On the other hand, the XRD spectrum of Zr$_{50}$Ti$_{50}$ HUP cathodes denoted the presence of a new phase, whose peaks did not match neither with those belonging to Zr powders nor to those referring to Ti ones (Figure 7-43a-b). The attribution of these new peaks was not trivial: the best match among the database

spectra was with an HCP Ti/Zr mixed oxide, but some of the main peaks were still not ascribable to it.

References

[1] M. Audi and M. Pierini, "Surface structure and composition profile of sputter-ion pump cathode and anode," *J. Vac. Sci. Technol. A,* vol. 4, no. 3, pp. 303-305, 1986.

[2] A. Vesel, M. Mozetic, J. Kovac and A. Zalar, "AES investigation of anode deposits in magnetron-type sputter ion pump," *Applied Surface Science ,* vol. 246, pp. 126-131, 2005.

[3] A. Vesel, M. Mozetic, J. Kovac and A. Zalar, "XPS study of the deposited Ti layer in a magnetron-type sputter ion pump," *Applied Surface Science,* vol. 253, pp. 2941-2946, 2006.

[4] N. Yagi and S. Komiya, "In situ observation of a cathode surface contamination of a sputter ion pump by Auger electron spectroscopy," *J. Vac. Sci. Technol.,* vol. 18, no. 3, p. 1152, 1981.

[5] G. K. Wehner and D. J. Hajicek, "Cone formation on metal targets during sputtering," *J. Appl. Phys.,* vol. 42, no. 3, pp. 1145-1149, 1971.

[6] G. K. Wehner, «Whisker growth and cone formation on metal surfaces under ion bombardment,» *Appl. Phys. Lett.,* vol. 43, n. 4, pp. 366-367, 1983.

[7] G. K. Wehner, "Cone formation as a result of whisker growth on ion bombarded metal surfaces," *J. Vac. Sci. Technol. A,* vol. 3, no. 4, pp. 1821-1835, 1985.

[8] G. Carter, M. J. Nobes, G. W. Lewis, J. L. Whitton and G. Kiriakidis, "The effect of ion species on morphological structure development of ion bombarded (11 3 1) single crystal Cu," *Vacuum,* vol. 34, no. 1-2, pp. 167-173, 1984.

[9] M. Ohring, in *Materials Science of Thin Films*, Academic Press, 2002, pp. 164-166.

[10] R. L. Jepsen, "The physics of sputter-ion pumps," in *Proc. 4th Int. Vacuum Congr.*, London, 1968.

[11] I. Brodie, L. T. Lamont and R. L. Jepsen, "Production of high-energy neutral atoms by scattering of ions at solid surfaces and its relation to sputtering," *Phys. Rev. Lett.,* vol. 21, no. 17, pp. 1224-1226, 1968.

[12] J. A. Vaumoron and M. P. De Biasio, "Argon and rare gas instability with heavy metal cathode Penning Pumps," *Vacuum,* vol. 20, no. 3, pp. 109-111, 1970.

[13] N. Laegreid and G. K. Wehner, "Sputtering yields of metals for Ar+ and Ne+ ions with energies from 50 to 600 eV," *J. Appl. Phys.,* vol. 32, no. 3, pp. 365-369, 1961.

[14] N. Ashcroft and N. Mermin, Solid State Physics, Saunders College Publishing, 1976.

8. Conclusions

8.1. Final remarks

The series of FESEM/EDX and XRD analyses resumed in Chapter 7 was driven by the need to find any possible correlation between the crystal structure of each pair of cathodes, the surface modifications occurred during its use in IP-LAB and the sorption performances presented in Chapter 6.

The microscopic cones found on Ti cathodes, as already mentioned in Section 7.1.1, might be related to the outbreak of Ar instability, which is one of the main drawbacks of diode SIPs. Cones have been detected on several pairs of Ti-Ti cathodes always around the central erosion pit, where the most intense sputtering occurs. Implanted gas species are normally never found in this location due to the continuous erosion of the cathode surface; however, significant quantities of Ar have always been detected by EDX inside these cones. In some cases, Ne, N and C were also found and the tree-like structure of cones confirmed their progressive formation through the deposition of concentric layers of sputtered Ti, each one containing a different gas. In any case, the contribution of Ar to the growth of cones was always the largest.

Cones were observed also on the Ti cathode of the Cu-Ti bulk pair but not on the Cu one, confirming their presumed preferential growth on Ti. On the other hand, Zr-Zr cathodes also showed the presence of few, large, Ne and Ar-containing cones on their surface. Nevertheless, the Ar and Ne pumping speeds by Cu-Ti and Zr-Zr cathodes were perfectly in line with the linear dependence on the mean cathode atomic mass, as described in Section 6.4. Thus, the presence of cones does not seem to affect the saturation pumping speed of a cathode pair. On the contrary, it might perhaps influence their predisposition to instability; more

experiments specifically focused on this aspect should be possibly made in the future. Ar instability has already been documented for Cu-Ti flat cathodes below 10^{-4} Torr [1].

Cones were thus found on Ti-Ti cathodes but neither on Al nor on Cu ones. Their presence was attested on Zr cathodes but not on Nb ones, although they have almost the same atomic mass. Their chance to grow on a cathode during Ar sputtering seems thus to be independent on the atomic mass: more likely, it is influenced by the sputter yield of the cathode material. Ti and Zr, being both in the 4th group of the periodic table, are very similar from this point of view [2]. The difference with Nb and Ta, which belong to the 5th group, is rather small but perhaps sufficient to determine whether cones will grow or not.

When considering HUP cathodes, cones were found only on the ones made of pure Ti; the density of cones on their surface was indeed the highest ever observed. At the same time, Ar and Ne pumping speeds of these cathodes were the lowest among HUP materials and the lowest ever measured, even scarcer than Ti-Ti diode SIPs. Before the attainment of saturation, strong fluctuations were observed in the Ar sorption curves of Ti HUP (cf. Figure 6-12 and Figure 6-13); this seems to confirm the supposed role played by cones in the onset of instability.
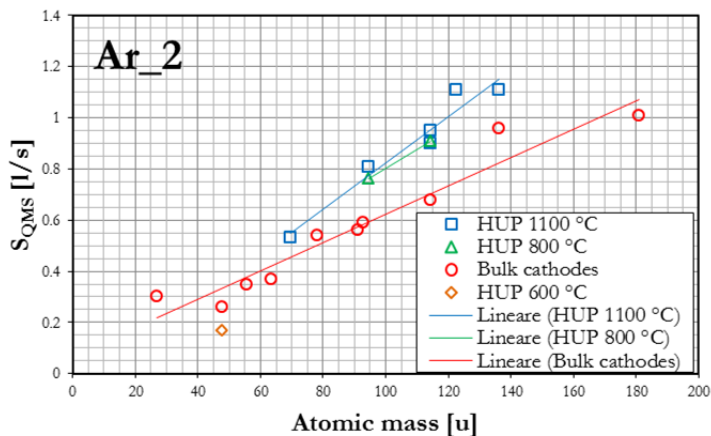
Figure 8-1 – Pumping speed after saturation S_{QMS} during tests Ar_2 of HUP and bulk cathodes as a function of the mean cathode atomic mass A. HUP cathodes are divided according to their annealing temperature.

165

On the other side, it is worth noting that cones did not affect all the other tested HUP materials, whose saturation pumping speeds were always higher than those of the corresponding bulk cathode plates (Figure 8-1). The formation of cones seems therefore to be a peculiarity of cathodes made of pure Ti (or, to a lesser extent, Zr): when Ti (or Zr) is mixed with another material—*e.g.*, $Zr_{50}Ti_{50}$, $Ta_{35}Ti_{65}$, $Ta_{50}Zr_{50}$—the growth of cones is somehow prevented, probably due to the combined sputtering of two metals with different atomic masses and sputter yields. In some cases, the remains of some eroded cones were perhaps observed also on these high-mass HUP cathodes; however, their correspondence to Ti cones should be still confirmed and, in any case, implanted gas species have never been detected inside these eroded structures.

Apart from cones, it has been significant to find out that HUP cathodes have Ne and Ar saturation pumping speeds higher than those of bulk cathodes with the same atomic mass, with the only exception of pure Ti HUP ones. As already mentioned, a possible reason for this might be that the beneficial effect given by the use of one Ta cathode in noble-diode SIPs is amplified if Ta and Ti are homogeneously mixed together. This applies also when coupling Ta and Zr. The pumping of CH_4 is dictated by completely different mechanisms; nevertheless, the example of $Ta_{35}Zr_{65}$ and $Ta_{50}Zr_{50}$ shows that a homogeneous dispersion of a low-performing material (in this case, Ta) does not affect at all the performance of the other component providing a high CH_4 pumping speed (*i.e.*, Zr).
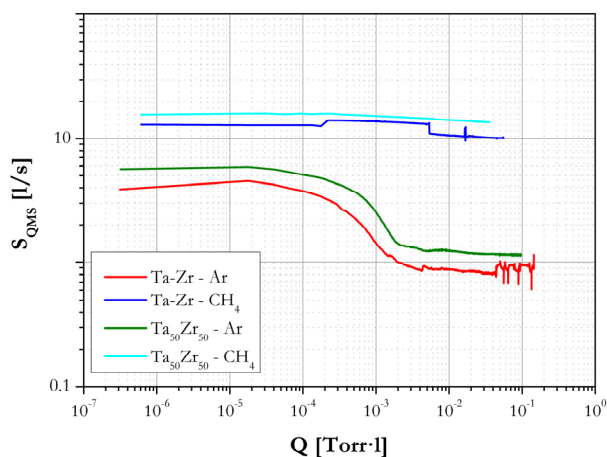

Figure 8-2 – Ar and CH₄ sorption curves of Ta-Zr cathodes and Ta₅₀Zr₅₀ ones.

Again, the possibility to mix two or more metals with different characteristics seems thus to be the key factor when high pumping performances should be ensured for several different gases. For instance, Ta increases Ar pumping speed and prevents the onset of Ar instability but, on the other side, it gives poor H_2 and CH_4 sorption rates. On the contrary, Zr is very good for these two latter gases but it has a lower Ar pumping speed, due to its atomic mass. A HUP cathode made of mixed Ta and Zr powders enhances the performances ensured for all these gases by the simple coupling of two separate Zr and Ta bulk cathode plates (Figure 8-2).
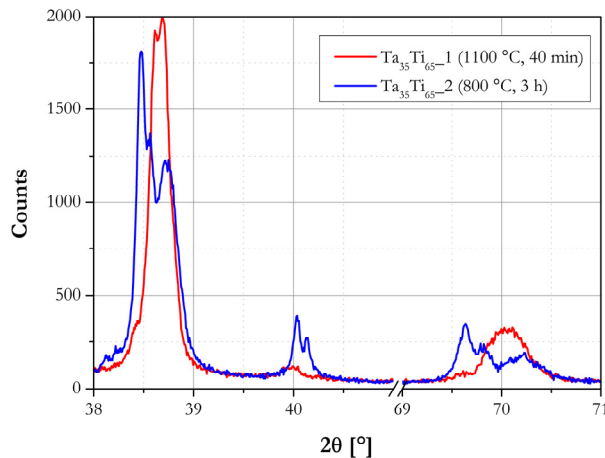
Figure 8-3 – Main peaks in the diffraction patterns of $Ta_{35}Ti_{65}\_1$ and $Ta_{35}Ti_{65}\_2$ HUP cathodes after their use in IP-LAB.

Other information can be obtained from the FESEM/EDX and XRD analyses of HUP cathodes. By backscattering imaging, extended parts of $Ta_{35}Ti_{65}\_1$ cathodes (annealed at 1100 °C for 40 min) appeared to be made of alternated lamellae with different concentration of Ti. These structures seem to be a peculiarity of these precise elemental composition and thermal treatment: to a much lesser extent, they have been detected also on $Ta_{50}Ti_{50}\_1$ and on $Ta_{50}Ti_{50}\_2$ cathodes (annealed at 1100 °C for 40 min and at 800 °C for 3 h, respectively). Lamellae were instead absent on $Ta_{35}Ti_{65}\_2$ (800 °C, 3 h) and on $Ta_{50}Ti_{50}\_3$ cathodes annealed at 1100 °C for 72 h. The diffraction patterns of $Ta_{35}Ti_{65}\_1$ and

167

$Ta_{35}Ti_{65}\_2$ differ in the shape of their main peaks (Figure 8-3); this might be somehow related to the morphological differences evidenced by FESEM/EDX imaging. In any case, the presence or not of these lamellar structures apparently did not affect the pumping performance of these cathode pairs with the same elemental composition.

		S_{QMS} [l/s]		
Cathodes	**Annealing**	**Ar_1**	**Ar_2**	**Ne_1**
$Ta_{35}Ti_{65}\_1$	1100 °C, 40 min	0.91	0.81	0.83
$Ta_{35}Ti_{65}\_2$	800 °C, 3 h	<u>0.54</u>	0.76	0.71
$Ta_{50}Ti_{50}\_1$	1100 °C, 40 min	0.91	0.90	0.78
$Ta_{50}Ti_{50}\_2$	800 °C, 3 h	<u>0.78</u>	0.91	0.73
$Ta_{50}Ti_{50}\_3$	1100 °C, 72 h	1.00	0.95	0.78

Table 8-1 – Saturation values of S_{QMS} during tests Ar_1, Ar_2 and Ne_1 at $P_m=5\cdot10^{-5}$ Torr with $Ta_{35}Ti_{65}$ and $Ta_{50}Ti_{50}$ HUP cathodes (the precision of pumping speed measurements is ±15% according to the ASTM F798-97 standard [3] but it might be even lower according to the laboratory experience).

In general, the XRD evidenced an increase of crystallinity for cathodes annealed at 1100 °C for 40 min with respect to those treated at 800 °C for 3 h. A 72 h long annealing at 1100 °C was of course even more effective in terms of crystallinity gain; FESEM/EDX imaging demonstrated a more uniform rearrangement of Ta and Ti, proven also by the absence of lamellae. It is difficult to ascertain whether this difference in crystallinity could impact on pumping speed or not. If Ar saturation pumping speeds of $Ta_{35}Ti_{65}$ and $Ta_{50}Ti_{50}$ cathodes are considered, the values obtained with those annealed at 800 °C were considerably lower during the first Ar_1 test; however, this discrepancy disappeared during the second Ar_2, at the end of the series of sorption tests (Table 8-1). Even if a performance gap was present at the beginning due to the lower annealing temperature, it tended therefore to vanish as sputtering on the cathodes by different gas species went on. A slight gap of the same kind was noticeable also during Ne tests. This trend might be further confirmed by Ti HUP cathodes annealed at 600 °C, whose performance was the worst for both Ar and Ne. On the other hand, when considering S and S_{QMS} during CH_4 pumping, the same Ti HUP cathodes were among the best and there was no clear distinction between TaTi cathodes annealed at high and lower temperature. This confirms the complexity of

the scenario and the need to carry on in parallel the optimisation of CH_4 and noble-gas pumping.

8.2. Current status and future prospects

This study has led to a deeper understanding of the dynamics on which the functioning of SIPs is based, focusing in particular on the memory effects given by their sorption mechanisms. Thanks to this, it has been possible to tune a standard experimental procedure that allows to obtain reliable and reproducible sorption curves for several gas species. Pumping speed measured after saturation, in particular, has been identified as a key factor for determining the performance of a SIP.

Starting from the experience gained with conventional diode and noble-diode SIPs, several innovative combinations of cathode materials (Al, Ti, Cu, Zr, Nb, Ta) have been investigated using this experimental sequence. In view of the combination of SIPs with NEG pumps, the focus has been on the sorption rates ensured by each pair of cathodes while pumping noble gases (primarily, Ar) and CH_4.

The first significant result of this experimental campaign has been that Ar (and Ne) pumping speed is linearly dependent on the atomic mass of the cathodes. Another major breakthrough has been represented by the introduction of cathodes made of a mixture of powders of two different elements, by means of the HUP sintering technique. The possibility to mix homogenously two elements (*e.g.*, TaZr or TaTi) instead of keeping them into separate cathode plates seems to affect positively the pumping of Ar and other heavy noble gases.

The series of sorption tests has been flanked by FESEM/EDX and XRD analyses of the cathodes, in order to highlight any possible correlation between their pumping performances and the structural and surface modifications occurred during the preparation of cathodes and their use in a SIP. Some interesting information has been collected about the formation of microscopic cones through sputtering and the choice of the most suitable annealing procedure. These two aspects might have a significant influence on the onset of Ar instability and on Ar pumping speed, respectively. However, the scenario is still incomplete and more data should be possibly collected in the future. For instance, it would be interesting

to verify also for heavier noble gases (Kr, Xe) the trend observed for Ar and Ne, whose pumping speeds grow linearly with the mean atomic mass of the cathodes.

In parallel, useful data have become available also about the sorption of CH_4. From this point of view, it is clear that the optimisations of Ar and CH_4 pumping cannot go hand in hand. Ta is for instance essential to improve Ar pumping but, at the same time, it is poorer than Ti and Zr in the sorption of CH_4. Nevertheless, the homogeneous dispersion of Ta powders typical of HUP cathodes seems to mitigate this weakness while promoting Ar pumping.

Having in mind this basic principle, more pairs of HUP cathodes ought to be tested in the future. Further binary combination of mixed elements should be studied and ternary mixtures as well as alloys might be taken into account too. A small atomic fraction of a third component with a high atomic mass could be for instance dispersed in the HUP matrix, in order to increase further the pumping of noble gases. Conversely, it could act also as a catalyst and foster the cracking of CH_4 molecules; in a SIP+NEG combination pump, the resulting H_2 would be effectively sorbed by the getter.

References

[1] J. A. Vaumoron and M. P. De Biasio, "Argon and rare gas instability with heavy metal cathode Penning Pumps," *Vacuum,* vol. 20, no. 3, pp. 109-111, 1970.

[2] N. Laegreid and G. K. Wehner, "Sputtering yields of metals for Ar+ and Ne+ ions with energies from 50 to 600 eV," *J. Appl. Phys.,* vol. 32, no. 3, pp. 365-369, 1961.

[3] ASTM, "F798-97: Standard practice for determining gettering rate, sorption capacity and gas content of nonevaporable getters in the molecular flow region," 2002.

Acknowledgements